MOLECULAR DYNAMICS SIMULATION OF A NANOSCALE DEVICE FOR FAST SEQUENCING OF DNA

By

Christina M. Payne

Dissertation

Submitted to the Faculty of the

Graduate School of Vanderbilt University

in partial fulfillment of the requirements

for the degree of

DOCTOR OF PHILOSOPHY

in

Chemical Engineering

December 2007

Nashville, Tennessee

Approved:

Peter T. Cummings

M. Douglas LeVan

G. Kane Jennings

Clare McCabe

Jens Meiler

To my mother, Janice, for her unconditional love and support

and

To my friends, for their endless encouragement

ACKNOWLEDGEMENTS

This work has been made possible through the financial support of the Department of Energy Computational Science Graduate Fellowship under grant number DE-FG02-97ER25308. I am extraordinarily grateful to have been a part of such an incredibly gifted and unique group of individuals comprising the CSGF fellows. Additional financial support for related research performed at Oak Ridge National Laboratory was provided by the National Institutes of Health under grant number 1R21HG003578-01.

I am grateful for all of the support and guidance I have received during my research from my advisor, Professor Peter T. Cummings. I would also like to thank the members of my Dissertation Committee for offering valuable insight and suggestions as well as Dr. Paul Crozier at Sandia National Laboratory for his exceptional mentorship and assistance.

I would like to thank Dr. James W. Lee of the Chemical Sciences Division of Oak Ridge National Laboratory for introducing the proposed nanoscale sequencing device and for helpful discussions. Dr. Lukas Vlcek is due special thanks for his help implementing electrode charge dynamics in LAMMPS.

Finally, I would like to thank my family and friends for their unconditional love and support in all my endeavors. Without them, I would not be the woman I am today.

TABLE OF CONTENTS

Page

LIST OF TABLES

LIST OF FIGURES

CHAPTER I

INTRODUCTION

Interest in technology capable of low-cost (less than $1000), high-throughput genome sequencing has risen significantly since the completion of the first sequencing effort in the Human Genome Project[1]. Such a technology could be a revolutionary tool in the advent of individualized medicine. In order for such a tool to be of use to a medical practitioner, however, sequencing of an individual's DNA would need to occur at speeds thousands times faster and at orders of magnitude lower cost than current available technology can offer.

A novel nanotechnology concept has been proposed to detect single molecules using a nanoelectrode-gated device, which, theoretically, has the capability of performing genome sequencing at a rate of 10^6 base pairs per second. Computational modeling of this nanoscale device has the potential to provide valuable insight into the behavior of the system for use in development of actual nanotechnology devices for application. In particular, molecular dynamics simulations that solve Newton's equations of motion to produce a trajectory for each atom can be useful in evaluating macroscopic properties such as velocity, diffusion coefficients, and molecular conformation[2]. These techniques eliminate the necessity of constructing multiple prototype devices to determine the ideal design characteristics.

The proposed nanotechnology concept hinges on the idea that each of the four nucleotides of which DNA is comprised (adenine, cytosine, guanine, and thymine) can be

uniquely identified by characteristic tunneling conductance properties (that is, current, I, versus applied voltage, V, curves)[3]. The device concept developed to take advantage of this property consists of two nanoelectrodes positioned anywhere from two to five nanometers apart on a nonconductive surface. This gap will serve as the detection gate through which tunneling conductance measurements will be made to identify the base pair directly between the nodes (see Figure 1).

There exists a multitude of possibilities for the design of this sequencing device concept. Structurally, the types of materials chosen for the surface and nodes are variable and could possibly influence molecular motion of the DNA strand. Additionally, the gap between the two nodes could be so large as to yield inaccurate tunneling conductance measurements or too small to allow unhindered passage of the DNA molecule. In the simulation of the sequencing device, properties such as the length of the DNA strand as well as the solvent in which it is contained may also be significant factors in the behavior of the conformational movement of the DNA.

A method for inducing and, consequently, controlling the translocation of the DNA strand through the gap in the nodes is also of significant interest. It has been experimentally shown that an electrical driving force in the range of 25-110 pN can pull a single-stranded DNA molecule through a 2 nm α-hemolysin nanopore[4]. The appropriate type of programmable applied electric field could plausibly allow for controlled motion at the desired velocity for sequencing the DNA strand. Another possible method for controlling the sequencing velocity is through the induction of Poiseuille flow in the solution, as in a nanofluidic device.

In addition to applied fields designed to direct horizontal motion of the DNA strand through the detection gates, a vertical field perpendicular to the applied field directing motion may be necessary. If the sequencing device were constructed of one surface, the DNA strand would need to be constrained to the surface in a particular position to prevent molecular drift and to aid in the positioning of the nucleotide between the nodes of the detection gate. Molecular drift could also be prevented by the use of two surface plates to contain the solution.

In short, there are many possibilities all within the realm of investigation through molecular dynamics simulations. This disseration will discuss the various simulations performed and the corresponding results in an attempt to satisfy my objectives for this project including (I) determining the magnitude of the controlling force necessary to produce the desired motion, (II) identifying the best possible method for controlling the transport and conformational motion of the DNA strand, and (III) evaluating the effects of the above mentioned design variables on the molecular conformation and transport properties of the translocating DNA introduced into the system.

I.1 Conceptual Device Design

The concept of polymer translocation through nanometer-sized pores is prevalent in biology. Many experimental and simulation studies have focused on a variety of polymers and nucleotides introduced into numerous pores and gaps of varying materials[4-13]. The range of complexity in previous studies related to the translocation of large biomolecules varies from simple electrophoretic mobility studies without the influence of nanopores[14] to full-scale experiments on translocation through nanopores with electrical

driving forces[4-9]. For the most part, the research relevant to the aims of this project has occurred within the past ten years, and only recently has research on similarly structured nanoscale systems become the focus of genomic sequencing efforts.

In conjunction with the experimental development of this project at Oak Ridge National Laboratories (ORNL), a basic device concept has been developed as shown in Figure 1. This conceptual device design is based on the precision electrolytic nanofabrication technique patented by Lee and Greenbaum at ORNL[15, 16] by which metallic atoms can be precisely deposited on the nonconductive and hydrophilic surface with an extremely small distance (1-10 nm) between the nanoelectrode tips. A pair of macroelectrodes will provide the electrophoretic field required to induce translocation of the DNA strand through the nanogap in the detection electrodes. The DNA sample molecules will be loaded into the device using micropipetting and/or microfluidic techniques.

The sequencing of the individual nucleotides as the DNA sample travels through the electrodes will be accomplished through the application of a tunneling electron beam across the metal electrodes. In theory, each of the four nucleotides has a unique corresponding conductance measurement. Measurement of this conductance will ultimately yield the sample sequence. In practice, this characteristic has yet to be proven either theoretically or in experiment. Additionally, theoretical studies of nucleotide conductance have been inconclusive. The most positive results indicating conductance sequencing techniques are a possibility have been published by Lagerqvist, et al.[17, 18]. They concluded through a combination of quantum-mechanical calculations of current and molecular dynamics simulations of DNA translocation that, in the absence of

structural fluctions, ions, and water, it is very likely DNA can be sequenced through a nanopore should dynamics be controllable. A second study of the feasibility of transversal DNA conductance measurement was reported by Zhang, et al.[19]. This study used first-principles calculation to determine transverse conductance across DNA fragments between gold nanoelectrodes. The conclusion presented here is that the conductance measurements of the four nucleotides differ only as a result of geometrical size (i.e. the space remaining between the sample and the electrodes). As this would be extraordinarily difficult to control in an on-the-fly sequencing device, they suggest this method of sequencing is not viable as a matter of convenience. The drawback to both of the theoretical studies of tunneling conductance measurements is their highly idealized simulation setups. Both examine DNA in the absence of realistic environments, such as the presence of solvent and counterions. Additionally, the first-principles study presented by Zhang does not represent the behavior of DNA at finite temperatures. Lacking a decisive conclusion on the feasibility of tunneling conductance sequencing techniques, we have continued the molecular dynamics study of transport behavior of such a device as presented here.

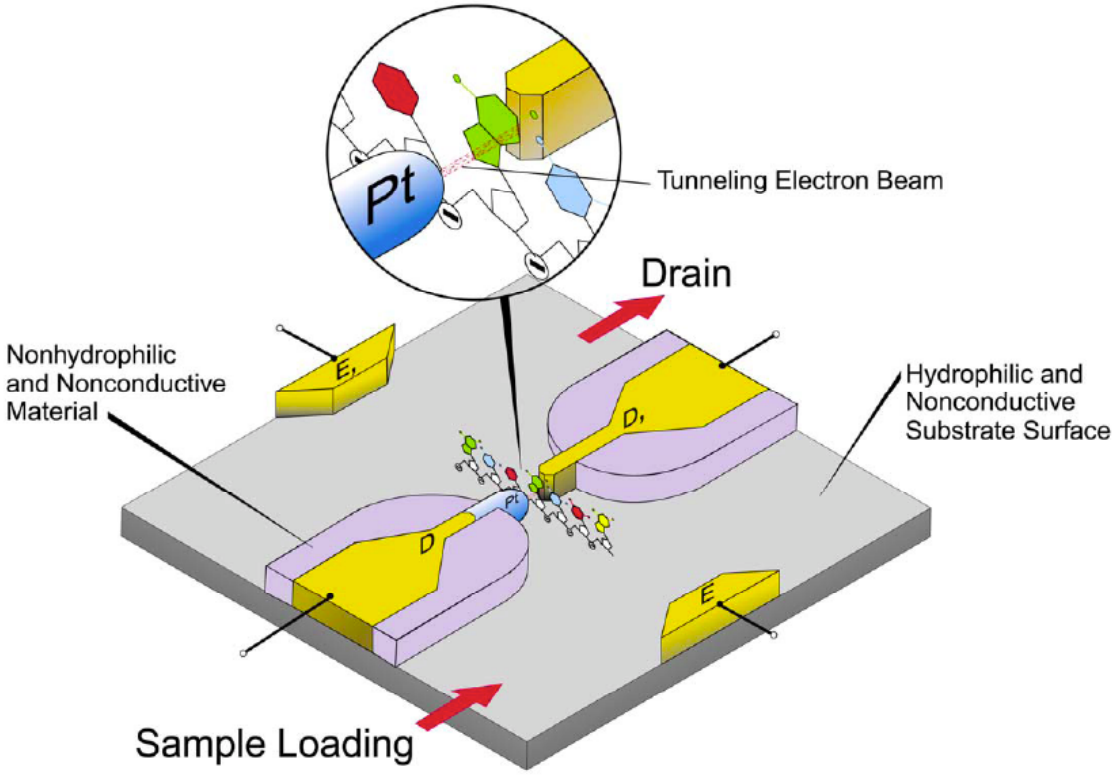

Figure 1: Nanoscale sequencing device concept developed by researchers at ORNL[20]

I.2 Design Variables

I.2.A Applied Electrical Fields

As mentioned before, there exist several variables in the conceptual design that may have significant effects on the functional operation of the nanoscale device. The variable at the forefront of this investigation is the use of an electrophoretic field to control translocation of the DNA strand. The importance of this applied electric field lies in the necessity of providing sufficient residence time between the nanogap and maintaining vertical stability of the molecule. Without an external driving force, the DNA strand likely will not move between the nanogap or maintain a velocity suitable for the purpose of base pair detection.

DNA is a negatively charged molecule having a charge of –1 per base pair. Positively charged counterions exist in solution around the DNA molecule to maintain a charge-neutral system and the proper conformation of the molecule. When an electric field is applied to the DNA in solution, the entire strand should move toward the anode while the counterions will move in the opposite direction. Many experimental studies have been performed using a voltage bias to induce movement of DNA in solution. In particular, Meller et al.[4] used an electrophoretic driving force to force single-stranded DNA through a 2 nm diameter α-hemolysin nanopore.

Controlling the transduction of the DNA strand may not be as simple as the application of a uniform electrical field, however. The required detection period may necessitate the use of an electrophoretic pulse as shown in Figure 2. While this is an experimentally feasible solution to the problem of controlling motion, implementation of

a pulsing field in a molecular dynamics simulation presents a problem due to the timescale relation to reality. Experimental pulsing of a field includes a ramp-up period of approximately 10 ns and, likewise, a ramp-down period of 10 ns in addition to the pulse period. Thus, modeling a realistic electrical pulse would require simulation times of at least 20 ns. These timescales are not completely unattainable; however, the computational cost of such simulations strongly suggests studying a uniform electric field initially. Investigation of the electrical driving force is primarily for determining an appropriate magnitude.

In the experimental design, there is also a need for a perpendicular holding field to properly align the DNA strand between the detection electrodes and retain it on the surface of the sample plate. The negatively charged phosphate groups along the backbone of the DNA will serve to align the DNA strand with the application of a perpendicular field as seen in the inset of Figure 1. An additional applied field across the detection nodes is necessary to perform the tunneling conductance measurements by which nucleotide sequence will be determined.

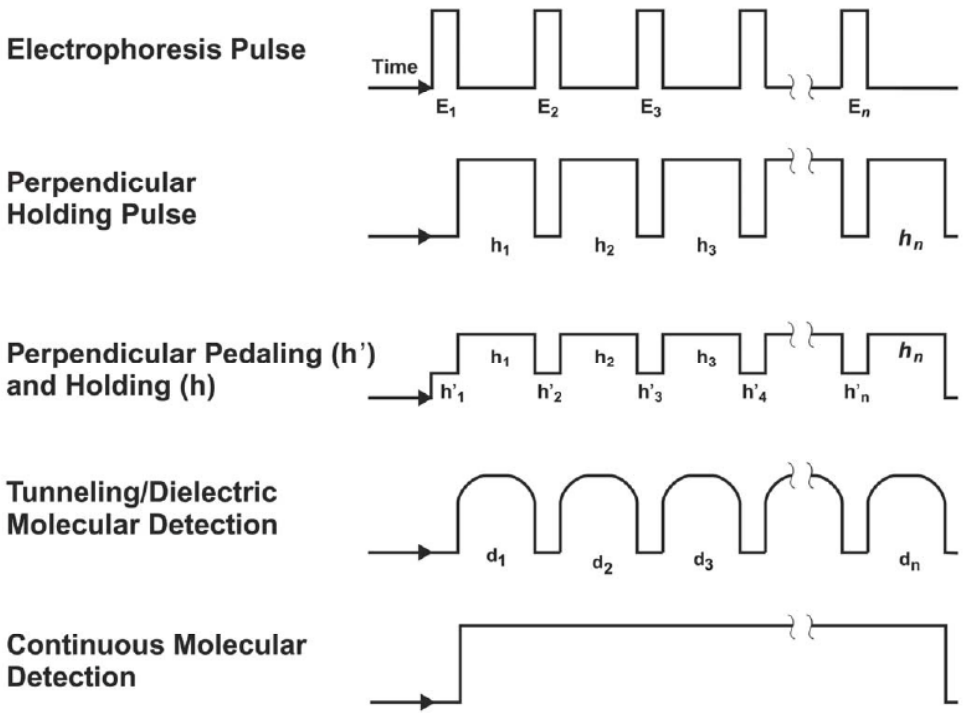

Figure 2: Proposed synchronization and coordination of applied electric fields

I.2.B Materials of Construction

The material chosen for the prototype design of the nanoscale-sequencing device has been determined to suit both experimental and simulation needs. The surface of the sample plates must be constructed out of a nonconductive and hydrophilic material. The sample plates must be nonconductive as to not interfere with the tunneling conductance measurements and hydrophilic so that the solvent will wet the surface and not create any adverse interactions that may affect the movement of the DNA strand. The device must also be designed to minimize leakage current to potentially improve the detection sensitivity. Initially, the surface material of interest was silicon dioxide; however, this material proved to be too rough at 1 nm, approximately the size of the molecules of interest in simulations. A paper by Leng and Cummings[21] presents results of the molecular dynamics simulations of water confined between two mica surfaces indicating that water confined between mica surfaces of the separation distance needed for the nanoscale device (~ 3 nm) does not exhibit abnormal fluidic behavior. Thus, mica surfaces have been used in simulations.

The electrodes must be conductive to achieve the intended purpose as tunneling current detection nodes. The electrolytic nanofabrication technique mentioned previously has been developed to precisely fabricate (approximately 100 atoms per step) a gap as narrow as 1 to 10 nm by deposition or depletion of metal. Consequently, metal nodes are ideal for the purpose of molecular detection nodes in the proposed sequencing device. Currently, the experimental plans call for platinum and/or gold nodes though, as will be shown, we have also made use of copper electrodes in many of our simulations. Again, the issue of current leakage is a factor in the sensitivity of the nanoelectrode-gated

detection system. It is only possible to use charge transport through the molecule as a means of detection when the leakage current is less than the tunneling current. This can be controlled by the addition of insulating shields around the sides of the detection electrodes, which should be constructed of a hydrophilic, nonconductive substrate such as silicon nitride (SiN). This is not reflected directly in simulations, however, because of the discrepancy in scale.

A final element in construction of the sequencing device is the choice of solvent in which the DNA sample is contained. The device has been developed under the assumption that the solvent will be water. For now, the simulations are being carried out in an aqueous environment, but it may be necessary to incorporate a more viscous solvent to achieve the desired control over the motion of the DNA sample.

I.2.C Electrode Gap Width

Experimentally, the gap distance between the electrodes can be fabricated as small as 1 nm creating a natural lower bound to the gap distance. Additionally, the electrodes must be within a few nanometers to observe a large tunneling current for detection purposes, resulting in an upper bound. The diameter of the DNA helix, 2 nm[22], gives a good estimate as to the actual value to choose.

While some stretching of bonds during translocation is acceptable, significant denaturation of the strand may adversely affect the detection process, so the gap must not be so small as to prevent reasonable conformational motion. In the paper by Heng, el. al.[5], the electrophoretically-driven DNA strand forced through a 1.2 nm pore in a Si_3N_4 membrane exhibited rupture of hydrogen bonds connecting three terminal base pairs.

However, the experimental studies performed by Meller, et al.[4] utilized a 2 nm diameter α-hemolysin pore in effectively allowing passage of a single-stranded DNA sample with clear evidence of elongation but no bond breakage.

Furthermore, large gap distances allow for folding of the sample as it passes through the detection gate. Studies by Storm, et al.[7] indicate that a pore diameter of 10 nm allows for the passage of DNA in a folded conformation. For proper nucleotide detection, the DNA must pass through the gap a single base pair at a time. Thus, the gap must be much smaller than 10 nm, most likely, closer to the lower distance constraint.

I.2.D Sample Length and Sequence

In 2001, Meller, et al.[4] performed experiments in which single-stranded DNA polymers were driven through a single α-hemolysin pore (2 nm in diameter and 5.2 nm depth) by an applied electrical field with the purpose of measuring current blockage across the length of the pore as the DNA strand is in residence as well as time distribution as it is related to length of the strand. Using the current blockade measurement to estimate residence time, and thus velocity, the authors conclude that strands longer than the length of the pore travel at a constant velocity while the velocity of shorter strands increases with decreasing length.

Storm, et al.[7] experimentally investigated the relationship of translocation time and length of double-stranded DNA electrophoretically driven through a 10 nm diameter silicon oxide pore of approximately 20 nm in depth. They observed a power-law scaling of translocation time with length. Though this likely will not hold true for smaller diameter pores, these studies indicate the importance of sample length with regard to pore

length. The majority of the simulations presented here use a single-stranded DNA sample of 16 nucleotides, which is approximately 5.5 nm in length. We also present a sample length simulation study in which the largest sample molecule is 48 nucleotides long. We are limited in sample length by simulation device design. The length of the pore, or gate, of the current design in this dissertation is approximately 2 nm. Hence, in our cased, the DNA length is longer than the pore length. On the basis of the Meller, et al.[4] experiment, we should expect to see constant translocation speed through the "pore" created by the nanoelectrodes.

I.3 Molecular Dynamics Simulation

In this work, the simulations being performed are known as classical molecular dynamics simulations. This method of simulation determines atomic trajectory by using an integrator, such as the Verlet Integrator[23], to solve Newton's second law of motion,

$$m_i \frac{d^2\mathbf{r}_i}{dt^2} = \mathbf{f}_i \tag{1}$$

for every atom in the system where m_i is the mass of atom i, $\mathbf{r}_i$ is the atom's position vector, t is time, and $\mathbf{f}_i$ is the force acting upon the atom as given below.

$$\mathbf{f}_i = -\nabla_{\mathbf{r}_i} U \tag{2}$$

In Equation (2), the potential energy or force field, denoted by U, is a description of how the atoms interact with surrounding atoms, and force, $\mathbf{f}_i$, is obtained from the gradient of the potential energy with respect to the position of atom i, $\mathbf{r}_i$. This intermolecular potential function is of great significance is determining the accuracy of the simulation being performed as will be illustrated by the results presented with in this dissertation.

Other technical issues associated with simulation methodology are discussed in the computational methods section of each chapter.

CHAPTER II

PRELIMINARY SIMULATIONS

II.1 System Setup of Nanoscale Device for Simulation

Using the device concept developed for experimental studies, a simulation prototype was developed. Figure 3 illustrates the actual device as used in the initial simulations. The initial device under examination consisted of two mica plates separated by approximately 3 nm. Each plate measured 20.7 nm x 14.4 nm. The detection nodes were constructed of a single gold node and a single platinum node each measuring 2 nm x 5 nm x 3 nm and separated by a 2.87 nm gap (as measured from center-to-center of the outermost atoms, shown in Figure 4). The DNA strand consisted of a single-strand of 16 base pairs, eight consecutive cytosines followed by eight consecutive thymines, which was solvated in water of 1 g/cc density. The ssDNA strand is surrounded by 15 sodium ions to make the total system charge neutral. The first residue of the ssDNA was placed approximately 1 nm from the entrance to the nanogate. The entrance of the nanogate is defined as the center of the external metal atoms closest to the ssDNA. The total dimension of the simulation box was 20.7 nm x 14.4 nm x 5 nm.

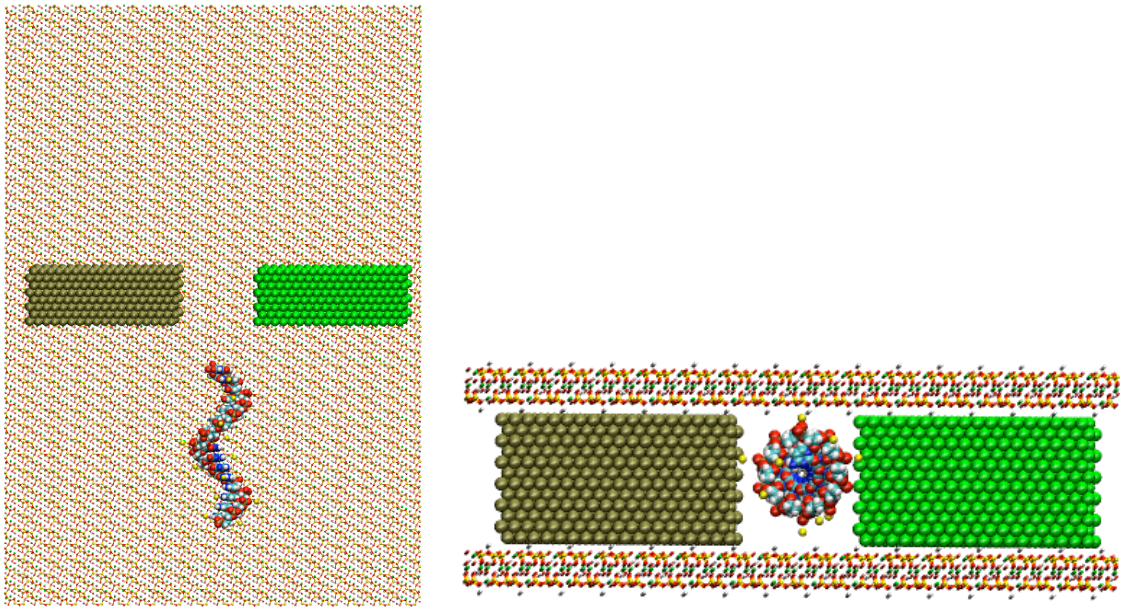

Figure 3: A top view shown without the upper mica plate for clarity and side view of the sequencing device initially examined using molecular dynamics. Platinum is shown in tan, and gold is shown in green.

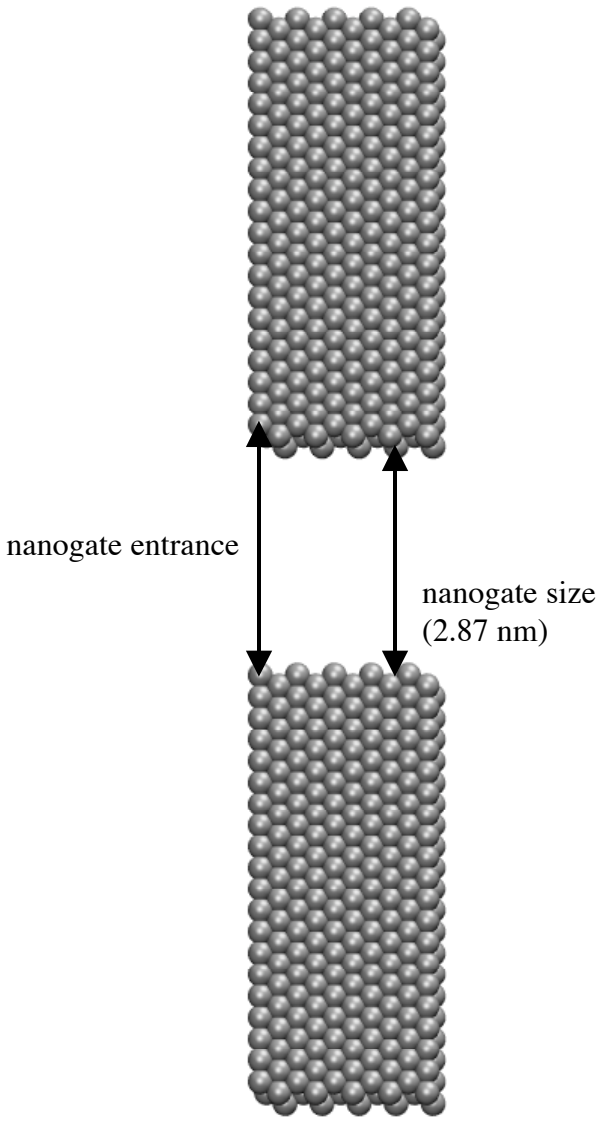

Figure 4: Representation of the definitions of “nanogate entrance” and “nanogate size”

II.2 Computational Methods

The software package known as LAMMPS (Large-scale Atomic/Molecular Massively Parallel Simulator) was used to carry out the molecular dynamics simulations in this proposal[24, 25]. The interaction potentials varied based on the atom type. The DNA molecules were described using the CHARMM27 all-hydrogen potential[26, 27] which means that all hydrogens are explicitly taken into account as opposed to united atom models which do not have explicit hydrogens (e.g., CH_3 groups represented as a single interaction sphere). In the CHARMM27 potential, bond stretching interactions are described a harmonic potential. Angle bending is represented by a harmonic potential on the angle, and dihedral angles are represented with a cosine series. Improper torsions are occasionally enforced with a harmonic term. Non-bonded atoms are described with a 12-6 Lennard-Jones plus Coulombic interaction

$$U_{ij}(r) = \frac{q_i q_j}{r} + 4\varepsilon_{ij}\left[\left(\frac{\sigma_{ij}}{r}\right)^{12} - \left(\frac{\sigma_{ij}}{r}\right)^{6}\right] \tag{3}$$

where U_{ij} is the non-bonded potential energy, r is the distance of separation, q is point charge, ε is an energy parameter, and σ is a distance parameter. The sodium ions were represented by a potential developed by Beglov and Roux[28]. The water was described by the rigid water model known as TIP3P[29] that describes the oxygen by a Lennard-Jones site and the hydrogens as bare charge sites. This particular water model is somewhat crude compared to newer models; however, because the CHARMM27 potential was parameterized to be used with the TIP3P potential, and a detailed description of the solvent in these simulations is unnecessary, the computationally efficient TIP3P model was chosen to represent water. TIP3P has three rigid interaction sites described by

Lennard-Jones and Coulombic terms. The mica surface potential was represented by the CLAYFF force field which was developed for hydrated crystalline compounds and their interfaces with fluid phases[30] which reduces to a Lennard-Jones term plus Coulombic interaction with the mica surfaces being held fixed as we have in all our simulations. Lastly, the force field temporarily being used to describe the platinum and gold electrodes is called UFF (Universal force field)[31]. The use of the UFF potential for metals is expected to be somewhat inaccurate since it does not take into account the response of valence electrons in the metal to the motion of charges in solution (commonly referred to as image charges when the metal surface is infinitely large and molecularly smooth). Thus, the search for a more realistic force field to model metal-charge interactions was necessary as will be discussed in the preliminary results. When two species described by different potentials interact, the interaction is typically estimated by a Lennard-Jones potential with parameters determined by using the Lorentz-Berthelot mixing rules shown in Equation (4) to combine individual parameters.

$$\sigma_{ij} = \frac{1}{2}\left(\sigma_i + \sigma_j\right)$$
$$\varepsilon_{ij} = \sqrt{\varepsilon_i \varepsilon_j} \tag{4}$$

Long-range Coulombic interactions were computed using a particle-particle particle-mesh (PPPM) solver[32].

The simulations were setup to have periodic boundary conditions in the x and y direction with motion in the z direction limited by the presence of the mica sheets. The z direction was modeled by a slab geometry, which inserts empty volume between the mica sheets and removes the dipole inter-slab interactions to effectively "turn off" slab-slab interactions. These boundary conditions allow the DNA strand to continue movement

across boundaries in the x and y direction and reduces computational expenditure, since the 3-D slab geometry technique is less computationally demanding than using a 2-D Ewald method[33].

All simulations were equilibrated for 1 ns using the NVT ensemble at 300 K with a Nosé-Hoover thermostat[34-36]. The hydrogen bonds being simulated were constrained through the use of the SHAKE algorithm. Because we are not interested in the dynamical behavior of the mica sheets or the electrodes, these atoms were excluded from the integration performed using the Velocity Verlet algorithm. This left the total mobile atoms in the simulations at 80,448 from a total of 134,208 atoms. The initial equilibration timestep was 0.0005 fs to allow for the extremely non-ideal atomic positions to relax to more energetically favorable positions. The remainder of the integration was carried out with a 2 fs timestep.

After the 1 ns equilibration, the simulations were restarted with the addition of an applied uniform external electrical field of varying magnitude. This was originally not part of the functionality of LAMMPS, so we developed a modular addition to the original code that implements an additional force to chosen atoms based on the equation below.

$$\mathbf{F} = q\mathbf{E} \tag{5}$$

This addition has been included in the latest version of the LAMMPS software package. The simulations run with the addition of an external field were run under the exact same conditions as the equilibration simulation for 1 ns.

Upon applying the electric field to the system, this force became the primary contribution to DNA drift dynamics. Diffusion and conformational dynamics contributed

little to the forward motion of the molecules due to the magnitudes of the applied fields except for the case of very weak applied fields.

II.3 Results and Discussion of Initial Simulations

The first in a series of simulations designed to develop a relationship between the velocity of the DNA sample and the applied field magnitude was the simulation of an applied field of magnitude –0.05 V/Å in the x direction. This magnitude is considerably larger than the experimentally suggested magnitude of –0.01 to –0.02 V/Å. The purpose behind simulating an applied field much larger than necessary was to insure that motion was indeed induced as well as to provide insight into the range of velocities produced over varying magnitudes. Snapshots of the simulation results shown below in Figure 5 illustrate the progression of the DNA strand as it translocates though the electrodes, continues past the boundary plane, and then reappears within the simulation box. Sample simulation movies are available for viewing at http://flory.vuse.vanderbilt.edu:16080/~christy. The sodium counterions travel in the opposite direction of the DNA as a result of their charge and disperse throughout the simulation box. The mica plates have not been visualized for clarity.

Using the center of mass of the DNA sample as a position reference, the velocity was determined by taking the difference of the current position from the original position and plotting it versus time. Figure 6 is a plot of the displacement from the original center of mass vs. time for the –0.05 V/Å simulation. As illustrated by the difference in slope before the molecule reaches the nanogate (<100 ps) and after (>100 ps), the velocity of the molecule seems to be dependent on the positioning with respect to the nanogate. The

molecule appears to be traveling at a velocity of approximately 200 Å/ns before it reaches the nanogate and increases velocity in the vicinity of the nanogate to 415 Å/ns. These values are substantial departures from the desired value of 1 to 2 Å/ ns to μs. As expected, there is little motion in y and z-directions of the simulation because the field was applied in x-direction.

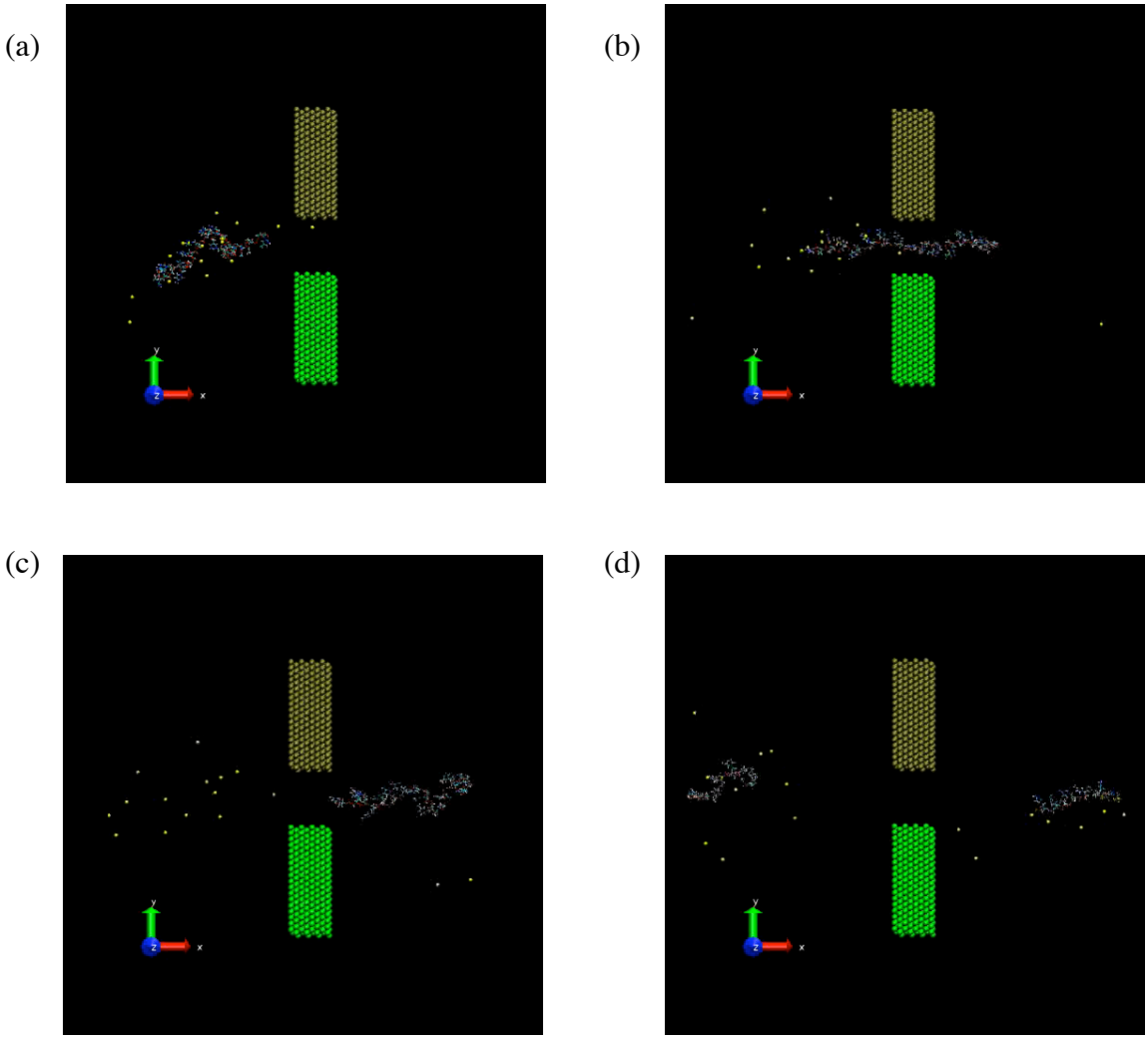

Figure 5: Snapshots of the –0.05 V/Å applied field simulation of ssDNA (C_8T_8) in water at (a) 0 ps, (b) 150 ps, (c) 275ps, and (d) 500 ps

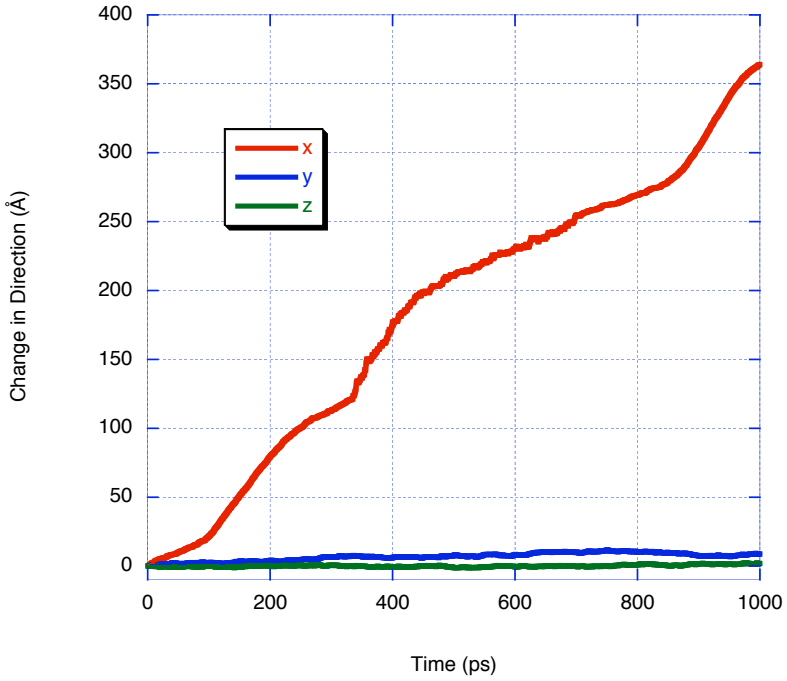

Figure 6: Change in direction vs. time based on the center of mass with an applied electrical field of –0.05 V/Å.

As a result of obtaining such remarkable velocity with the –0.05 V/Å applied field, the next simulation in this series implemented a field of less than half that magnitude at –0.02 V/Å. As expected, the lower magnitude electrical driving force resulted in slower translocation of the DNA sample. The sample translocated through the electrodes a single time in the case of the –0.02 V/Å field. Again, as illustrated in Figure 7, the velocity observed as calculated through the displacement from the original center of mass position has two distinct regimes, bulk velocity and approaching translocation. The bulk velocity appears to be around 50 Å/ns while the velocity increases to near 220 Å/ns as the DNA strand approaches and passes through the nanogate. Movement in the y and z-directions is negligible in comparison to x-directional velocity. Like the resulting velocity from the applied field of –0.05 V/Å, the induced velocity from the –0.02 V/Å field is much larger than desired.

Continuing the series of simulations attempting to evaluate the relationship of applied field magnitude to induce velocity, we simulated the application of a –0.01 V/Å magnitude field. The DNA sample did not completely translocate through the electrodes during the 1 ns production run. Figure 8 shows that, despite the fact that complete translocation did not occur, there remains a definite distinction between the velocity of the sample in the bulk water and when the sample is near the nanogate. In this case, the velocity of the sample in the bulk is approximately 24 Å/ns; whereas, the velocity of the sample nearing and entering the nanogate appears to be 61 Å/ns.

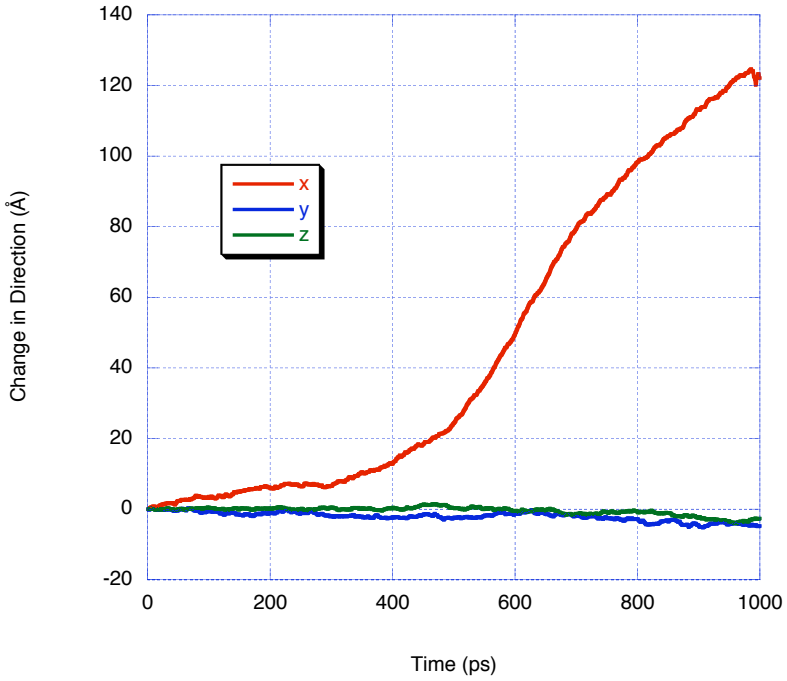

Figure 7: Change in direction vs. time based on the center of mass with an applied electrical field of –0.02 V/Å

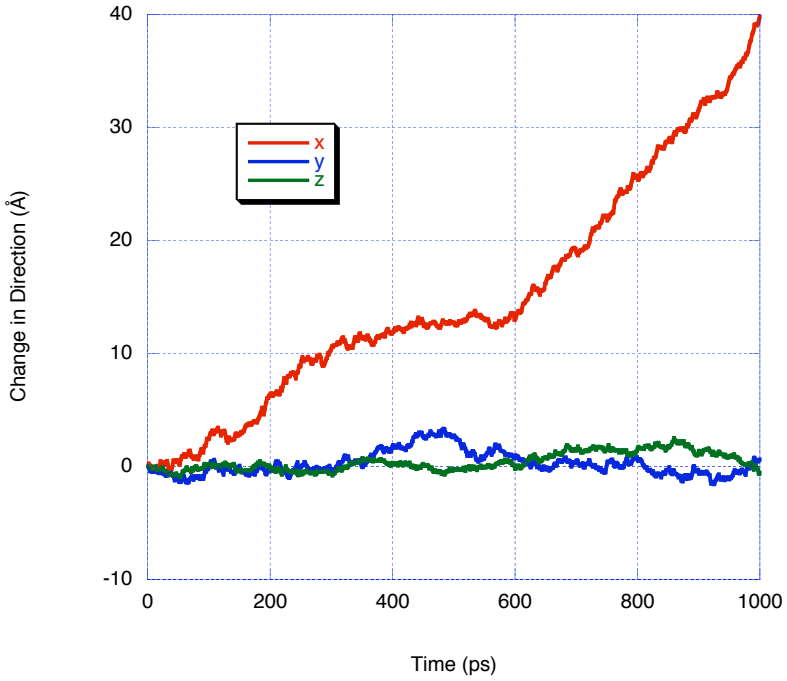

Figure 8: Change in direction vs. time based on the center of mass with an applied electrical field of –0.01 V/Å

The next simulation in this series was that of an applied field of –0.0075 V/Å. The –0.0075 V/Å magnitude applied field resulted in less definitive bulk motion in comparison to previous simulations. As shown in Figure 9, the DNA seems to exhibit somewhat oscillatory velocity at 4 Å/ns in the x-direction as the strand creeps toward the nanogate over a period of 800 ps. When the sample reaches a point near the nanogate, the velocity increases to approximately 65 Å/ns. This is roughly the same velocity in the vicinity of the electrodes as the resulting velocity of a –0.01 V/Å applied field. Under this lower magnitude applied field, the motion in the y and z-directions becomes more noticeable; however, the application of an external field in the x-direction will override motion in the y-direction. The z-direction is fixed due to the presence of the mica surfaces above and below the sample solution.

Following the –0.0075 V/Å simulation with a –0.005 V/Å simulation, we are presented with seemingly contradictory results. In Figure 10, one can see that the oscillatory behavior at approximately 5 Å/ns reappears under the low magnitude applied field; however, this behavior is only exhibited over 200 ps before the DNA reaches the pull of the nanogate and increases in velocity to 19 Å/ns.

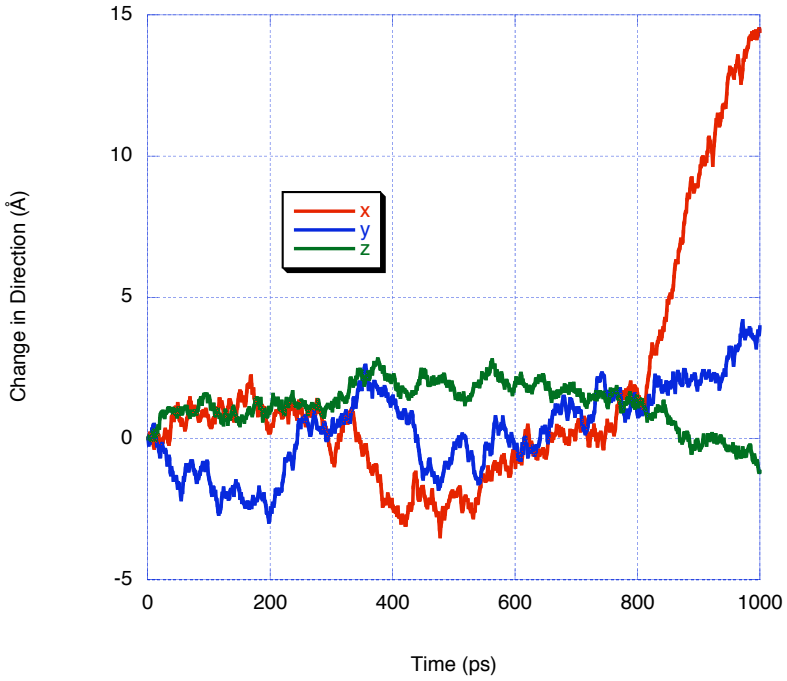

Figure 9: Change in direction vs. time based on the center of mass with an applied electrical field of –0.0075 V/Å

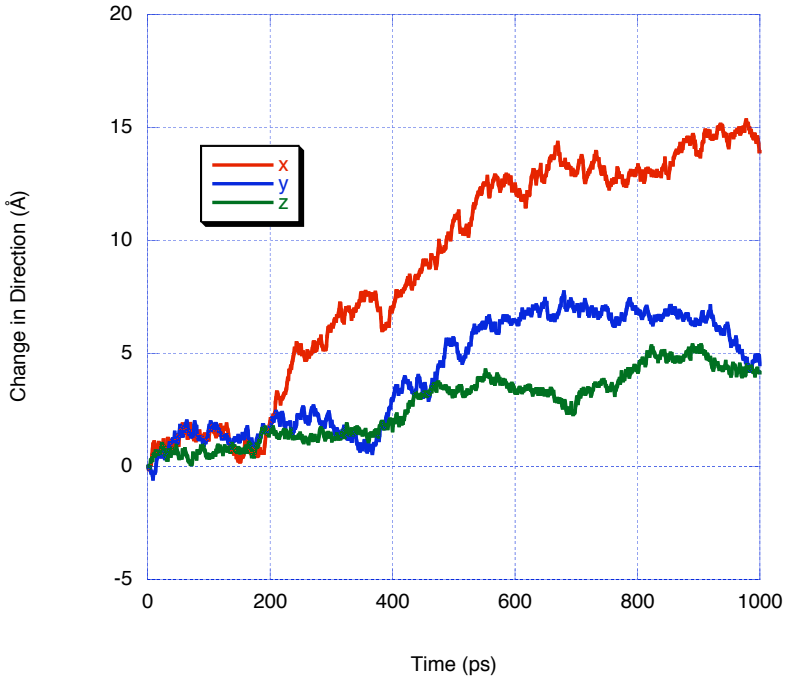

Figure 10: Change in direction vs. time based on the center of mass with an applied electrical field of –0.005 V/Å

Continuing to lower the magnitude of the applied field to –0.002 V/Å results in entirely oscillatory motion of nearly the same velocity in all directions resulting in no appreciable net motion as seen in Figure 11. This and the behavior of the –0.0075 V/Å and –0.005 V/Å simulation leads to the conjecture that an apparent energy barrier to motion exists which must be overcome before the molecule begins its approach to the nanogate. It is my opinion that should the simulation of the –0.002 V/Å applied field be continued beyond the 1 ns production run, the DNA molecule would eventually begin progressing toward the electrodes as the molecule did previously under larger magnitude fields.

Examining the relationship of the magnitude of the electric field with respect to the apparent velocity of the center of mass of the molecule requires examining both the bulk velocity and the velocity in proximity of the nanogate. As previously shown, these two situations within the simulation result in drastically different behaviors. Figure 12 is a compilation of the velocities resulting from the above-mentioned simulations.

Position relative to the nanogate was delineated by the marked acceleration of the molecule. The ssDNA molecules appeared to accelerate when the first base pair was within 0.5 nm of the entrance to the gap. All molecules, with the exception of the smallest magnitude applied electric field (-0.02 V/Å), entered the device gap to some degree during the course of our simulations. This acceleration may be an artifact of the force fields used for the DNA-electrode and water-electrode interactions[37]. According to the results, the bulk velocity relationship to the electric field magnitude appeared to be nearly linear, given the rough approximation of velocity, when the field strength was

stronger than –0.01 V/Å which was in agreement with previous similar simulations[14]; however, under smaller magnitude fields, the motion fell into somewhat oscillatory behavior, perhaps as a result of the short length of the simulation and possible energetic barriers to translocation. The relationship of the velocity near the nanogate to the field magnitude appeared to be nonlinear given the set of velocities available. One could compare this to what is known for non-biological polymers translocating through nanopores, for which a consensus on the expected behavior of polymers translocating through nanopores has not been reached at this time. Over small ranges of applied fields, the drift velocity of polymers varied linearly with potentials[38]; however, over wider ranges, the relationship appeared to be more quadratic in form[4]. This could be attributed to the large number of variables involved in determining this relationship such as the pore material/polymer interactions, length of the polymer affecting velocity, and energetic barriers to translocation in general. Despite my conjectures, definitive relationships cannot be determined from this limited set of data.

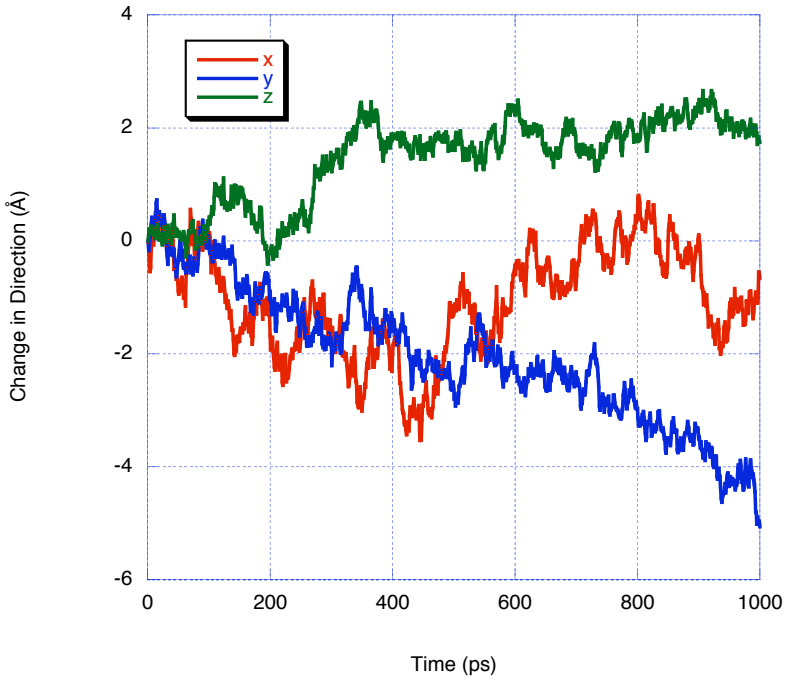

Figure 11: Change in direction vs. time based on the center of mass with an applied electrical field of –0.002 V/Å

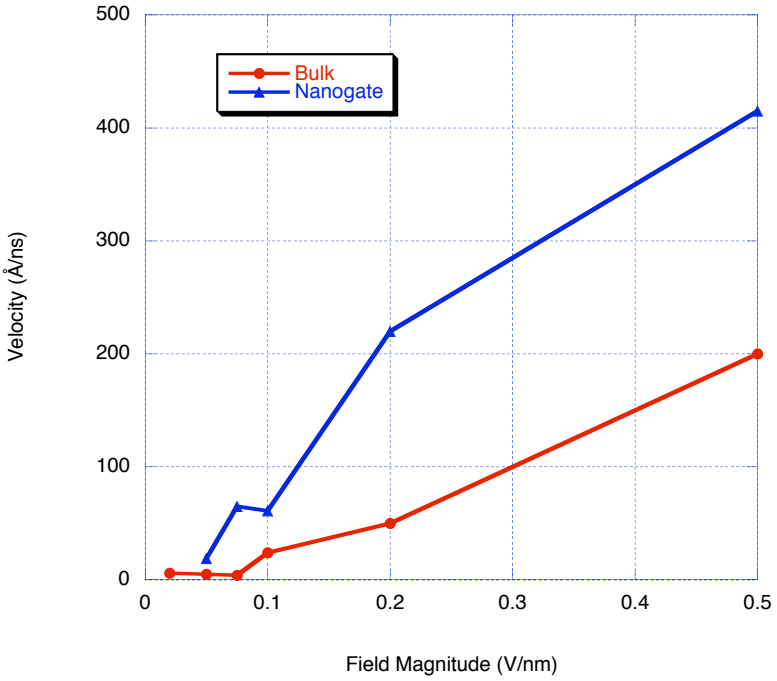

Figure 12: Relationship of velocity to applied field magnitude. Also, the difference between bulk and nanogate velocity increases with applied field. Note that both bulk and nanogate velocities exhibit the same overall trend with increasing field.

A comparison of the observed bulk velocities in the previously discussed simulations to the capillary electrophoresis mobility study performed by Stellwagen and Stellwagen[39] reveals order of magnitude consistency in velocity measurements. The experiments made use of a technique known as capillary zone electrophoresis, which is the electrophoretic technique that most closely approximates the bulk behavior of the simulated nanoscale device. In this experimental study, single and double strand DNA 20 base pair oligomers in a buffer of 40mM Tris-Cl, 0.1 mM EDTA at 7.6 pH were electrophoresed through a capillary coated with polyacrylamide 38.8 cm long and 100μm in diameter at 200 V/cm (2×10^{-6} V/Å). Stellwagen noted that free solution mobility of DNA increases with increasing molecular weight up to a plateau that occurs around 170 base pairs. A relationship between sequence and mobility was also observed in this experiment; however, for the purpose of assessing consistency between simulation and experiment, all sequence mobilities observed in this experiment were in the range of 2.894×10^{-4} and 2.944×10^{-4} $cm^2V^{-1}s^{-1}$. With an electrophoretic field of 200 V/cm, these mobilities correspond to velocities in the range of 0.00578 to 0.00588 Å/ns. The electrophoretic field, at 0.000002 V/Å, is much smaller than the smallest applied field, 0.002 V/Å, in simulations described above. Figure 13 is an illustration of the predicted velocities based on an assumed linear relationship to electric field magnitude compared to observed bulk simulation velocities. Given the slight differences in the experimental and simulated environment, the velocities observed in simulation are consistent with the extrapolated velocities based on experimental data.

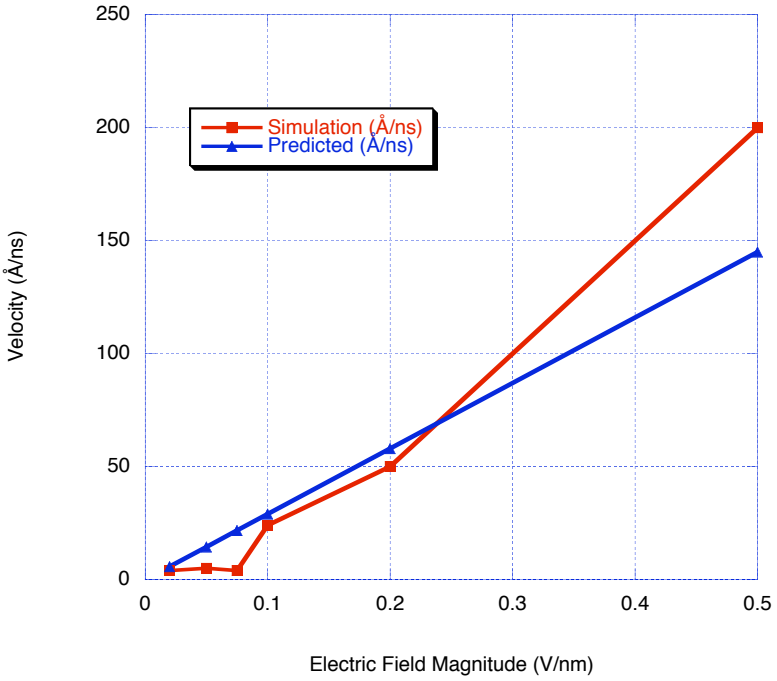

Figure 13: Relationship of velocity to applied field magnitude in bulk solution compared to velocities predicted based on electrophoretic experiments

An additional behavior of note observed in each simulation as the DNA sample passes through the nanogate is molecular elongation. This is somewhat expected due to the size of the nanogap at 2.87 nm. Furthermore, this may be a root cause of the increase in velocity as the DNA translocates due to the repulsion forces created to achieve the energetically favorable relaxed conformation after translocation. Elongation was quantitatively observed by tabulating the end-to-end distance of the molecule as a function of time as shown in Figure 14. In the event that the DNA sample enters the gap between the electrodes, the end-to-end distance increases by almost 30 Å as the DNA passes through the nanogate which is roughly 55% of the initial length. While the helix geometry does not maintain rigidity, the molecular structure does not appear to stretch beyond reasonable expectations. In the simulation of the –0.05 V/Å magnitude applied field, this elongation pattern is observed twice as the molecule reentered the simulation boundary and translocated a second time.

Additional analysis of factors such as the radius of gyration and the root mean square distribution have thus far yielded no additional insights about the nature of motion of the DNA sample.

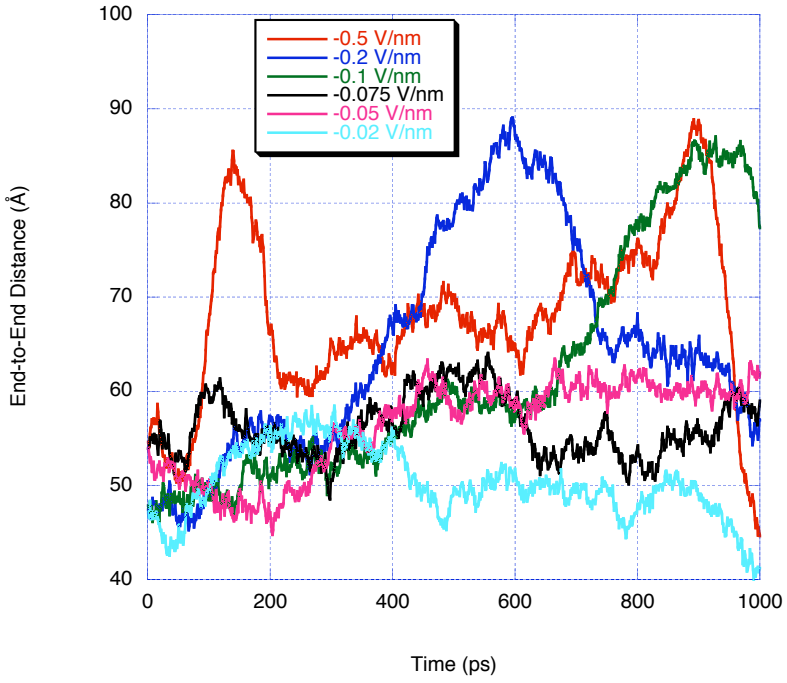

Figure 14: End-to-end distance vs. time of DNA under an applied electrical field

II.4 Interaction Potential for Metals and Non-metals

A significant fault of the preliminary simulations is the lack of an adequate interaction potential for describing the behavior of non-metal atoms interacting with metal atoms. A visualization of the equilibrated system in which the water molecules are shown, Figure 15, exemplifies the inadequate description. One can see how the metallic surface appears hydrophobic and the water molecules form lower density pockets around the surface of the metal.

One of the most important tasks to be accomplished within this project is to properly implement a new potential into LAMMPS to account for the metal/non-metal interactions. The current behavior of the water at the electrode surface may possibly be interfering with the forward motion of the DNA molecule. Additionally, the repulsion from the electrodes is not limited in its effects to water and may explain the reluctance of the DNA strand to translocate under lower magnitude electric field application.

This behavior occurred because the implemented potential failed to properly reproduce the varying charge density in response to Coulombic forces acting on the metal. In the past, this has been accounted for by a method known as the image charge method[40]. Spohr and Heinzinger[41] have previously used this method successfully to model the platinum/water interface; however, their implementation is only valid for simple macroscopic geometries that cross the periodic boundary conditions essentially producing infinite slabs.

This has been addressed by modifying LAMMPS based on the electrode charge dynamics (ECD) method developed recently by Guymon, et al.[42]. We will discuss the

electrode charge dynamics methodology in more detail as well as limitations to its implementations and the resulting simulations in a future chapter.

II.5 Magnitude and Velocity Relationship

A conclusion has yet to be made as to the relationship of the applied electric field magnitude to resulting velocity of the DNA sample. It is clear that more simulations must be performed to explore this relationship. With the new metal/non-metal potential implemented, the –0.05, -0.02, -0.01, -0.0075, -0.005, and –0.002 V/Å applied field simulations have been repeated extending the length of the simulations to 2 ns.

The task of simulating production runs to develop the magnitude/velocity relationship will require re-equilibration using the newly implemented potential. Each production run of 1 ns takes approximately two days to complete on 64 Opteron processors.

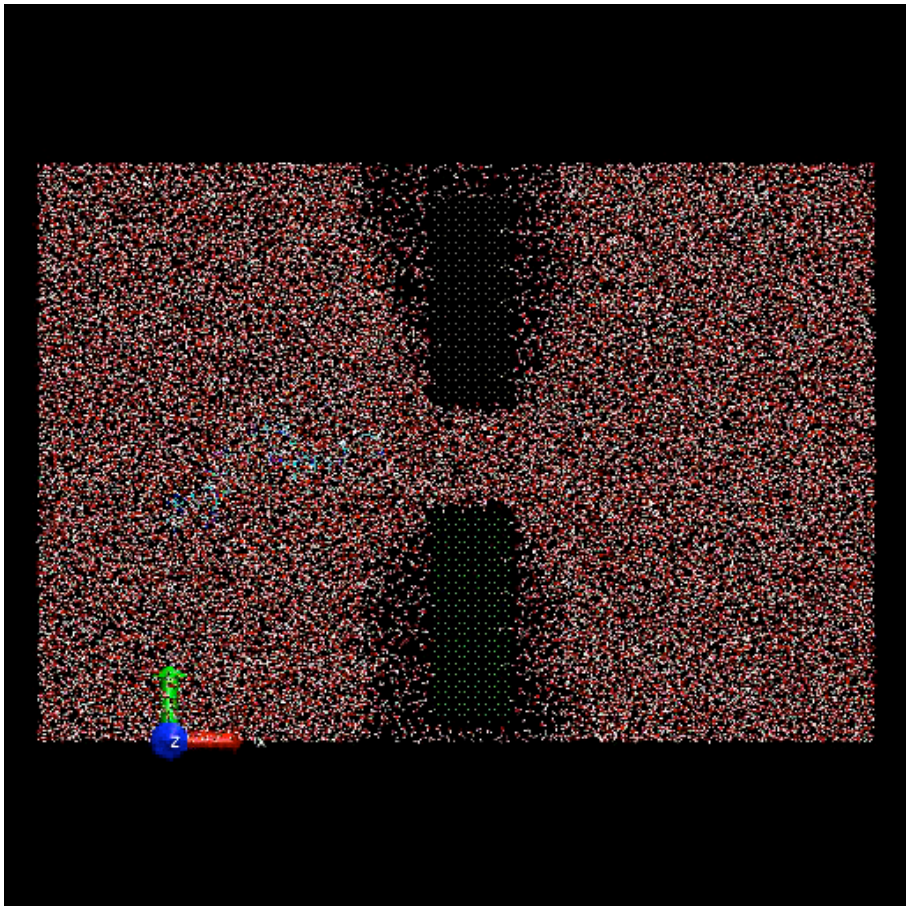

Figure 15: Equilibrated device with visualized water molecules

II.6 Identify Optimal Controlling Mechanism

The possibility exists that the application of a uniform electric field will not be sufficient to control the translocation of the DNA sample as intended. As mentioned before, the implementation of a pulsed electric field within molecular dynamics would require increased computational resources. This hurdle has forced our initial investigation into controlling mechanisms to focus on inducing flow within the solution.

II.6.A Simulation Details

The physical setup of the simulated device was exactly the same as the setup used in the electric field magnitude studies mentioned previously, including the use of the same forcefields.

The induction of flow was achieved by imposing an additional external force of equal magnitude on every atom in the solution. Production runs of 1 ns were performed for each magnitude tested.

II.6.B Results and Discussion of Flow Simulations

Simulations were performed with 0.5, 0.25, 0.05, 0.005, and 0.0001 kcal/mol-Å magnitude forces on the solution atoms. Assuming linear response behavior (i.e., that Navier-Stokes hydrodynamics is valid), these forces correspond to very large pressure drops (~ 0.5 MPa to 8 MPa over 20.7 nm) over the length of the simulation box; however, with respect to molecular dynamics, these pressure drops are negligible in comparison to fluctuations in pressure (~ 10 MPa) typically observed in molecular dynamics simulations. The simulations of 0.5, 0.25, 0.05, and 0.005 kcal/mol-Å

magnitude forces all resulted in very similar behavior to varying degrees. Figure 16 is an illustration of this behavior in which the forces on the solution atoms are so strong that the stationary constraint imposed on the electrodes cannot be maintained. Additionally, one can see that the solution atoms are moving so fast that they create void space behind the electrodes. This is clearly too fast (~ 600 m/s) to be of use in the sequencing device.

(a)

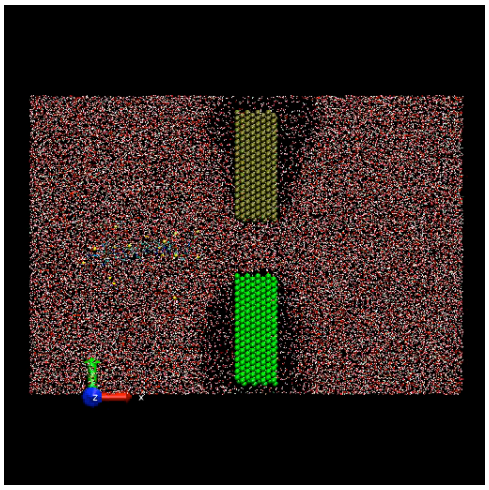

(b)

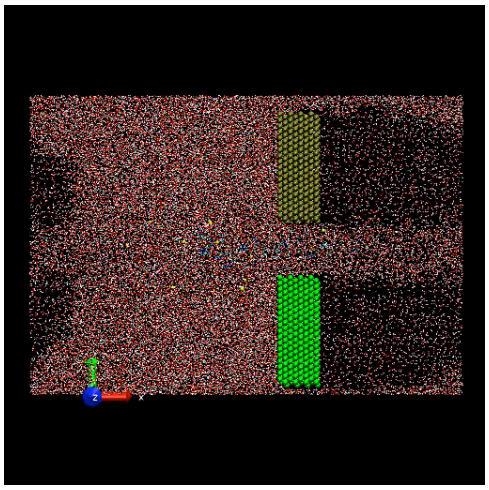

Figure 16: Snapshots of the 0.05 kcal/mol-Å magnitude force simulation of ssDNA (C_8T_8) in water at (a) 0 ps and (b) 1000 ps

In contrast, the simulation of the 0.0001 kcal/mol-Å applied force produced much more promising results. Not only did the applied force not create the void space behind the nodes, the electrodes remained stationary objects within the simulation. As in the applied electric field simulations, the velocity of the DNA strand was determined through the evaluation of the change in direction of the center of mass from its original position. Figure 17 is the plot of this change in direction for the 0.0001 kcal/mol-Å simulation. The molecule appears to have net motion away from the initial position of about 1 Å; however, the velocity varies over the course of the simulation.

Elongation of the DNA strand was noted as it was in the applied electrical field simulations. The elongation in the 0.0001 kcal/mol-Å induced flow simulation was similar to those observed in the applied field simulations. Note that applied electric field should not elongate a uniformly charge object. The molecule's end-to-end distance increased by approximately 10 Å over the course of a nanosecond as shown in Figure 18. More extreme elongation was not seen in this simulation likely because the molecule did not come close enough to the nanogate.

Preliminary simulations provide promising results that indicate induced flow may be used as a controlling mechanism. Ideally, more simulations of induced flow need to be performed at a variety of magnitudes between 0.0001 kcal/mol-Å and 0.005 kcal/mol-Å, implementing the proper metal/non-metal potential, to better understand the relationship of magnitude to velocity. Furthermore, the implementation of pulsed applied electrical fields should be examined should both uniform electrical field application and induced flow prove incapable of producing the desired motion control; however, these implementations are beyond the scope of this dissertation.

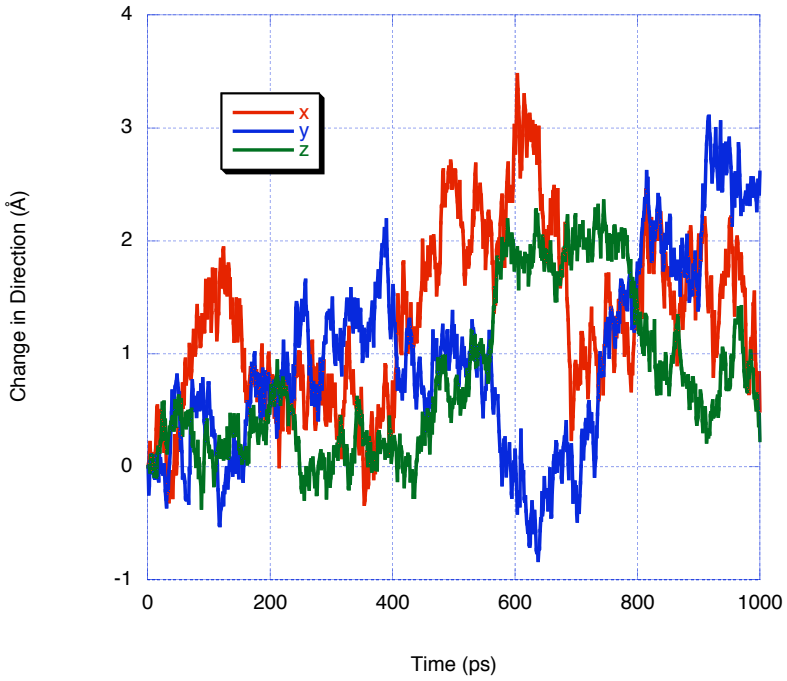

Figure 17: Change in direction vs. time based on the center of mass with an applied force of 0.0001 kcal/mol-Å

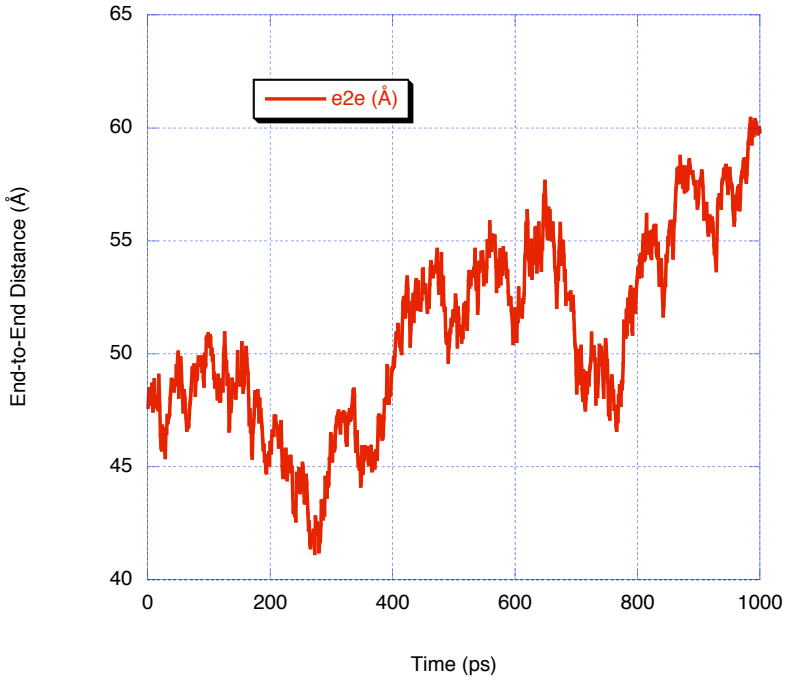

Figure 18: End-to-end distance vs. time of DNA under an applied force of 0.0001 kcal/mol-Å

CHAPTER III

ELECTROPHORETIC RESPONSE OF DNA IN SOLUTION

III.1 Motivation

Initial simulations of a given configuration of the conceptual device have shown that DNA behaves differently in the bulk solution than it does when in proximity to the electrode gate. Motivated by the similarity of the comparison of the transport properties of the ssDNA molecule in bulk solution to experimental capillary electrophoresis data and as part of the investigation into the ideal configuration of the sequencing device, we decided to perform molecular dynamics simulations of ssDNA and dsDNA in a bulk aqueous environment to directly compare the electrophoretic mobility calculated by simulation to experiment. We will examine the relationship between simulated electrophoretic mobility and experimental as a means of validating implemented force fields.

The examination of simulated electrophoretic mobility will again make use of the capillary zone electrophoresis mobility study performed by Stellwagen and Stellwagen[39] for comparison. The experimental capillary zone electrophoresis technique is easily approximated in simulation by the application of an external electric field. In this experimental study, as described in the previous chapter, single and double strand DNA 20 base pair oligomers in a buffer of 40mM Tris-acetate-EDTA at 7.6 pH were electrophoresed through a capillary coated with polyacrylamide 38.8 cm long and 100μm in diameter at 200 V/cm (2×10^{-6} V/Å). Stellwagen noted that free solution mobility of

DNA increased with increasing molecular weight up to a plateau that occurred around 170 base pairs. A relationship between sequence and mobility was also observed in this experiment; however, for the purpose of assessing consistency between simulation and experiment, we focused on two oligomers. All sequence mobilities observed in this experiment were in the range of 2.894×10^{-4} and 2.944×10^{-4} $cm^2V^{-1}s^{-1}$. With an electrophoretic field of 2×10^{-6} V/Å, these mobilities corresponded to velocities in the range of 0.00578 to 0.00588 Å/ns.

III.2 Simulation Details

We performed a series of simulations of both single and double strand DNA molecules in pure water similar to single-stranded RNA MD simulations performed by Yeh and Hummer[14] in order to more directly compare simulation results to experiment. The experiment authors, Stellwagen and Stellwagen, electrophoresed several different configurations of single strand DNA molecules as well as several double strand DNA molecules. We chose to compare our simulations to the experimental results of Stellwagen over another ssDNA electrophoretic mobility study by Hoagland[43] because of the smaller oligomers used in the Stellwagen study. Hoagland, et al. studied the electrophoretic mobility of ssDNA molecules consisting of tens of thousands of base pairs. This simulation study focused on the ssDNA oligomer denoted ssA5, which consisted of the following sequence of nucleotides, CGCAAAAACGCGCAAAAACG, as well as the dsDNA oligomer denoted dsA5, which was a double strand DNA molecule consisting of the ssA5 sequence and its complement.

The MD simulations of ssA5 and dsA5 were performed using LAMMPS with the CHARMM 27 all-hydrogen force field[26, 27]. Explicit water was described by the TIP3P model[29]. The sodium counterions were represented by a potential developed by Beglov and Roux[28]. Initial coordinates for the ssA5 and dsA5 molecules were generated using Nucleic Acid Builder (NAB)[44, 45]. The molecules were solvated and neutralized with sodium (Na^+) counterions using a script within the LAMMPS software package. At a density of 1 g/cc, 3802 water molecules solvated the ssA5 molecule in addition to 20 sodium counterions. The dsA5 molecule was solvated with 3486 water molecules and 40 sodium counterions.

The simulations utilized periodic boundary conditions and were equilibrated for 1ns using the NPT ensemble at 300 K and 101 325 Pa with the Nosé-Hoover thermostat[46] and barostat[47]. Time integration was performed using the velocity-Verlet algorithm[2] with a timestep of 2 fs. The hydrogen bonds were constrained using the SHAKE algorithm[48]. Long-range Coulombic interactions were computed using a particle-particle-particle-mesh (PPPM) solver[32].

After the equilibration period, the simulations were restarted with the addition of an applied uniform external electric field of varying magnitudes (0.003, 0.03, 0.04, and 0.05 V/Å) and run for 1.5 ns. As in the previous simulations, these applied field magnitudes were significantly larger than those typically used in capillary electrophoresis experiments due to the timescale limitations of molecular simulation.

III.3 Results and Discussion

In order to evaluate the electrophoretic mobility of the simulated DNA molecules, we first had to determine the drift velocity of the molecule. Figures 19 and 20 show the change in position of the ssA5 and dsA5 molecules, respectively, from their original position in the z-direction (the direction of the applied electric field). The change in position was evaluated by monitoring the center of mass of the molecule. The drift velocity for each applied field magnitude was determined from the slope of the relatively linear change in position over time. In most cases, the change in position over time increased as the applied field magnitude increased resulting in a larger drift velocity. The behaviors of the ssA5 molecule when the 0.03 and 0.04 V/Å fields were applied were the only exceptions. These two cases seemed to oscillate in roughly the same positions resulting in approximately the same drift velocities despite the varying field magnitude. We note that for the larger magnitude applied fields, there appeared to be an emergent "step pattern" in the change in position versus time though this behavior was not as apparent in visualizations. We conjecture that averaging $\Delta z(t)$ over many trajectories may eliminate the steps evident in the current single trajectory results reported here. This requires further study. Such behavior was not evident in electrophoresis experiments as the applied fields used experimentally were of significantly lower magnitude than those applied in simulation.

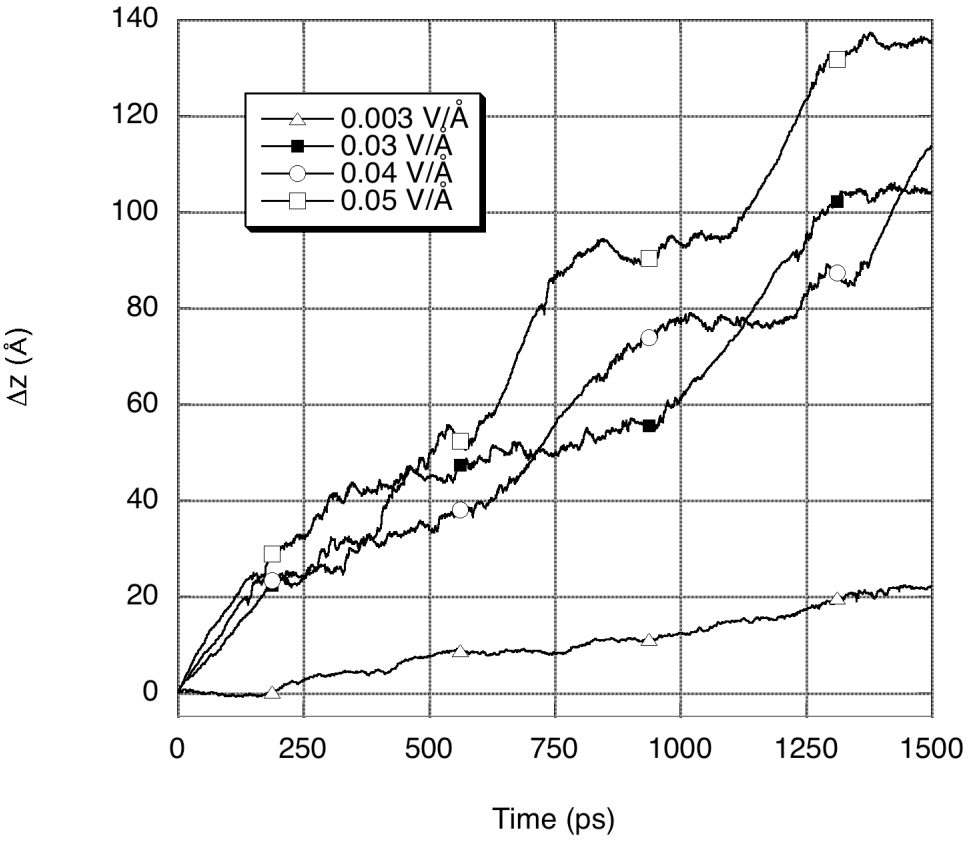

Figure 19: Center of mass motion in the z-direction for the ssA5 molecule versus time for applied fields 0.003, 0.03, 0.04, and 0.05 V/Å. The open triangles, circles, squares, and filled squares are not representative of data points but merely a method of differentiating lines

.

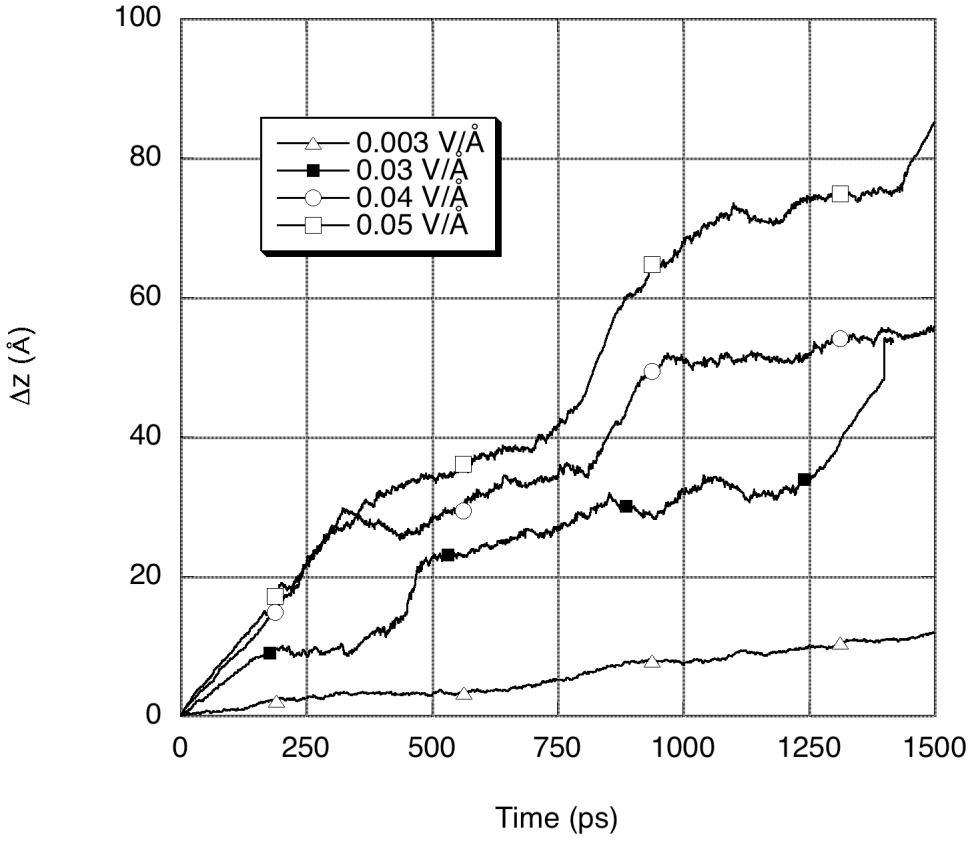

Figure 20: Center of mass motion in the z-direction for the dsA5 molecule versus time for applied fields 0.003, 0.03, 0.04, and 0.05 V/Å. The open triangles, circles, squares, and filled squares are not representative of data points but merely a method of differentiating lines

Figure 21 illustrates the correlation of the drift velocities obtained as above with the applied electric field. There is an assumed linear relationship between electric field magnitude, $\vec{\mathbf{E}}$, and drift velocity, $\vec{\mathbf{v}}$, where the electrophoretic mobility, μ, is a proportionality constant, i.e.

$$\vec{\mathbf{v}} = \mu\vec{\mathbf{E}} \tag{6}$$

Based on this relationship, we have extrapolated an experimental drift velocity for each of the simulated electric field magnitudes for comparison to simulated drift velocity. As one can see, the simulated drift velocities were somewhat lower than the extrapolated experimental values for the larger magnitude electric fields; however, the simulated drift velocities of both ssA5 and dsA5 for the 0.003 V/Å magnitude were consistent with experiment.

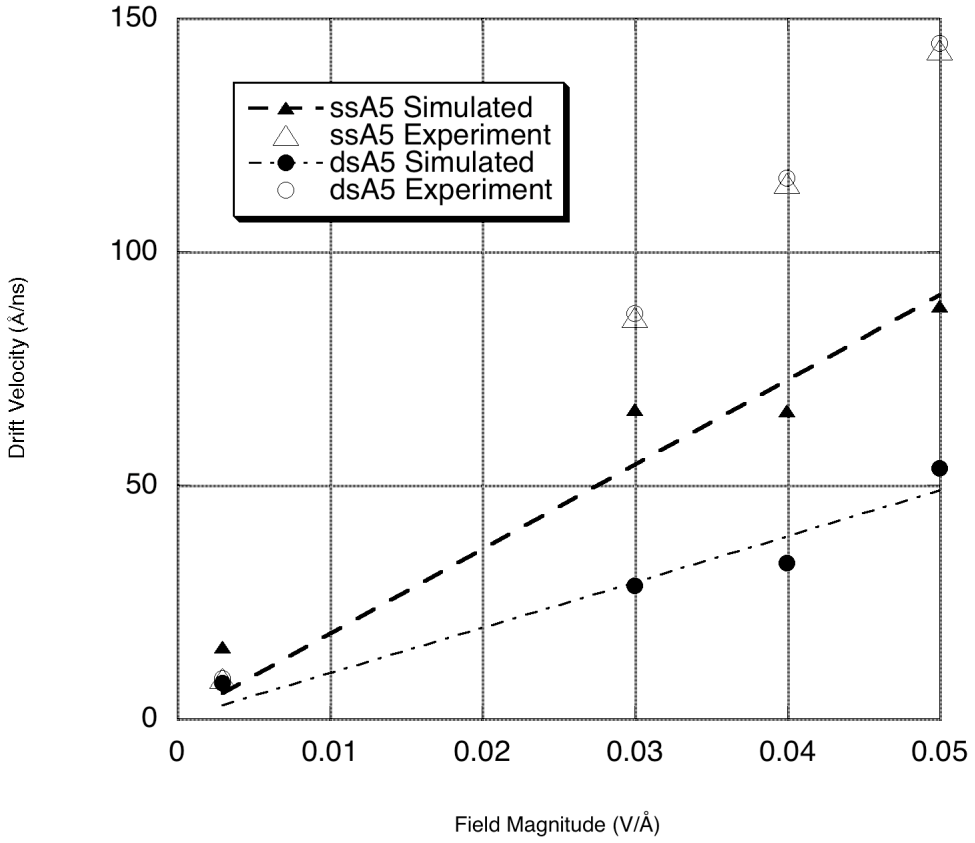

Figure 21: Drift velocity of ssA5 and dsA5 as a function of applied electric field. The dashed and dot-dashed lines are the linear fits of the ssA5 and dsA5 drift velocity vs. electric field data, respectively, through which electrophoretic mobility was determined. The experimental velocities are obtained from Equation (6) using the experimental electrophoretic mobilities.

The values of the simulated electrophoretic mobility were calculated from the slope of the linear fit to the drift velocity data. Significantly strong electric fields can result in nonlinear electrophoretic mobilities[49]; however, in experimental capillary electrophoresis and in this simulation study, the linear regime was applicable. Here, electrophoretic mobility from simulation was calculated to be 1.8×10^{-4} and 9.8×10^{-5} $cm^2\ V^{-1}\ s^{-1}$ for ssA5 and dsA5, respectively. Compared with the experimental values for ssA5 at 2.87×10^{-4} and dsA5 at 2.89×10^{-4} $cm^2\ V^{-1}\ s^{-1}$, we can see that simulation in the above described manner resulted in a lower electrophoretic mobility (by 35% for ssA5 and by 65% for dsA5). This could result from the viscosity difference of using pure water as the solvent in simulations as opposed using the buffer used in experiments. Additionally, the simulations had no physical boundary such as the experimental capillary, which could augment mobility, though in theory, this effect was corrected for in the experiments. Of more concern was that the simulated electrophoretic mobility of the larger molecule, dsA5, was smaller than that for the ssA5 molecule, while the experimental observations indicated that the larger molecule should have a slightly larger mobility. The experimental results were counter-intuitive (i.e., the experimental result indicated that the larger molecule had slightly higher mobility), and so the significance of the disagreement in the trends between simulation and experiment was difficult to gauge. Additionally, we note that the experimental mobilities for ss and dsDNA may not be statistically significantly different, once error estimates were taken into account. Though Stellwagen and Stellwagen reported no error values for the normalized mobilities, error propagation of the measured values to the normalized values used in this study indicated that the mobilities of both dsA5 and ssA5 were statistically the same.

It is interesting to note that the mobilities calculated in the bulk simulations (i.e., with no nanogate present) were lower than those found in the bulk regime of the nanogate simulation. One possibility was that the convective motion induced in the solvent by the field acting on the DNA and its counterions was enhanced in the presence of the nanogate because of the collimating effect of the nanogate, thus resulting in greater directionality of the DNA motion in the direction of the applied field. This could be tested by simulations in the presence of the nanogate in which the field is applied perpendicular to the nanogate opening.

III.4 Conclusions

We have performed simulations of two DNA molecules, ssA5 and dsA5, in bulk aqueous solution using classical molecular dynamics simulations in order to determine electrophoretic mobilities. Results from the ssA5 and dsA5 simulations in bulk water compared to initial simulations of ssDNA confined between two mica plates and experimental capillary electrophoresis experiments were inconsistent at larger applied electric field magnitudes. The simulated electrophoretic mobilities were notably smaller likely due to freedom of motion through periodic boundary conditions. Future work in this area will include the constraint of the DNA molecules in the x and y-directions as well as examining lower magnitude fields over longer timescales.

CHAPTER IV

MOLECULAR DYNAMICS SIMULATION OF ssDNA TRANSLOCATION THROUGH A COPPER NANOELECTRODE GAP

Given the results from the initial molecular dynamics study of the proposed genomic sequencing device, we decided to perform further simulations to evaluate the applicability of the metal/non-metal interaction potential. Using a fixed gap width between the electrodes and a small sample segment of ssDNA as initial starting points in this portion of the project, the effect of applied electric fields on translocation velocity was studied.

Research very similar to the proposed nanoscale sequencing device we will evaluate in this work has been reported using the classical UFF[31] potential for the interaction of the metal electrodes with water, ions, and DNA [17]; however, as we shall see below, by implementing a more appropriate metal/non-metal interaction potential known as electrode charge dynamics (ECD)[42] we obtain more realistic results as evidenced by water distributions around the metal nanoelectrodes and details of the translocation velocities measured in the simulations. Our initial studies of DNA molecules translocating through metallic electrodes have also made use of UFF in describing metal/non-metal interactions of the metal with water, ions, and DNA.

IV.1 Electrode Charge Dynamics

In comparison to the UFF potential, the ECD potential more accurately describes the phenomena of fluctuating charge density in response to Coulombic forces acting on the metal by representing valence electrons with a diffuse negative Gaussian charge-density distribution centered at each atom and representing the core electrons and the nuclei as fixed positive point charges. The magnitude of the electron charge associated with each atom is determined by an energy minimization criterion, thus permitting electron density to migrate within the metal nanoelectrode in response to the motion of charges in the fluid phase (water, ions, and ssDNA). This description of interactions is further supplemented by the addition of a modified-Morse potential utilizing parameters fitted from *ab initio* data.

The difficulty in this method lies in the necessity of determining the dynamic diffuse charge at each timestep, and thus, this code must be integrated into the time evolution scheme of the molecular dynamics code. The propagation equations as derivatives of time, t, for the diffuse charge, q_i^v, and its velocity, v_i, are as follows.

$$\begin{aligned} \frac{dq_i^v}{dt} &= v_i - \xi \\ \frac{dv_i}{dt} &= \frac{F_i}{m_q} - \zeta v_i \end{aligned} \tag{7}$$

where ξ, a parameter to correct long-term numerical drift in total electrode charge, is given below.

$$\xi = \frac{1}{n\tau}\left[\sum_{j=1}^{n}\left(q_j^v + q_j^c\right) - Q_{tot}\right] \tag{8}$$

τ is a time constant which is equal to approximately 100 timesteps. n is the number of atoms in the electrode. q_i^c is the fixed positive point charge, and Q_{tot} is the fixed total

charge. ζ, in Equation (9), is an integral-feedback control variable used to maintain the average charge temperature at the set point $\bar{T}_q$.

$$\frac{d\zeta}{dt} = \frac{T_q - \bar{T}_q}{\bar{T}_q \tau^2} \tag{9}$$

The instantaneous charge temperature is T_q given by

$$T_q = \frac{m_q}{n k_B} \sum_{j=1}^{n} v_j^2 , \tag{10}$$

where k_B is Boltzmann's constant. The choice of mass, m_q, is related to the choice of the temperature set point to maintain stability. Guymon and coworkers recommend using the following relationship.

$$m_q = k_B \bar{T}_q \left(10\,\text{ps}/|e|\right)^2 \tag{11}$$

The description of the force on each valence charge, F_i, is given by

$$F_i = \left(\frac{1}{n} \sum_{j=1}^{n} \phi_j \right) - \phi_i , \tag{12}$$

where ϕ_i is the chemical potential for the valence charge *i* given in by

$$\phi_i = \sum_{j=1}^{n} C_{ij} q_j^v + \sum_{j=1}^{n} C_{ij}^* q_j^c + \frac{\partial U_{ext}}{\partial q_i^v} + \phi_i^{set} - \mu_i . \tag{13}$$

U_{ext} is the Coulomb energy from interactions with charges external to the electrodes. ϕ_i^{set} is the user specified offset potential between two parts of the electrode. C_{ij} and C_{ij}^* are Coulomb overlap integrals given by

$$\begin{aligned} C_{ij} &= \frac{erf\left(\gamma_{ij} r_{ij}\right)}{r_{ij}} \\ C_{ij}^* &= \frac{erf\left(\gamma_i r_{ij}\right)}{r_{ij}} , \end{aligned} \tag{14}$$

where $\gamma_{ij} = (\gamma_i^{-2} + \gamma_j^{-2})^{-1/2}$, and r is the distance from the atom center. μ_i is a Lagrange multiplier used to constrain the diffuse charge to negative or zero, which has been chosen to yield an exponential repulsion barrier, *viz*

$$\mu_i = -\frac{k_B \overline{T}_q}{Q_u} \exp\left(\frac{q_i^v}{Q_u}\right). \tag{15}$$

The stiffness parameter, Q_u, is 0.01 |*e*|. The solutions to the above equations are substituted into the following equation to obtain the Coulombic potential energy, U.

$$U = \frac{1}{2}\sum_{i=1}^{n}\sum_{j=1}^{n} q_i^v q_j^v C_{ij} + \sum_{i=1}^{n}\sum_{j=1}^{n} q_i^v q_j^c C_{ij}^* + \frac{1}{2}\sum_{i=1}^{n}\sum_{\substack{j=1,\\ j\neq i}}^{n} q_i^c q_j^c \frac{1}{r_{ij}} + \sum_{i=1}^{n} q_i^v \phi_i^{set} + U_{ext} \tag{16}$$

To supplement this Coulombic potential as mentioned previously, a modified Morse potential given by

$$U(r) = -\varepsilon\left(1 - \left\{1 - \exp\left[-A\left(r - r^*\right)\right]\right\}^2\right) \tag{17}$$

is added to Equation (16). The three parameters, ε, A, and r^*, are found through fitting the potential to the difference between *ab initio* and ECD interactions.

The ECD method has been tested for applicability through simulations of water-NaCl solution at a copper interface resulting in marked improvement in the representation of electrochemical interfaces. The method logically extends to other metals, and we have obtained improvement in representing the behavior of water near the electrode surface.

Past methods of accounting for valence electron migration have included the image charge method[40] of which Spohr and Heinzinger[41] successfully implemented to model a platinum/water interface. However, the image charge method is based on macroscopic electrostatics, and so is only valid for simple geometries in which the

surface crosses periodic boundaries resulting in an infinite slab, essentially eliminating its applicability to nanoscopic (i.e., non-macroscopic) metal objects. Hence, the ECD method offers a significant opportunity for more accurate descriptions of ion-metal, water-metal and ssDNA-metal interactions in realistic sequencing device configurations.

Initial simulations similar to the previously mentioned work utilizing the UFF potential will be compared to simulations utilizing the alternate ECD potential. We demonstrate that the choice of interaction potential between the metal and water significantly impacts the behavior of the electrically driven DNA translocation behavior.

IV.2 Computational Method

The classical molecular dynamics simulations were performed using a modified version of the LAMMPS (Large-scale Atomic/Molecular Massively Parallel Simulator)[24, 25] simulation package. The LAMMPS code was modified and extended to incorporate ECD. This procedure included the definition of new pair potentials for metal-metal and metal-solution interactions with Gaussian type charge distributions, a new charge dynamics class with methods controlling the amount of negative charge located at individual metal atoms, and additional variables carrying atomic properties required by the ECD method, such as chemical potential. The proper function of the code was tested by comparison with the data published in the original paper[42] and to independent simulations run with our own in-house code which implements ECD.

The initial set of simulations was of a nanoscale sequencing device consisting of two mica plates separated by approximately 3 nm; the solvated DNA and water are enclosed between the plates. Each plate measured 20.7 nm x 14.4 nm. The detection

nodes were constructed of two copper FCC lattices measuring approximately 2 nm x 5 nm x 3 nm and separated by a 2.87 nm gap, as measured from center-to-center of the outermost copper atoms. Copper nanoelectrodes, rather than the Pt and Au nanoelectrodes being fabricated for the actual device, were used in this study since Cu is the only metal for which ECD parameters have been published to date[42]. Obtaining ECD parameters requires extensive *ab initio* calculations; the ECD interaction plus a Morse potential are then used to extract the parameters required for the ECD model[42]. At the moment, the 2.87 nm gap has been the only gap distance evaluated through simulation. Future simulations will investigate the gap size, as well as other developmental design details, including developing ECD parameters for metals other than Cu. The ssDNA strand used in the present study consisted of sixteen nucleotides, eight consecutive cytosines followed by eight consecutive thymines. The ssDNA was solvated in water at a density of 1g/cc. The ssDNA strand was surrounded by sodium ions to make the total system charge neutral. The number of atoms in this simulation totaled 132,697. The total dimension of the simulation box was 20.7 nm x 14.4 nm x 5.0 nm (including mica atoms). The simulations were periodic in the *x* and *y* directions and fixed in the *z* direction represented in LAMMPS as a slab separated by a large vacuum space. Note that the mica surfaces were parallel to the *x*-*y* plane.

Interaction potentials varied based on the atom type. The nucleic acids were described using the CHARMM27 all-hydrogen potential[26, 27]. The sodium ions were represented by a potential developed by Beglov and Roux[28], included in the CHARMM potential. Water molecules were described by the rigid water model known as TIP3P[29] with which the CHARMM potential has been optimized. A more rigorous water

potential was unnecessary in comparison to the need for computational efficiency for such a large system. The mica surfaces and the copper nodes were treated as rigid bodies in this set of simulations. As such, their interactions with other atoms were estimated by Lennard-Jones potential with parameters determined by Lorentz-Berthelot mixing rules. The CLAYFF potential[30] parameters were used for mica, and the UFF potential parameters were used for copper. Note that, according to the experimental studies of Klein[50] and the simulations of Leng and Cummings[51, 52], fluidity of water confined between two mica surfaces is maintained under extreme confinement (down to mica-to-mica separations of 0.7nm). The mica-to-mica distance used in this study was approximately 3 nm, and so was much larger than the distances at which nanoconfinement influences the fluidity of liquid water. Thus, based on these results[50-52]we expect that the behavior of the water confined between the mica sheets will be bulk-like.

All simulations began with an equilibration period of 1 ns. Simulations were performed using the NVT ensemble at 300K with a Nosé-Hoover thermostat[46]. Time integration was performed using the velocity-Verlet algorithm with a 2 fs timestep[2]. Hydrogen bonds were constrained using the SHAKE algorithm[48]. The particle-particle particle-mesh (PPPM) solver was used to compute long-range Coulombic interactions[32]. The ssDNA strand was positioned at the entrance of the gap between the electrodes, which will be referred to here as the nanogate. This positioning alleviated the need to examine ssDNA conformational effects on the transport behavior. Experimentally, proper alignment of the ssDNA strand to ensure translocation will have to be addressed, most likely through the use of nanofluidic transport to the nanogate.

After the equilibration period, the simulations were subjected to an applied uniform electric field and performed for 2 ns. This uniform field was applied in the *x*-direction in order to force the ssDNA to translocate through the nanoscale gap. In an attempt to develop a relationship between translocation velocity and magnitude of the applied electric field, the field was varied between 0.0005 V/Å and 0.5 V/Å. In the actual device, the electric field is better described as an effective potential varying based on position within the device. The applied fields (0.0005, 0.001, 0.0025, 0.005, 0.0075, 0.01, 0.02, and 0.05 V/Å) correspond to effective transmembrane voltages drops of 1, 2, 5, 10, 15, 20, 40, and 100 mV; however, for the purpose of describing the relationship to velocity, we will refer to the applied field magnitude. In the future, examining pulsing electric fields as a driving force would be desirable though extremely computationally expensive. Additionally, the proper positioning of the ssDNA strand between the electrodes may necessitate the use of a holding field perpendicular to the mica surface.

A second set of simulations was performed exchanging the UFF potential used to describe the metal/non-metal interactions by the more appropriate ECD potential. Based on the UFF simulations, the size of the simulation box was reduced to obtain more efficiently information about transport behavior (in essence, to eliminate some of the bulk water that did not contribute to transport). In this case, the simulation box was 15.6 nm x 14.4 nm x 5 nm totaling 107, 545 atoms. All other simulation details remained the same as described for the initial simulation set.

Due to the intense computational requirements of simulations this size, the following results shown are of single trajectories. While ensemble averages would be useful in generalizing behavior, we believe that the results presented still properly

illustrate the transport phenomena, and in particular, demonstrate clearly the impact of the use of ECD.

IV.3 Results

This section presents results first from the simulations utilizing the UFF potential and second from the simulations utilizing the ECD methodology. The resulting translocation velocity and relationships to applied electric field are studied and compared.

IV.3.A. UFF Potential

The results in this section make use of the UFF potential as described in the methodology section. This potential was initially chosen to represent the metal/non-metal interactions in part because of its wide use[53-57], its availability in existing molecular dynamics software packages, in addition to its relative simplicity, while accepting its limitations in describing variable charge density in metallic surfaces.

A significant goal of this project is to develop a relationship between translocation velocity of the ssDNA sample and the applied electric field magnitude. In doing so, the transport behavior of the ssDNA strand was evaluated over the application of eight electric fields of magnitudes 0.0005, 0.001, 0.0025, 0.005, 0.0075, 0.01, 0.02, and 0.05 V/Å. Using the center of mass of the ssDNA strand as a position reference, the change in position was determined by taking the difference of the current position from the original position and plotting this difference versus time thus making the slope the resulting translocation velocity. Figure 22 is the plot of the change in center of mass in the x-direction as a function of time for the set of UFF simulations. The magnitude of the

applied field resulted in a variety of behaviors in the ssDNA. The 0.05 V/Å field evoked rapid and uncontrollable translocation with slightly less speed than that observed for the 0.02, 0.01, and 0.0075 V/Å fields. The 0.005 and 0.0025 V/Å fields appeared to result in motion though not in an apparently field-related fashion as the lower magnitude field produced more forward motion in this instance. The two lowest magnitude fields, 0.0005 and 0.001 V/Å, resulted in mostly oscillatory behavior. An important feature of note is the change in position over time was that of the delayed forward motion obvious in the 0.02, 0.01, and 0.0075 V/Å trajectories. The 0.05 VÅ field was large enough to overcome the energetic barrier hindering motion, and the smaller magnitude fields were not large enough to result in translocation (at least over the timescale of 2 ns).

Figure 23 contains snapshots from the 0.01 V/Å simulation following 1 ns of the applied external field for both UFF and ECD. It is immediately apparent from this illustration that the use of the UFF potential to describe metal/non-metal interactions was inadequate. Since the copper nanoelectrode has no net charge, the UFF model for a copper atom in the nanoelectrode is a simple Lennard-Jones interaction. Thus, UFF essentially represents the copper surface as a hydrophobic entity resulting in extremely low-density regions surrounding the electrodes. Such low density within the vicinity of the nanogate does not yield an accurate picture of the transport behavior. We believe this hydrophobic representation of the copper nodes resulted in the energetic barrier to forward motion noted above.

(a)

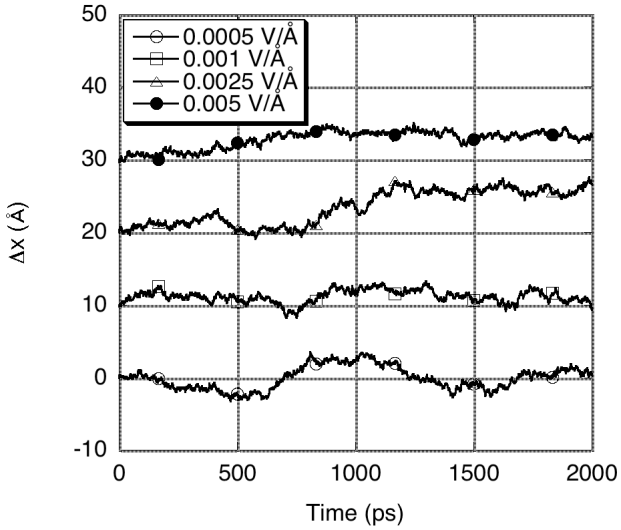

(b)

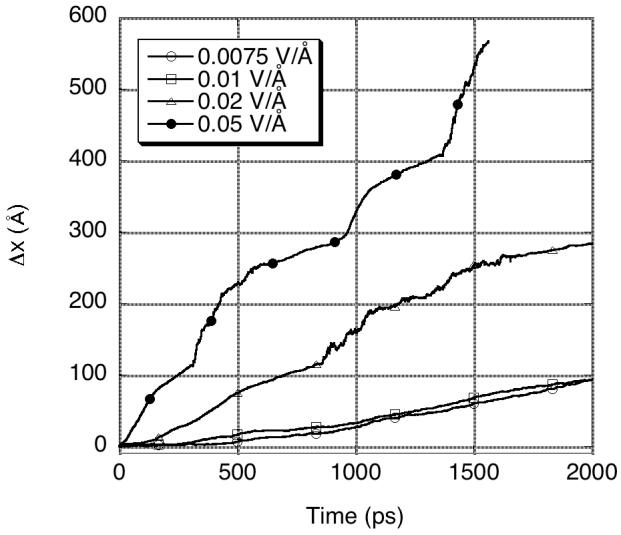

Figure 22: Change in position in *x*-direction vs. time based upon the center of mass resulting from the application of an external electric field (UFF potential simulations). Figure a shows the four lowest magnitude applied fields. Note that the origin of each curve is shifted upwards by 10Å for clarity. Figure b shows the four highest magnitude applied fields.

(a)

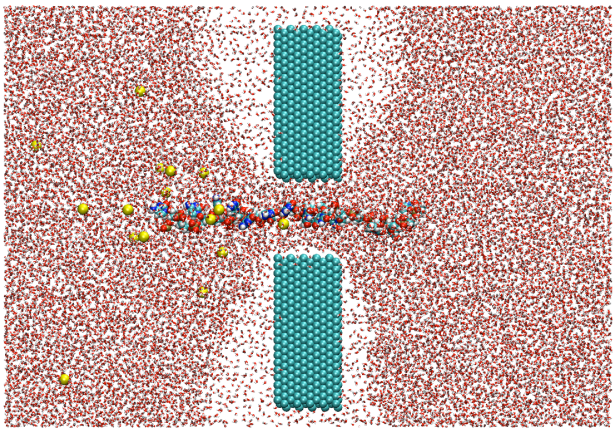

(b)

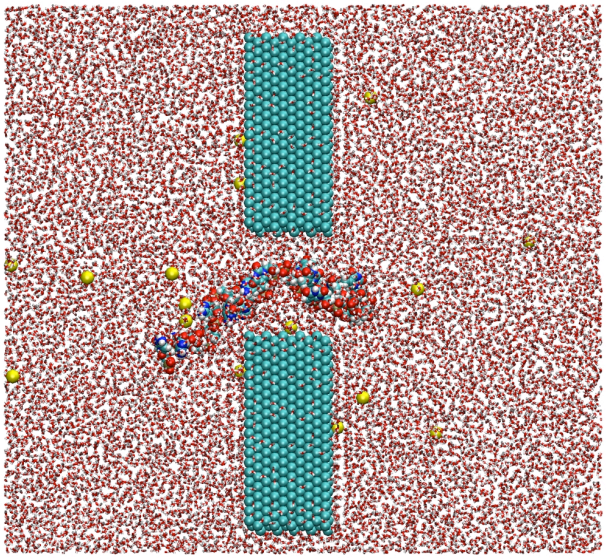

Figure 23: Snapshot of the 0.01 V/Å simulation at 1 ns utilizing (a) UFF and (b) ECD

IV.3.B. ECD Method

To address the significant shortcomings of the initial simulations resulting from the use of the UFF potential, we performed the same set of simulations with the more appropriate ECD potential in its place. It is apparent from visualization alone that the new potential has much improved the physical behavior of non-metals in the presence of the copper electrodes. The water molecules no longer formed low-density regions, more closely resembling actual experimental operating conditions, as shown in Figure 23(b). Further discussion of the density profiles resulting from both potential implementations will be presented below.

Using the same method of determining change of position mentioned previously, we have obtained Figures 24(a) and 24(b), which are plots of the change in position of the center of mass in the x-direction over time for the simulations utilizing the ECD potential. Note that the applied electric field was also applied to the electrodes, resulting in a response within the Cu nanoelectrode. An immediately noticeable difference in the trajectories compared to the UFF trajectories is that the lower magnitude applied fields resulting in forward motion, as opposed to oscillatory behavior, have done so from the beginning of the field application. The implementation of the ECD potential has most notably eliminated the energetic barrier to motion observed in the initial set of simulations. We expect that this was partly due to the charge polarization of the nanoelectrodes, which should result in an additional attractive interaction between the nanoelectrodes and the (negatively charged) ssDNA. As one would expect, the application of an external electric driving force resulted in the immediate response of the ssDNA strand and a more linear trajectory within the appropriate regime. Over the course

of the 2 ns simulation, the 0.001 V/Å simulation trajectory did not appear, however, to correspond to the expected trend of forward motion. We expect that this was a fluctuation, and that averaging over multiple 0.001 V/Å simulation trajectories would show, on average, forward motion. In the context of the fluctuation theorem[58, 59], the reported 0.0005 V/Å and 0.001 V/Å simulation trajectories were exhibiting regions of negative entropy production (motion in the opposite direction to the applied field). Thus, this behavior is to be expected, and we conjecture that with sufficient averaging and classification the trajectories of the ssDNA could be shown to follow the predictions of the fluctuation theorem for the relative probability of the duration of negative and positive entropy-producing states.

The mica surface, being composed of ions, has a net dipole moment. If the upper and lower mica surfaces are replicates of each other, the effect of the mica surface dipoles is additive. Thus it is interesting to ask whether the direction of the mica dipole (in our simulated system, the mica dipole is predominantly in the positive *x* direction) and the direction of the applied field (in our simulated system, the applied field is predominantly in the positive *x* direction) are coupled significantly. Figure 24 (b) shows the trajectory of the ssDNA strand within the device when the uniform electric field is applied in the direction opposite that of the mica dipole (all other trajectories are that of the applied field in line with the mica dipole). The dipole resulting from the mica is larger than the other components of the device; however, in comparison to the volume occupied by the device, the mica dipole is relatively small. Nonetheless, there was clearly some impact of the direction of the mica dipole on the trajectories; further investigation of this phenomenon is beyond the scope of the present project.

(a)

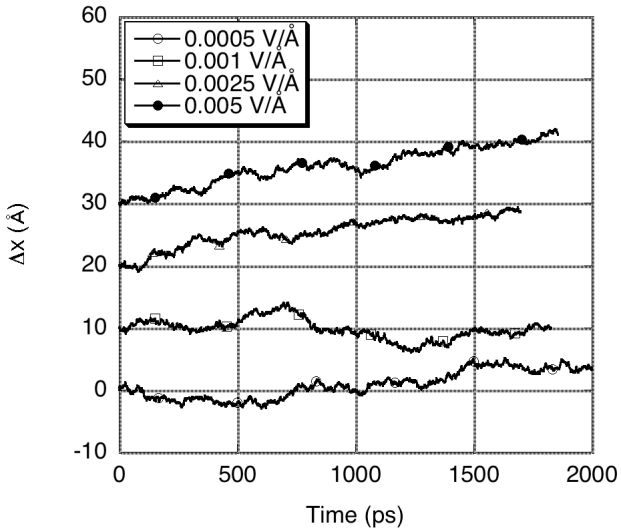

(b)

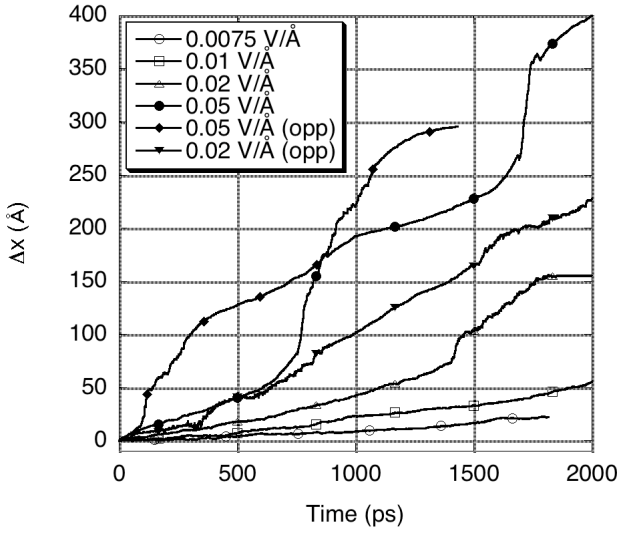

Figure 24: Change in position in *x*-direction vs. time based upon the center of mass resulting from the application of an external electric field (ECD potential simulations). Figure a shows the four lowest magnitude applied fields. Note that the origin of each curve is shifted upwards by 10Å for clarity. Figure b shows the four highest magnitude applied fields.

IV.4 Discussion

In order to directly compare the results of the two simulation sets, the translocation velocity has been obtained from the slope of the trajectories in Figures 22 and 24 and plotted against the electric field magnitude. The simulation translocation velocity values are also compared to results from simulations of the ssDNA strand in bulk water in Figure 25. The bulk water simulations were performed using the same methodology as our previous bulk ssDNA simulations described in Chapter III and elsewhere[60].

Figure 25 reiterates the fact that the lower magnitude fields of the UFF simulations resulted in very similar translocation velocities until the electric field became large enough to overcome the resistance to motion created by the UFF potential interactions. It appears that this resistance to motion is largely dependent on the ability of the ssDNA strand to recruit a sufficient number of water molecules to surround it while traversing the nanogate. The ECD simulations resulted in more linear response to applied electric fields.

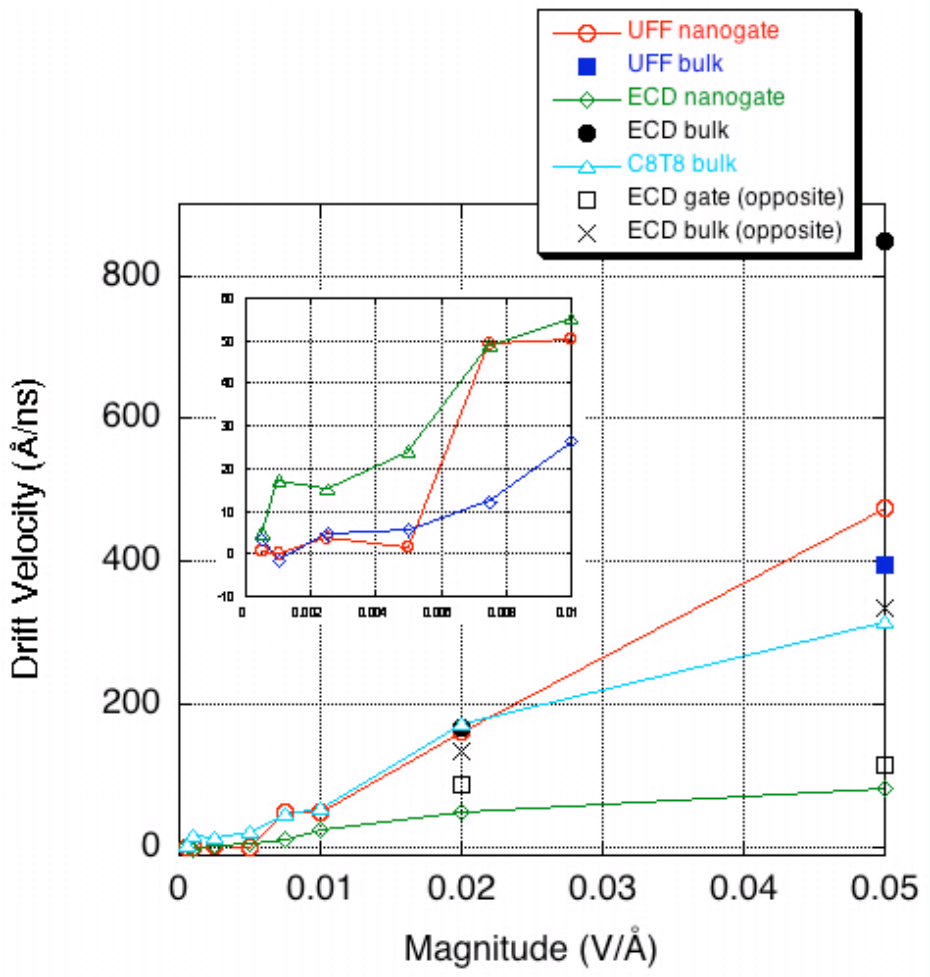

Figure 25: Translocation velocity vs. electric field magnitude for UFF and ECD simulation sets

Breaking the velocity analysis into regimes (i.e. in the vicinity of the nanogate or in the bulk) gives a better picture of the translocation behavior than an overall velocity. The translocation velocity of the ssDNA in the nanogate regime of the ECD simulations was slower than that of the strand surrounded by bulk water. This would appear to result from the fact that the ECD will result in a DNA-nanoelectrode net attraction that would not be present in the UFF simulations; hence, it is not surprising that the UFF nanogate-translocation velocities were more like bulk behavior, consistent with the absence of the electrostatic attraction. The bulk behaviors of the ECD and UFF simulations are also intriguing. The UFF results for translocation through water were much closer to the bulk simulations of translocation through water, while the ECD results resulted in faster translocation through water. We interpret these results as having their origin in the impact of the applied field on the nanoelectrode and the ssDNA-nanoelectrode interaction. Both of these factors will result in more attraction between the ssDNA and the nanoelectrodes, resulting in an additional force on the ssDNA moving it through the bulk water. Both of these effects were absent from the UFF simulations, and so it is reasonable that the UFF results differ little from bulk simulations.

All simulations were started in the nanogate regime with the exception of the two ECD simulations applying the electric field in the opposite direction of the existing mica dipole. The simulations in which the 0.05 V/Å field was applied in the direction opposite of the mica dipole, the resulting bulk translocation velocity was lower than that of the simulation of the same magnitude applied in the direction of the mica dipole. The translocation of the ssDNA strand in the vicinity of the nanogate remained largely unchanged, however, for both the 0.02 and 0.05 V/Å magnitudes as does the bulk

translocation of the 0.02 V/Å simulation. This deviation may be due to starting the strand in different regimes or possibly to the non-linearity of the electrophoretic response of molecules in the presence of large magnitude electric fields. Electrophoretic mobility, proportionally related to translocation velocity, will be linear with respect to applied field for sufficiently weak fields. Experimentally applied electric fields in which linear electrophoretic response can be observed are typically on the order of $2*10^{-6}$ V/Å, which is smaller than the smallest field presented here in this study. The gap between the 0.02 V/Å and the 0.05 V/Å translocation velocity results may represent the range at which this linear to non-linear transition occurs. As a matter of note, a similar non-linear transition in ionic conductivity for a different system has been reported for the same magnitude applied electric fields[61]. These results give credence to the notion of using an electrical field as the controlling mechanism within the proposed sequencing device. It should also be noted that the proposed experimental device is planned to be operated in what we would deduce from our simulations to be the linear regime (<0.02 V/Å). Non-linear response will have little effect on the operation of the actual device as the applied fields expected to be used experimentally will be below the 0.02 V/Å value. A brief description of non-linear field effects has been provided in Appendix C. In the case considered here, the nonlinear field effect on the electrophoretic velocity is likely due to the structure of the DNA and/or the solvent differing in high field compared to their structure on the absence of an applied field (the equilibrium structure). We have not investigated this in detail, but in general nonlinear field effects are associated with changes in structure away from the equilibrium molecular structure.

To further evaluate the applicability of the UFF and ECD potentials with regard to the simulation environment, simulations with the ssDNA strand absent were performed in order to obtain the water density profile across the nanogate. These simulations were simply equilibrations of the previously mentioned systems with the ssDNA strand and ions replaced by water molecules performed under the exact same constraints. Figure 26 is the density profile from the center of a copper atom of one electrode to the center of a copper atom in the next over the course of 1 nanosecond.

It is clear from Figure 26 that the UFF potential resulted in an unreasonably low-density region between the nanogate. Without the presence of the ssDNA strand in the nanogate, the UFF potential caused near-complete drying of the nanogate. By contrast, the ECD potential made the electrodes hydrophilic as shown by the density peaks at contact in Figure 26. Through the center of the nanogate, however, the ECD potential yielded the appropriate bulk-like density of approximately 1 g/cc. This difference in density in the vicinity of the nanogate is significant when evaluating the transport behavior of ssDNA in the proximity of the electrodes. The density profile does not go to zero at the edge of the electrodes as some water molecules managed to slide into the space between the electrodes and the rigid mica surface.

Also of interest is the density profile from mica surface to mica surface in the bulk regime of device. Figure 27 is the density profile between the center of the outermost potassium ions on the mica surfaces derived from the same 1ns simulation as the density profile in Figure 26. In the bulk of the device, it appears the choice of potential for metal/charge interactions has little effect on the density of the system.

However, the bulk behavior is not the most important aspect affecting translocation velocity and behavior.

IV.5 Conclusions

Molecular dynamics simulations of the ssDNA electrophoretic translocation through a copper nanogate have been performed using both the UFF and ECD potentials in order to fully investigate the applicability of each potential as well as to investigate the possibility of using an external field as a method of controlling translocation velocity in the proposed nanoscale sequencing device. Though the results were not entirely conclusive in regards to the utility of applying electric fields as translocation control, it is clear from the combination of the ECD nanogate response and the qualitative physical response of water to the copper electrodes using the ECD potential that ECD should be chosen over UFF for accurate description of molecular interactions. The ECD potential more closely approximated actual operating density values across the nanogate in addition to producing translocation velocities aligned with the expected electrophoretic response both in trend and quantity. Future work in this area should make use of the ECD potential for a more accurate physical description.

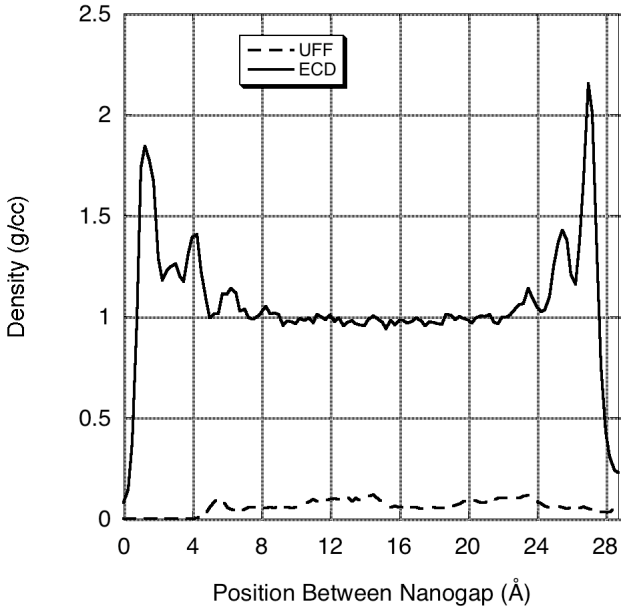

Figure 26: Density profile across the nanogate utilizing the UFF and ECD potential. Note that the distance between the peaks at each surface is approximately 2.5 nm for the ECD method.

(a)

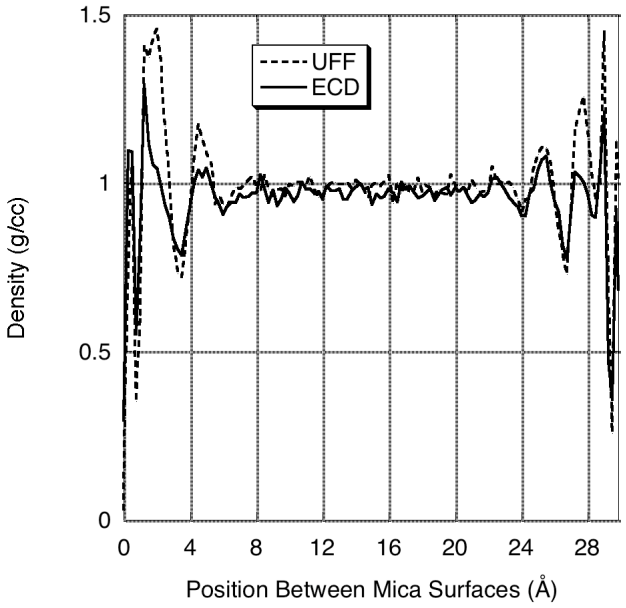

(b)

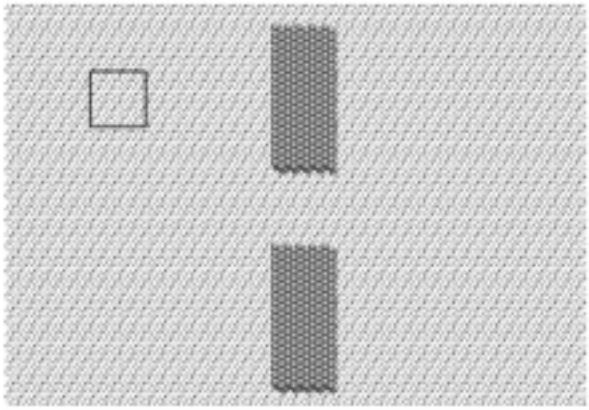

Figure 27: (a) Density profile across mica surfaces utilizing the UFF and ECD potential. (b) Bulk area from which density profile in (a) was obtained is marked by the square in the upper left of the device picture.

CHAPTER V

ELECTROPHORESIS OF ssDNA THROUGH NANOELECTRODE GAPS: IMPACT OF GAP WIDTH

V.1 Introduction

In this study, through the use of molecular dynamics simulations, we attempt to address one of the fundamental questions, namely, the physical behavior of the translocating DNA in the sequencing device and its response to the basic device design variable, the nano gap width (i.e., the nanoscopic distance between the two nano-electrodes).

Our previous simulations[37] of the proposed sequencing device shown in Figure 1 focused on the effects of the applied electric field on the translocation velocity of the ssDNA strand, in addition to the proper application of interaction potential. It was concluded that use of an applied electric field would provide sufficient force to initiate forward motion through the nanoscale gap, though the actual magnitude and shape of the field necessary has yet to be determined as it is dependent on other variables such as DNA strand length, solvent viscosity, and gap width. In the simulations presented in this chapter, we examine the effect of changing the gap width on the translocation of ssDNA through the nanoscale gap. We demonstrate that the gap width clearly has a significant impact on the ability of the ssDNA strand to effectively translocate. In addition, our simulations indicate a threshold value for which the ssDNA will enter and thread the gap during the course of a molecular dynamics simulation. we will also present the modified-Morse fit results for platinum to be applied in the ECD method.

V.2 Computational Method

V.2.A System Setup

Each simulation performed was of a nanoscale sequencing device consisting of two mica plates separated by approximately 3 nm; the solvated DNA, counterions, and water are enclosed between the plates. Each plate has dimensions of 20.7 nm x 14.4 nm. The detection nodes were constructed of two platinum FCC lattices measuring approximately 2 nm x 5 nm x 3 nm. The separation distance of these nodes was measured from center to center of the outermost platinum atoms. We considered values of 1.5, 1.75, 2.0, 2.25, 2.5, 2.75, 3.0, and 3.25 nm. These values are the nominal gap width. The effective gaps are usually about 0.3 nm narrower than the nominal gaps because of the van der Waals radius of the metal atoms determining the gap. The ssDNA strand used in the present study consisted of sixteen nucleotides, eight consecutive cytosines followed by eight consecutive thymines. The strand was solvated in water at a density of 1g/cc, and was surrounded by 15 sodium ions in solution to make the total system charge-neutral. The number of atoms in each of these simulations varied slightly but all eight simulations were of approximately 138,000 atoms. The total dimension of the simulation box was 20.7 nm x 14.4 nm x 5.0 nm (including mica atoms). The simulations were periodic in the *x* and *y* directions. The z direction was modeled by a slab geometry as described before. These boundary conditions allow the DNA strand to continue movement across boundaries in the x and y direction and reduces computational expenditure, since the 3-D slab geometry technique for PPPM is less computationally demanding than using a 2-D Ewald method[33]. Note that the mica surfaces were parallel to the *x*-*y* plane.

The ssDNA strand was positioned at the entrance of the gap between the electrodes, which will be referred to here as the nanogate. The head ssDNA residue is lined up with the nanogate such that the lead hydrogen atom on the backbone is exactly even with the x-position of the first row of platinum atoms comprising the nanogate. This positioning alleviated the need to examine ssDNA conformational effects on the transport behavior. Experimentally, proper alignment of the ssDNA strand to ensure translocation will have to be addressed, most likely through the use of nanofluidic transport to the nanogate.

V.2.B Force Fields

The nucleic acids were described using the CHARMM27 all-hydrogen potential[26, 27]. The sodium ions were represented by a potential developed by Beglov and Roux[28], included in the CHARMM potential. Water molecules were described by the rigid water model known as TIP3P[29] with which the CHARMM potential has been optimized. A more rigorous water potential was unnecessary in comparison to the need for computational efficiency for such a large system. The mica surfaces and the platinum nodes were treated as rigid bodies in this set of simulations. As such, their non-electrostatic interactions with other atoms were calculated by Lennard-Jones potential with parameters determined by Lorentz-Berthelot mixing rules. The CLAYFF potential[30] parameters were used for mica, and the ECD methodology was used for the platinum atoms. Note that, according to the experimental studies of Klein[50] and the simulations of Leng and Cummings[51, 52], the fluidity of water confined between two mica surfaces is maintained under extreme confinement (i.e., mica-to-mica distances of less than 1 nm); hence, we

expect that the water confined between the mica surfaces in our simulation (with mica-to-mica distances of 3 nm) will exhibit fluidity similar to that of bulk water.

V.2.C ECD Platinum Parameters

As discussed in the previous chapter, the ECD method more accurately describes the phenomena of varying charge density in response to Coulombic forces acting on the metal by representing valence electrons with a diffuse negative Gaussian charge-density distribution and representing the core electrons and the nuclei as fixed positive point charges. This description of interactions is further supplemented by the addition of a modified-Morse potential utilizing parameters fit from *ab initio* data.

In order to use the ECD method in these simulations, or for any simulation using metal other than copper, we must first fit a modified-Morse potential,

$$U(r) = -\varepsilon\left(1 - \left\{1 - \exp\left[-A\left(r - r^*\right)\right]\right\}^2\right) \tag{18}$$

to the difference between the *ab initio* and ECD Coulombic interactions. In Equation (18), U is the potential energy, r is the distance from the atom center, and ε, A and r^* are the adjustable parameters,.

Density functional theory (DFT) data for the interaction of a water molecule with a platinum (111) surface was obtained from Meng and coworkers[62]. The TIP3P water geometry and charges were used for the ECD calculations and simulations. ECD Coulombic interactions were determined from a sample surface of 64 platinum atoms in a FCC (111) lattice consisting of four layers of platinum atoms with a vacuum region of approximately 13 Å, in order to mimic the DFT study setup. The water molecule was held directly over a top site (i.e. directly above a platinum atom) because this position has

been shown to be the most favorable adsorption site. Ideally, the water molecule lies almost flat on the surface with its polar axis making an angle (θ) of 13º to 14º at approximately 2.43 Å above the top site. The energy was calculated as the water molecule was moved in a variety of positions. The first set of energies shown in Figure 28a was determined as the molecule was moved vertically from the top site maintaining the 13-14º angle. The second set shown in Figure 28b was determined as the molecule was held at 2.43 Å above the top site, and the surface-molecule angle was varied. Negative surface angle indicates the molecules hydrogen atoms were facing the platinum surface. Positive surface angles indicate the hydrogen atoms were facing the vacuum region.

The fit was determined using Excel solver to perform weighted least squares regression. The fit was weighted to the ideal distance above the surface and ideal angle with the surface because of their importance in description. Table 1 gives the values we obtained and used in the above-described simulations.

(a)

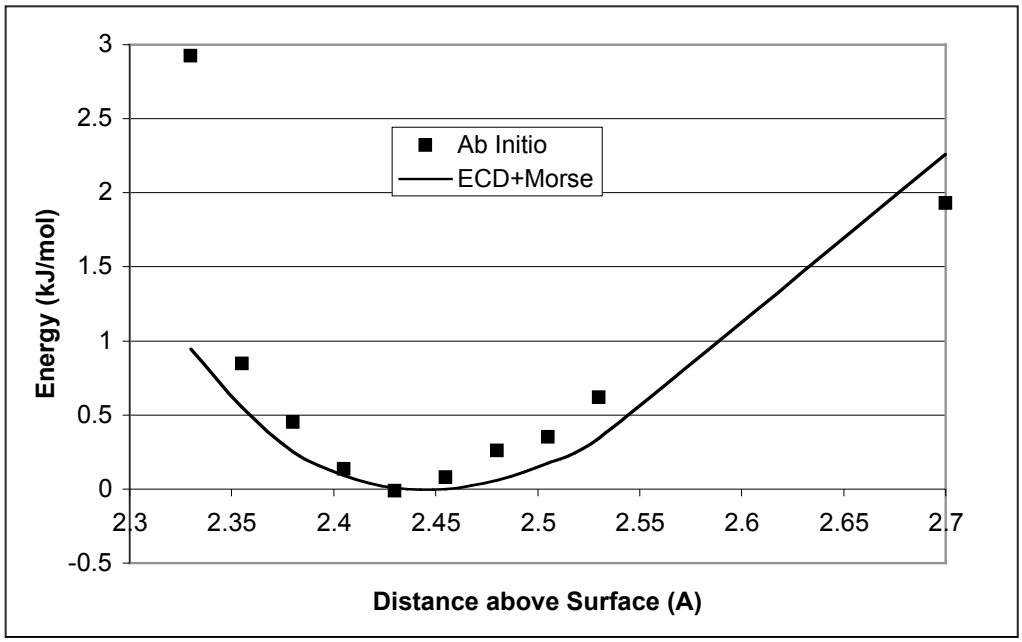

(b)

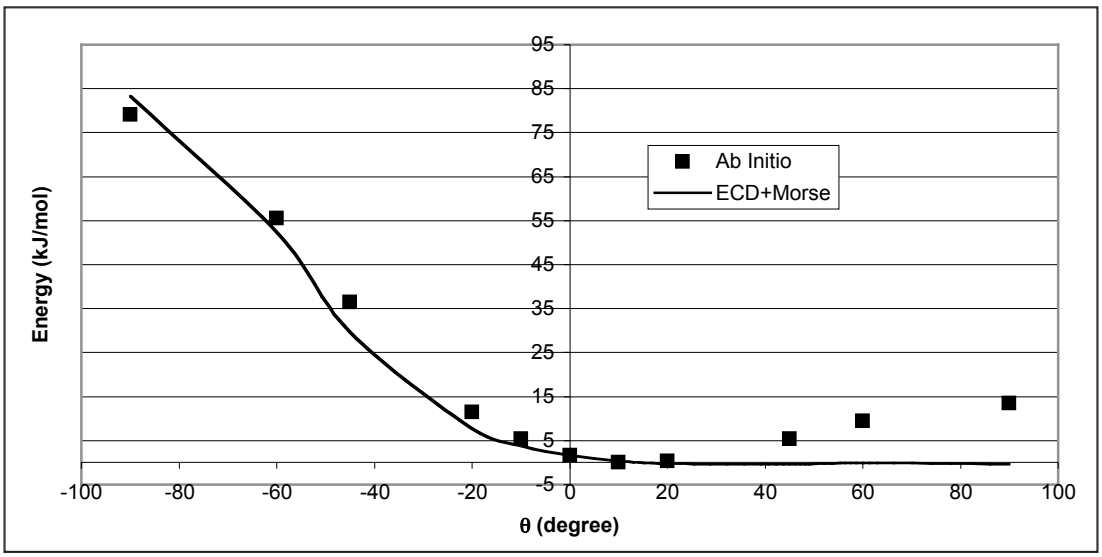

Figure 28: Modified-Morse potential fit for Pt(111) ECD parameters. (a) Energy as water molecule is moved vertically from the surface and (b) energy as water molecule is tilted from the surface holding the oxygen atom 2.43 Å above the platinum top-site.

Table 1: Interaction parameters for use with modified-Morse potential for Pt (111).

	O	H
ε, kJ/mol	0.831	1.621
A, $Å^{-1}$	2.000	2.320
*r**, Å	3.073	2.768

Additionally, the ECD methodology involves two additional parameters, q^c, core charge, and γ, an inverse-width parameter, to characterize the polarization behavior of the metal. In the ECD method, the metal ions are represented as positively charged spheres, whose charge has the same magnitude as the valence electron charge per atom; hence, for platinum, the charge on the core of the platinum ion q^c is 1.0 |e|. The ECD method assigned a Gaussian electron charge distribution to each atom to represent the valence electrons. The inverse of the width of this distribution, γ, for platinum is obtained by fitting to the *ab initio* calculations to be 0.751 $Å^{-1}$. The ECD parameters for platinum have not previously been published and represent a new finding in this work. In the ECD method[42], the magnitude of the charge associated with each metal ion fluctuates in response to interactions with charges outside the surface (e.g., partial charges in the water molecule) subject to the overall constraint of the total charge on the metallic nanostructure (zero in our case). In this way, the effect of valence electron mobility within the metallic nanostructure is taken into account; in a macroscopic system, this same mobility is taken into account via image charges.

V.2.D Simulation Details

The classical molecular dynamics simulations were performed using the modified version of the LAMMPS (Large-scale Atomic/Molecular Massively Parallel Simulator)[24, 25] simulation package as described in the previous chapter.

All simulations began with an equilibration period of 430 ps. Simulations were performed using the NVT ensemble at 300K with a Nosé-Hoover thermostat[46]. Time integration was performed using the velocity-Verlet algorithm with a 2 fs timestep[2].

Bonds involving hydrogen atoms were constrained using the SHAKE algorithm[48]. The particle-particle particle-mesh (PPPM) solver was used to compute long-range Coulombic interactions[32].

After the equilibration period, the simulations were subjected to an applied uniform electric field of 0.02 V/Å, corresponding to an effective transmembrane voltage drop of 40 mV, and a production run of 1 ns was performed. This uniform field was applied in the *x*-direction in order to force the ssDNA to translocate through the nanoscale gap. For the sake of computational expense, a uniform field was used without the additional perpendicular holding pulse as proposed in the original device design. Note that the results shown below are of single trajectories. While ensemble averages would be useful in generalizing behavior, we believe that the results presented still properly illustrate the transport phenomena, and in particular, demonstrate clearly the impact of the gate width on translocation behavior.

V.3 Results

The results of the platinum nanogate gap width on the translocation of the ssDNA strand has been evaluated here through examination of the trajectories in the ssDNA molecule's center of mass along the *x*-direction as well as the molecule's end-to-end distance.

The center of mass was used as the point of reference for the molecule's motion in this study. Figure 29 shows the change in center of mass in the *x*-direction versus time. From this slope of each of these lines, we determined the translocation velocity.

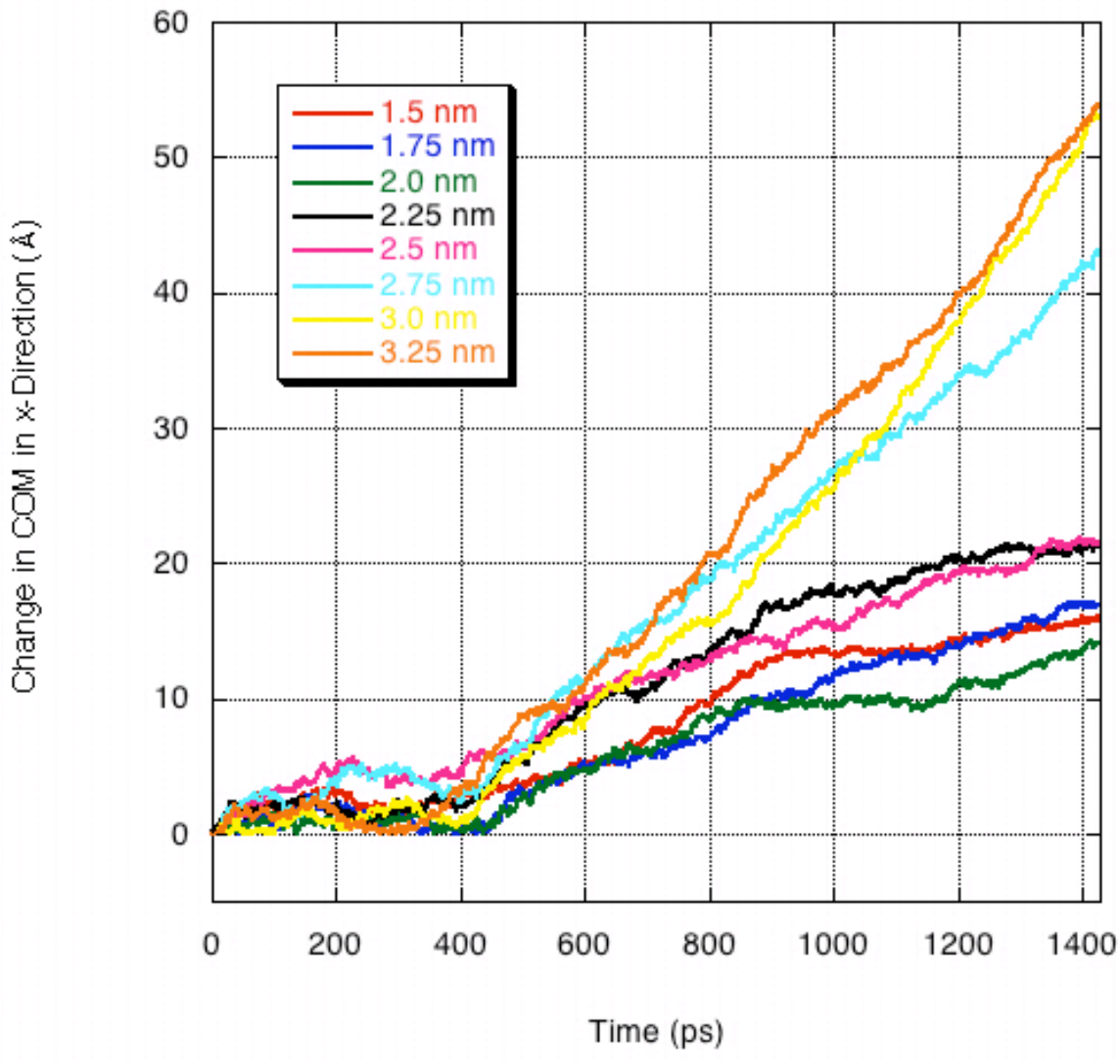

Figure 29: Change in position in *x*-direction vs. time based upon the center of mass resulting from the application of an external electric field.

After the 430 ps equilibration period, the application of the applied electric field in the *x*-direction forced the ssDNA molecule in the direction of the nanogate. The sodium ions moved in the opposite direction as a result of their positive charge. It is evident from Figure 29 that the gap distance between the values of 2.5 nm and 2.75 nm represents the point at which translocation was no longer observed within the timescale we simulated. The 20 Å change in center of mass exhibited by the non-translocating gap distance simulations represents the distance the center of mass traveled as the molecule deformed at the entrance of the nanogate. In the simulation of the 2.5 nm gap width, the ssDNA molecule begins to enter to the nanogate; however, the molecule does not translocate within the timescale (1 ns) of the production run. We cannot rule out the possibility that, after a much longer time than we are able to simulate via molecular dynamics, the ssDNA strand will translocate through a nanogate width smaller than the 2.75 nm threshold value observed in our simulations. It should also be noted that the application of higher electric fields could force the ssDNA strand through a narrower nanogate impermeable at smaller fields; however, the applied field used here was determined though previous simulations to yield a slightly higher translocation velocity than experimentally desired. In order to gain insight into the prototypical device design, we used the applied field considered reasonable for desired translocation velocity. The nanogate widths for which ssDNA could not translocate, 1.5, 1.75, 2.0, and 2.25, nm, force the molecule into a deformed conformation in front of the gate opening as shown in Figure 30.

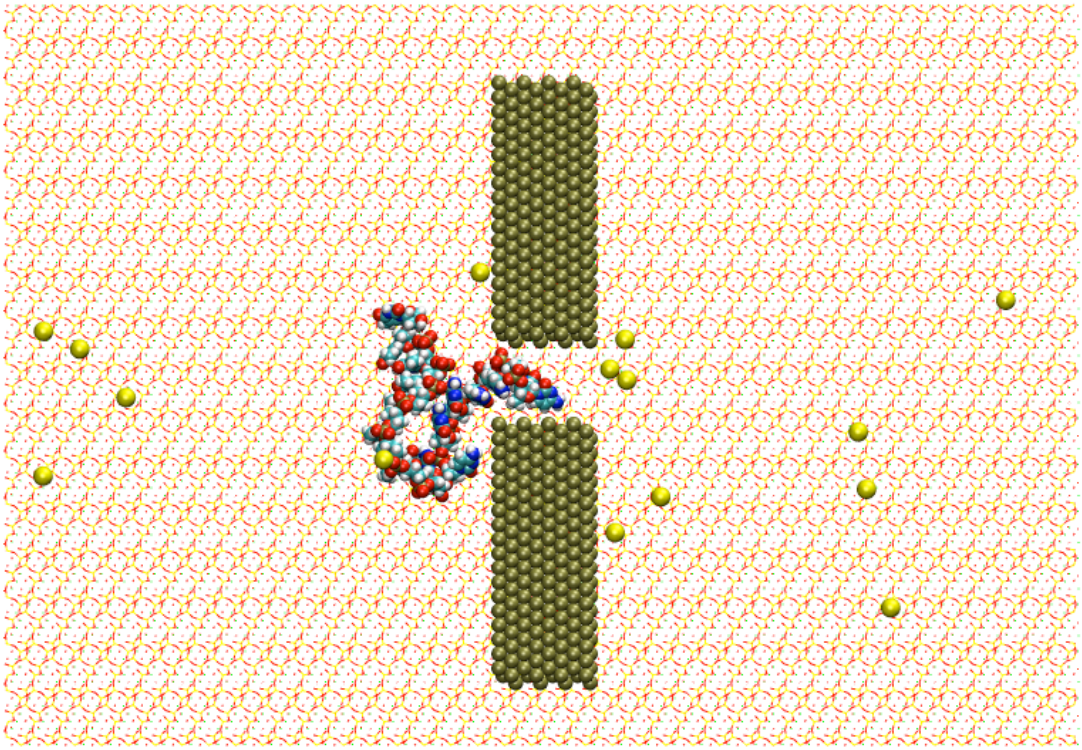

Figure 30: Snapshot of 1.75 nm gate width simulation after 1 ns production run (water not shown for clarity).

The gate configurations for which translocation occurred, i.e., 2.75, 3.0, and 3.25 nm, generally allowed so with minimal change in configuration aside from the expected molecular elongation as shown in Figure 31. It also appears that the gate width had little effect on the effective translocation velocity of the ssDNA. Translocation velocities obtained from the slopes of 2.75, 3.0, and 3.25 nm gate widths were 37.4, 49.8, and 48.7 Å/ns, respectively. Given these values were obtained from single trajectories, these are essentially the same translocation velocities for the three different gate widths.

Further examination of the effect of the gate width on the ability of ssDNA to translocate included the evaluation of the end-to-end distance of the ssDNA molecule as measured between the C5' of the first cytosine and the C2' of the last thymine. Figure 32 is the plot of the end-to-end distance versus time for each gate width examined.

As shown in Figure 32 and as mentioned before, the smaller gap widths force the molecule into a deformed configuration making the end-to-end distance progressively smaller. The three widths allowing translocation do not exhibit the compaction, and instead exhibit elongation of the DNA as it pases through the nanogate, as would be expected. The 2.75 and 3.0 nm gate widths maintain approximately the same end-to-end distance as the initial structure while the ssDNA strand elongates slightly beyond the initial end-to-end distance in the 3.25 nm width simulation.

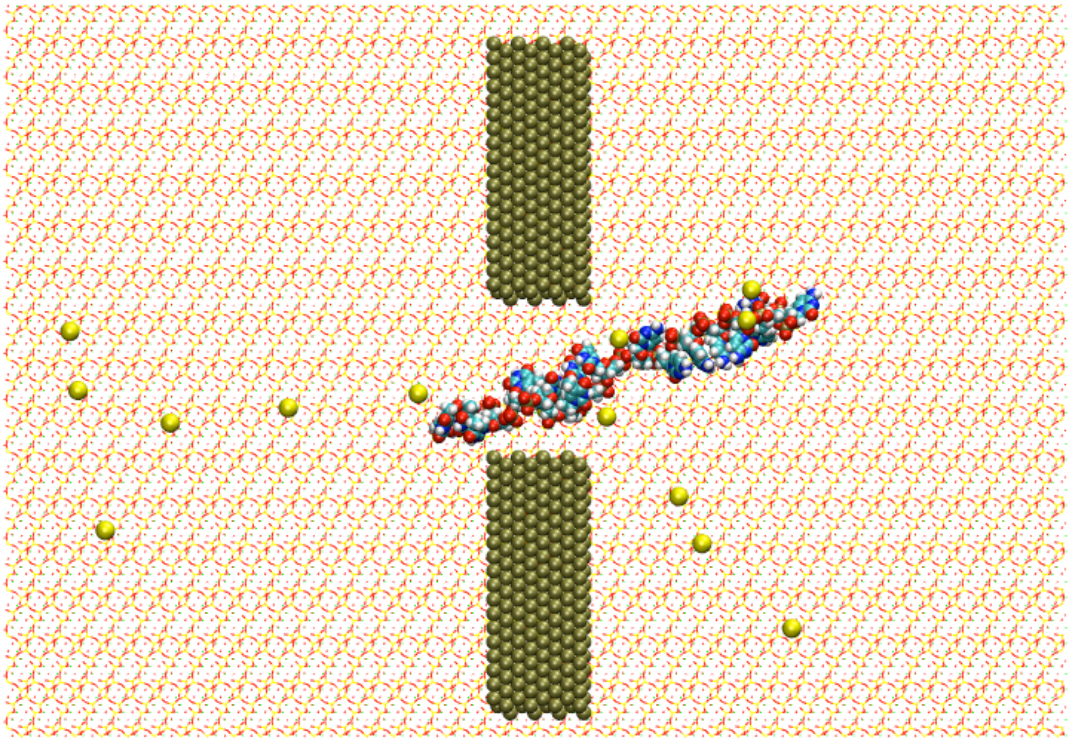

Figure 31. Snapshot of 3.25 nm gate width simulation after 1 ns production run (water not shown for clarity).

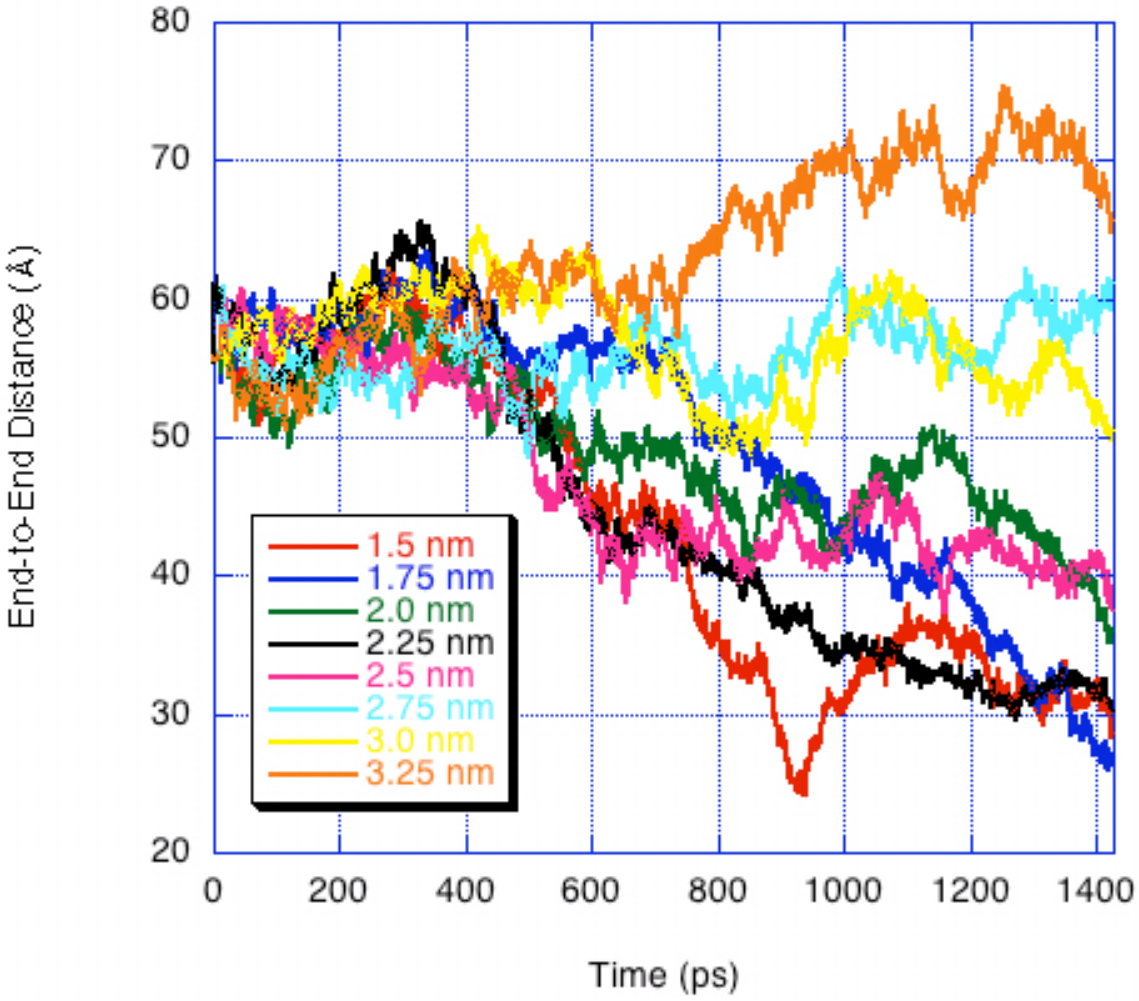

Figure 32: End-to-End distance vs. time as measured between the carbon atoms of the first and sixteenth residues.

Figure 32 serves as an explanation why the threshold gap width found in this work is large when compared with other previous studies of synthetic nanopore translocation[63]. Heng, *et al*. determined that ssDNA can permeate Si_3N_4 pores less than 1 nm in diameter under the influence of low electric fields. Single-stranded DNA, as opposed to the typical double-stranded DNA molecule, allows for more flexibility in translocation, enabling the molecule to readily translocate in smaller pores. However, in our simulations, we find that the ssDNA would fold rather than translocate and experience significant deformation thus increasing its effective characteristic dimension. We suggest that the folding is caused by the strong ssDNA-electrode attraction induced by electrostatic interactions with the metal modeled by ECD. Additionally, in the system used by Heng *et al*., the double-conical nanopore limits the molecular deformation at the entrance to the narrowest portion of the pore. The pore length examined by Heng et al. was much larger than we have simulated (10 nm as opposed to 2 nm) with an advantage of 1 nm of the helix being threaded within the pore at the start of the simulation, whereas in our simulation the ssDNA begins outside the pore. Also of note is the 8kT energetic barrier to translocation of ssDNA through an α-hemolysin protein pore discovered by Henrickson *et al*.[64]. This suggests that a minimum amount of applied field is necessary solely to enter the nanopore. This energy may be quite different than that required in the system devised by Heng *et al*., precluding the entrance to the rigid metallic nanopore used in our simulation in some cases.

For the purpose of clarifying visually what is occurring through the application of the ECD methodology, we have presented the simulation trajectory in Figure 33 of the 3.25 nm gate width visualizing the change in charge. Red represents positively charged

atoms, and blue represents negatively charged atoms. We can see the application of the external potential tends to charge the electrodes in a positive to negative fashion from left to right. The backbone of the DNA strand is negatively charged and hence attracted to the electrodes. In our previous applied field study, we determined that the ssDNA strand travels rapidly through the bulk due to this attraction to the nanogate. Additionally, we can see that the application of ECD to describe the electrostatic potentials does indeed allow for charge density variation in response to the environment in the vicinity of the metal atoms.

(a)

(b)\

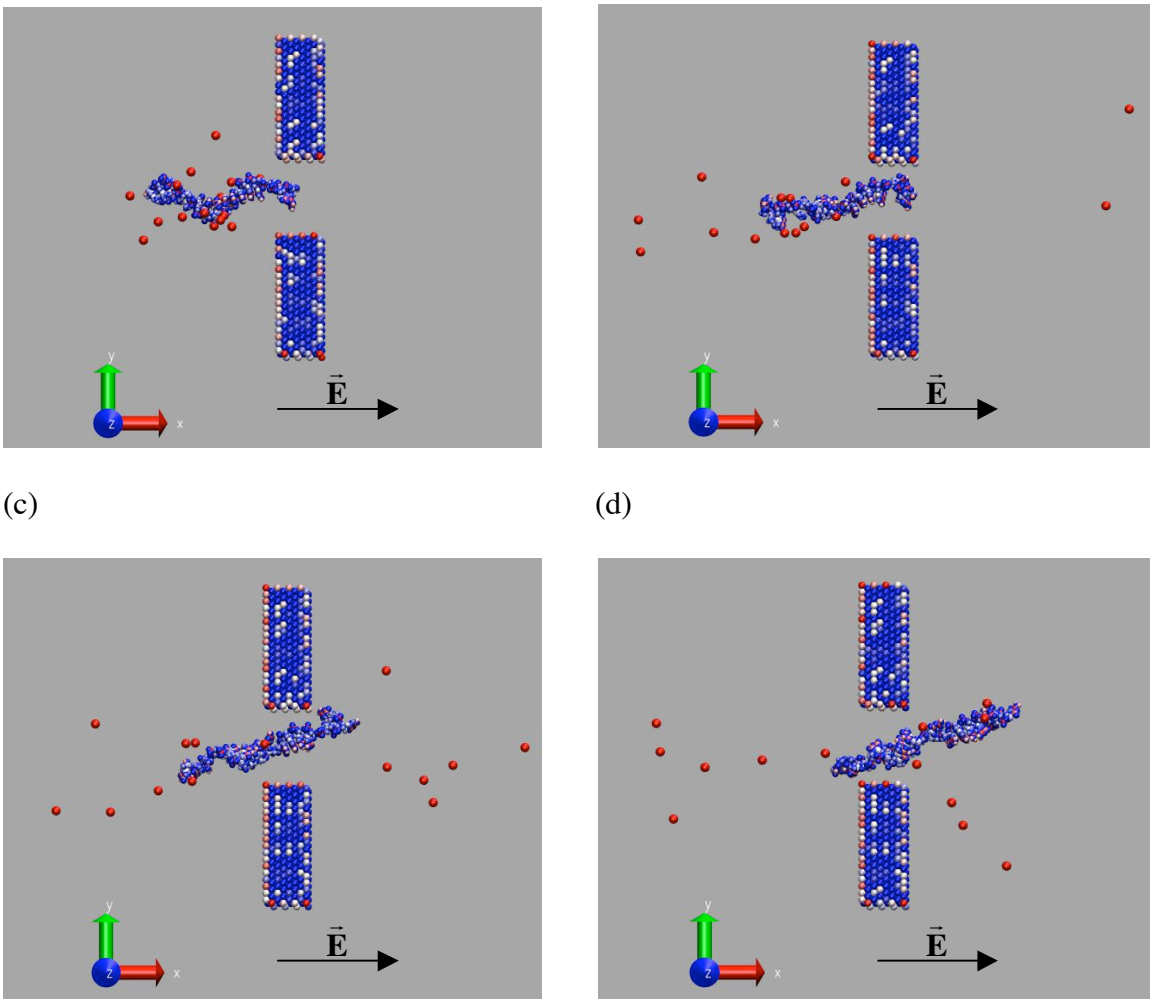

(c)

(d)

Figure 33: Snapshots of the 0.02 V/Å applied field simulation of ssDNA (C_8T_8) in water through the 3.25 nm gate at (a) 0 ps, (b) 250 ps, (c) 500ps, and (d) 1000 ps. Red indicates positive charge, and blue indicates negative charge. White is the mid-point of the charge gradient.

V.4 Conclusions

Molecular dynamics simulations of the ssDNA electrophoretic translocation through a platinum nanogate have been performed in order to fully investigate the gate width design variable. As expected, there exists a specific gate width for which the ssDNA strand will no longer translocate over the time scale of the simulation. For the applied field of 0.02 V/Å, the strand will not translocate through a gate width smaller than approximately 2.5 nm. The application of a stronger electrophoretic driving field might be able to force the strand through a smaller gate opening over the time scale simulated; however, we chose to use an experimentally relevant magnitude field in the simulation to yield desired translocation velocities as determined by our previous studies. Once the gate is large enough to allow translocation, the actual size of the gate appears to be irrelevant. The translocation velocity appears to be largely insensitive to the gate width beyond the minimum. However, we expect that if the gap is large enough to allow folding within the gap, this may impact translocation velocity. The translocation velocities observed for the translocating gate widths are roughly the same as the approximately 40 Å/ns translocation velocity we infer from simulations for a similar ssDNA molecule in bulk water[60] at the same applied field, which in turn is consistent with experimental results for translocation in bulk. The threshold value we have found in our simulations is larger than previously examined systems; however, there are many differences in the simulations to consider including the ssDNA, the initial conditions, pore geometry and nature of the pore, so that comparisons are difficult to make.

CHAPTER VI

ELECTROPHORESIS OF ssDNA THROUGH NANOELECTRODE GAPS: IMPACT OF SAMPLE LENGTH

VI.1 Introduction

This chapter presents the results of a set of simulations designed to examine the effect the DNA sample length has upon translocation velocity. Using the same simulation setup as previous simulations, we have introduced seven different length ssDNA strands varying from 4 to 48 nucleotides in length. Ideally, we would be able to compare finite length strand behavior to infinite (within the scale of simulation) length behavior; however, we are limited in scope by the size of our simulated device and the electrostatic cutoff value as well as by computational resources. We will present velocity results for translocating strand lengths as well as explanation for non-translocating molecules.

VI.2 Computational Methods

Each simulation performed was of a nanoscale sequencing device consisting of two mica plates separated by approximately 3 nm; the solvated DNA, counterions, and water are enclosed between the plates. Each plate has dimensions of 20.7 nm x 14.4 nm. The detection nodes were constructed of two platinum FCC lattices measuring approximately 2 nm x 5 nm x 3 nm. The separation distance of these nodes was measured from center to center of the outermost platinum atoms. We used a constant value of 3.0 nm. This value is a the nominal gap width as the effective gaps are usually about 0.3 nm narrower

than the nominal widths because of the van der Waals radius of the metal atoms confining the gap.

The ssDNA strand used in the present study consisted of a varying number of nucleotides solvated in water at a density of 1g/cc. The strands were comprised of a repeating sequence of cytosine, thymine, adenine, and guanine (CTAG). We evaluated seven different strand lengths denoted as CTAG, 2CTAG, 4CTAG, 6CTAG, 8CTAG, 10CTAG, and 12CTAG. The number in the abbreviation refers to the number of times the base CTAG is repeated (i.e., 4CTAG refers to the nucleotide sequence CTAGCTAGCTAGCTAG). The ssDNA strand was surrounded by an appropriate number of sodium ions to make the total system charge-neutral (3 for CTAG, 7 for 2CTAG, 15 for 4CTAG, etc.). The number of atoms in each of these simulations varied slightly but all seven simulations were of approximately 138,000 atoms. The total dimension of the simulation box was 20.7 nm x 14.4 nm x 5.0 nm (including mica atoms). The simulations were periodic in the *x* and *y* directions and fixed in the *z* direction. Note that the mica surfaces were parallel to the *x*-*y* plane.

The ssDNA strand was positioned at the entrance of the gap between the electrodes, which will be referred to here as the nanogate. The head ssDNA residue is lined up with the nanogate such that the lead hydrogen atom on the backbone is exactly even with the x-position of the first row of platinum atoms comprising the nanogate. This positioning alleviated the need to examine ssDNA conformational effects on the transport behavior. Experimentally, proper alignment of the ssDNA strand to ensure translocation will have to be addressed, most likely through the use of nanofluidic transport to the nanogate. We will present evidence to this effect shortly.

The details of the force field application are the same as has been presented in Section V.2.B. Likewise, the information regarding simulation equilibration and production methodology is the same as presented in Section V.2.D.

VI.3 Results

The results of the effect of strand length on the translocation of the ssDNA strand has been evaluated here, just as we have done in past evaluations of design variable behavior, through examination of the trajectories in the ssDNA molecule's center of mass along the *x*-direction as well as the molecule's end-to-end distance.

The center of mass was used as the point of reference for the molecule's motion in this study. In this study, as opposed to the previous variable studies, we used the center of mass of the first four residues instead of the entire molecule to get a more representative indication of trajectory. Figure 34 shows the change in center of mass in the *x*-direction from its original position versus time. From the slope of each of these lines, we determined the translocation velocity. This translocation velocity is presented in Table 2. The first 430ps are the equilibration steps referred to in the simulation details. At 430 ps, the 0.02 V/Å applied field has been applied to the ssDNA, ions, and platinum nodes.

Ideally, the molecules would translocate smoothly upon application of the external electric field. However, as seen here, the molecules did not translocate ideally. The 4CTAG, 8CTAG, and 10CTAG samples either stuck to the electrode or formed a compact conformation preventing proper translocation, thus, reducing velocity. The most notable trajectory here is that of the 4CTAG sample. This particular molecule was

particularly attracted to the metal electrodes. This attraction prevented linear translocation. The remaining part of the strand was forced through the nanogap and a bent conformation within the electrodes formed. Figure 35 illustrates through snapshots the molecular deformation as described for the 4CTAG sample. If the molecules had translocated ideally, we would have seen that the translocation velocity is relatively the same regardless of the chain length.

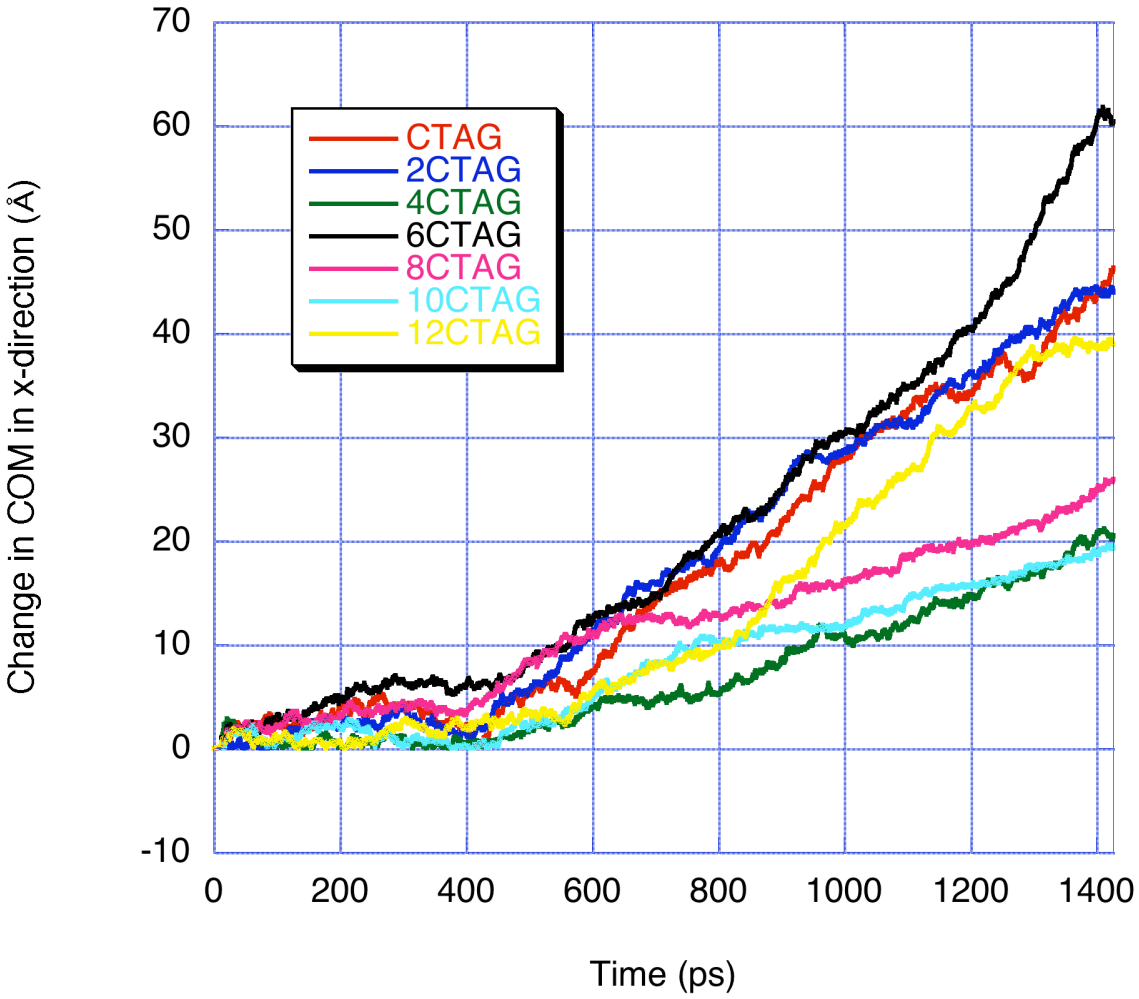

Figure 34: Change in position in *x*-direction vs. time based upon the center of mass resulting from the application of an external electric field.

Table 2: Translocation velocity as obtained from the slope of the change of center-of-mass over time and change from initial configuration in end-to-end distance of the molecule

Sample	Velocity (Å/ns)	Δ End-to-End Distance (Å)
CTAG	43.4	0.1
2CTAG	42.2	0.6
4CTAG	19.7	-23.0
6CTAG	53.2	-2.0
8CTAG	17.0	-26.1
10CTAG	17.8	-3.9
12CTAG	43.6	73.6

(a) (b)

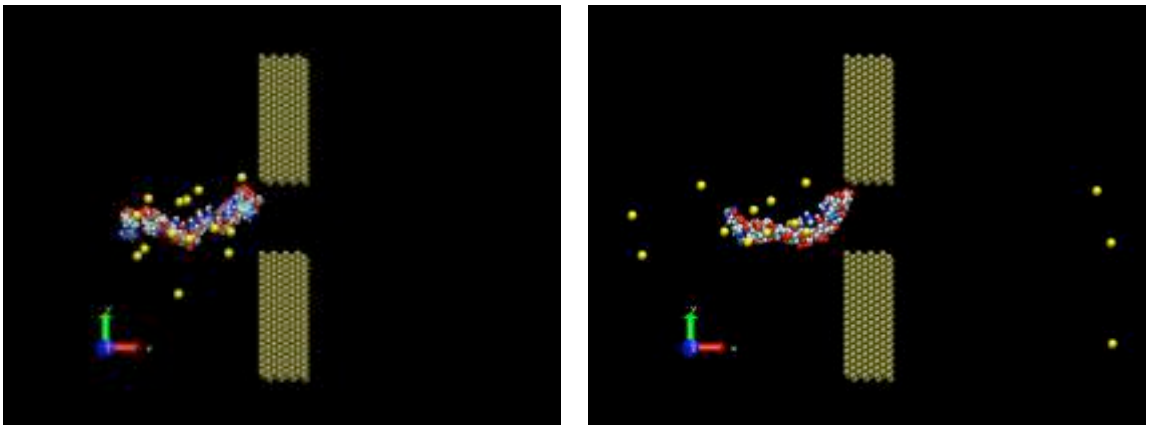

(c) (d)

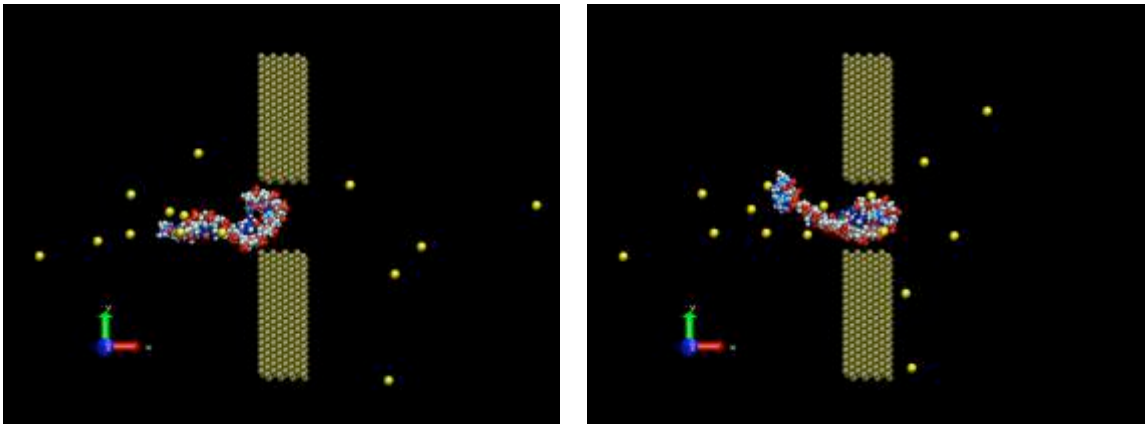

Figure 35: Snapshots of the –0.02 V/Å applied field simulation of 4CTAG in water through a 3.0 nm gate at (a) 0 ps, (b) 250 ps, (c) 500ps, and (d) 1000 ps.

Table 2 presents the translocation velocities as obtained from the slope of the change in center of mass versus time. The three samples for which the velocity is notably slowed experience significant molecular deformation due to the attraction to the electrode. It is commonly noted that DNA will "stick" to most surfaces[65-69], so this is not an unexpected result. However, it does imply that the length study will result in results for single trajectories that show considerable variation.

We believe molecular deformation could be avoided or reduced in three ways in future simulations. The shape of the electrodes, here and in our previous simulations, has proven to be a hindrance in the entrance of the molecule to the nanogate. The shaping of the electrodes into a sort of double conical shape to funnel the molecule into and out of the nanogate would probably alleviate some the deformed conformations at the entrance of the nanogate. A brief simulation result utilizing this technique shortly will be illustrated shortly. We will also examine the effect of pre-threading the ssDNA strand inside the nanogate by 1 nm. Additionally, the ssDNA sample could be replaced with a traditional double helix DNA molecule. This would render the molecule much less flexible, and less likely to deform. However, it is even less certain that a double helical molecule would be useful in determining DNA sequence. The concept on which this device is based lies in the detection of single nucleotides. To my knowledge, the current measurements of individual nucleotide pairs have not been examined.

Also in Table 2, we have presented the results of the change in end-to-end distance of the sample. The change in end-to-end distance has been defined as the end-to-end distance of the molecule as measured in the last timestep minus the end-to-end distance of the molecule in its initial configuration because of the difficulty in directly

comparing end-to-end distances of molecules of different initial lengths. End-to-end distances were measured from C5' atom of the first cytosine to the C2' atom of the last guanine. Ideal translocation would yield an elongated molecule as evidenced by portions of the 12CTAG sample.

The negative values for end-to-end distance represent the compacting of the molecule from it initial position. These generally correspond to the molecules with slower translocation velocities. The two smallest samples had very little change in the length of the molecule over the course of the nanosecond simulation.

VI.4 Shaped nanogate effects on translocation

VI.4.A System Setup and Simulation Details

This simulation used the same mica containment device as mentioned in Section VI.2. We chose to evaluate the 4CTAG sample as previously defined due to its significant deformation. The platinum electrodes were defined as has been done before for synthetic nanopores[63] as "double-conical" nanopores. Due to the confinement by the mica surfaces, the platinum electrodes do not technically form a conical shape; however, the shaping of the pore inside the device corresponds to this terminology. The platinum atoms form a shape with a diameter of

$$d(x) = d_o + |x| \tan\gamma \tag{19}$$

where the center of the pore and narrowest point is x = 0, d_o is the diameter of the pore at z = 0, and γ is the conical angle chosen here to be 45°. We chose d_o to be 2.5 nm here. The pore is 5 nm long in the x-direction, 5 nm wide in the y-direction, and 3 nm thick in

the z-direction. The 4CTAG sample was threaded 1 nm inside the pore as measured from the first platinum atom encountered in the x-direction.

We used the exact same potentials and simulation techniques as described in Sections V.2.B and V.2.D.

VI.4.B Results

The addition of a shaped nanopore, at least as can be surmised from a single trajectory, did little to alleviate the molecular deformation of the 4CTAG sample. Figure 36 illustrates through snapshots the compacting of the molecule into a deformed conformation. The head groups appear to make progress through the nanogate; however, the first cytosine group is attracted to one node while the tail guanine residue is attracted to the opposite node.

(a) (b)

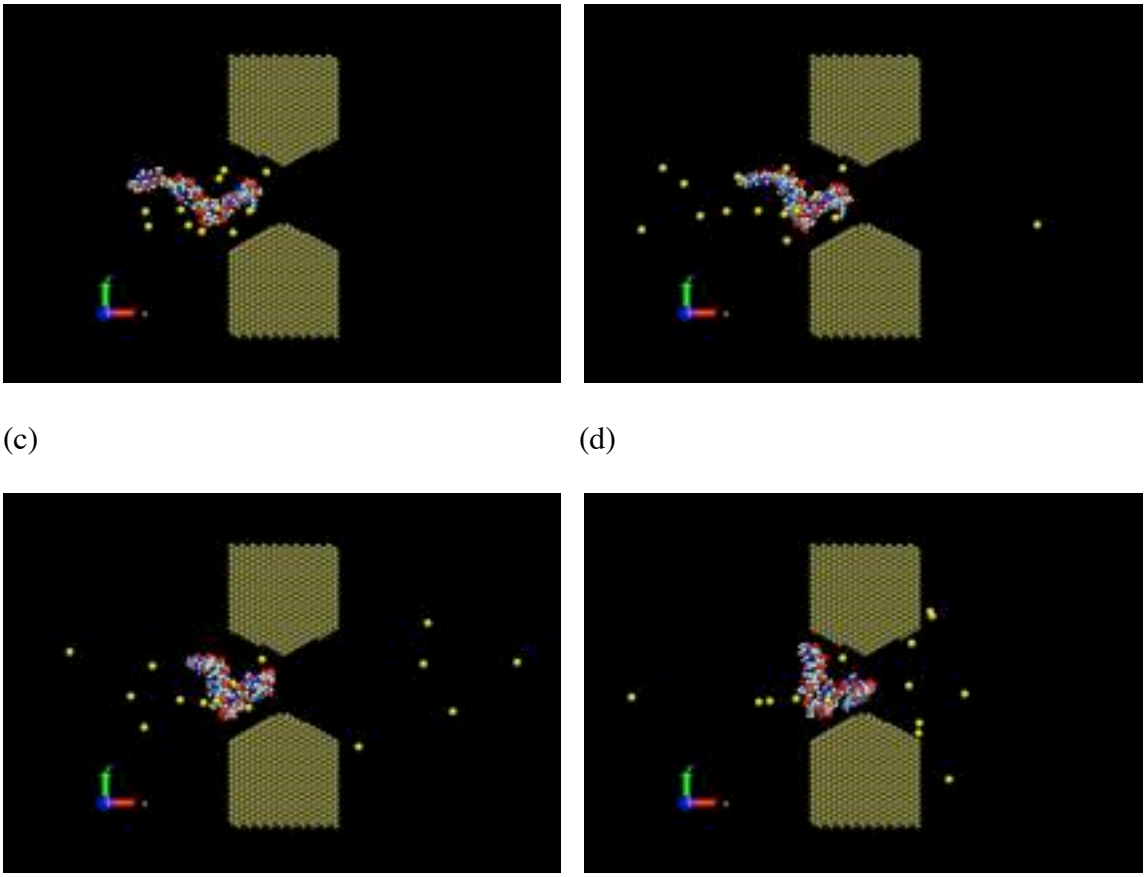

(c) (d)

Figure 36: Snapshots of the –0.02 V/Å applied field simulation of 4CTAG in water through the shaped nanogate at (a) 0 ps, (b) 250 ps, (c) 500ps, and (d) 1000 ps.

VI.5 Effect of pre-threading on translocation

The three samples, 4CTAG, 8CTAG, and 10CTAG, for which translocation was not observed above were subjected to further examination by attempting to overcome configurational hinderance to translocation through pre-threading the strands 1 nm inside the nanogate. Pre-threading, which has been done in a number of previous translocation studies[5-7, 63], results in a high probability of translocation. Apart from positioning the strand 1 nm inside the electrodes, the simulations were set up and executed exactly as described in Section VI.2 in the original chain length study. Figure 37 illustrates with snapshots the initial positioning as well as the final configuration of the 4CTAG sample.

Again, the center of mass of the first four residues was used as the point of reference for the molecule's motion in this study. Figure 38 shows the change in center of mass in the *x*-direction from its original position as a function of time. From the slope of each of these lines, we determined the translocation velocity. This translocation velocity is presented in Table 3 along with the change in end-to-end distance as described previously. The first 430ps are the equilibration steps referred to in the simulation details. At 430 ps, the 0.02 V/Å applied field has been applied to the ssDNA, ions, and platinum nodes.

It is evident from Figure 38 that the placement of the sample strand inside of the nanogate has a significant impact on the molecule's ability to translocate. The three samples pre-threaded inside the nanogate were able to translocate, whereas previously, they were unable. One can also see that the velocities here are relatively the same as the velocities of the molecules able to translocate without pre-threading. From Figure 39, in which all the results from Tables 2 and 3 corresponding to translocation are collected, it

appears that all of the ssDNA molecules translocate with a velocity of around 45 A/ns. The only exception is the result for 4CTAG, which evidently is atypical, and it probably not representative.

VI.6 Conclusions

Molecular dynamics simulations of the ssDNA electrophoretic translocation through a platinum nanogate have been performed to investigate the effect of sample length on overall translocation velocity. We were unable to conclusively evaluate the effect of changing length strand on the translocation velocity in the initial set of simulations. Molecules that did successfully begin translocation were generally in the previously determined acceptable velocity range of approximately 40 Å/ns inferred from simulations for a similar ssDNA molecule in bulk water[60] at the same applied field, which in turn is consistent with experimental results for translocation in the bulk.

Results varied based on the molecule's affinity for the nearby electrodes. Limited simulations of electrodes, shaped in an attempt to alleviate the molecular deformation resulting from the attraction to the electrodes, suggest that simply shaping the electrodes does not result in reduction of molecular deformation. However, pre-threading of the molecule inside the nanogate allowed for successful translocation and reduced molecular deformation of the head group.

The application of a stronger electrophoretic driving field might be able to force the strand through the gate opening more effectively over the time scale simulated. Likewise, the use of nanofluidic techniques to stretch the ssDNA out[70-72] and direct it through the electrodes appears to be necessary. It is also possible that surrounding the electrodes with another less attractive material (e.g., a hydrophobic material), shaped in

order to channel the ssDNA into the nanoelectrode gap, may result in reduced molecular deformation.

(a)

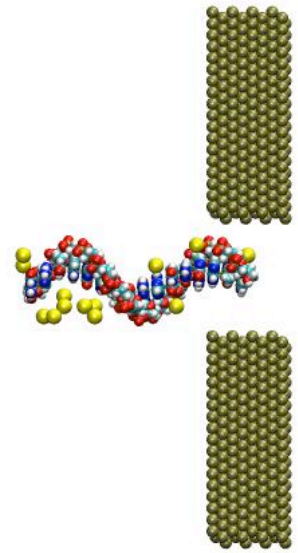

(b)

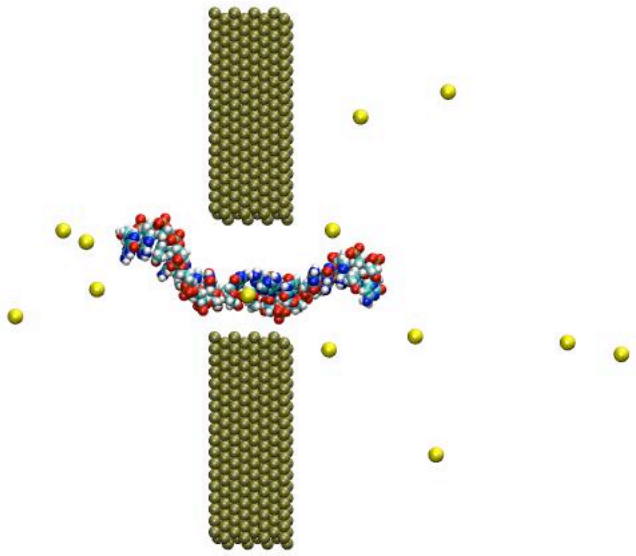

Figure 37: Snapshots of the –0.02 V/Å applied field simulation of 4CTAG in water pre-threaded 1 nm inside the nanogate (a) unequilibrated and (b) at 1000 ps.

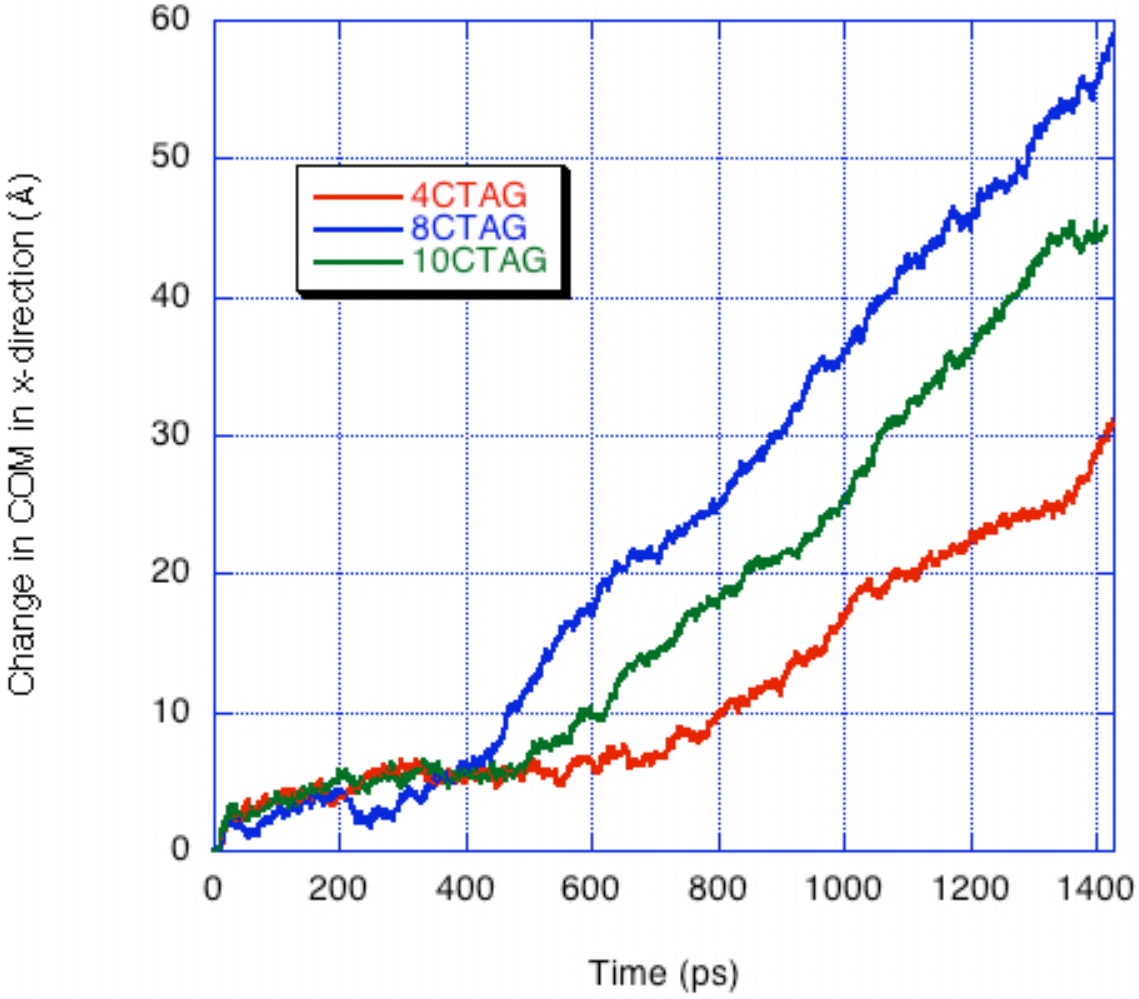

Figure 38: Change in position in *x*-direction vs. time of the pre-threaded ssDNA samples based upon the center of mass resulting from the application of an external electric field.

Table 3: Translocation velocity for pre-threaded ssDNA samples as obtained from the slope of the change of center-of-mass over time and change from initial configuration in end-to-end distance of the molecule.

Sample	Velocity (Å/ns)	Δ End-to-End Distance (Å)
4CTAG	26.1	5.1
8CTAG	49.1	-19.92
10CTAG	43.6	25.6

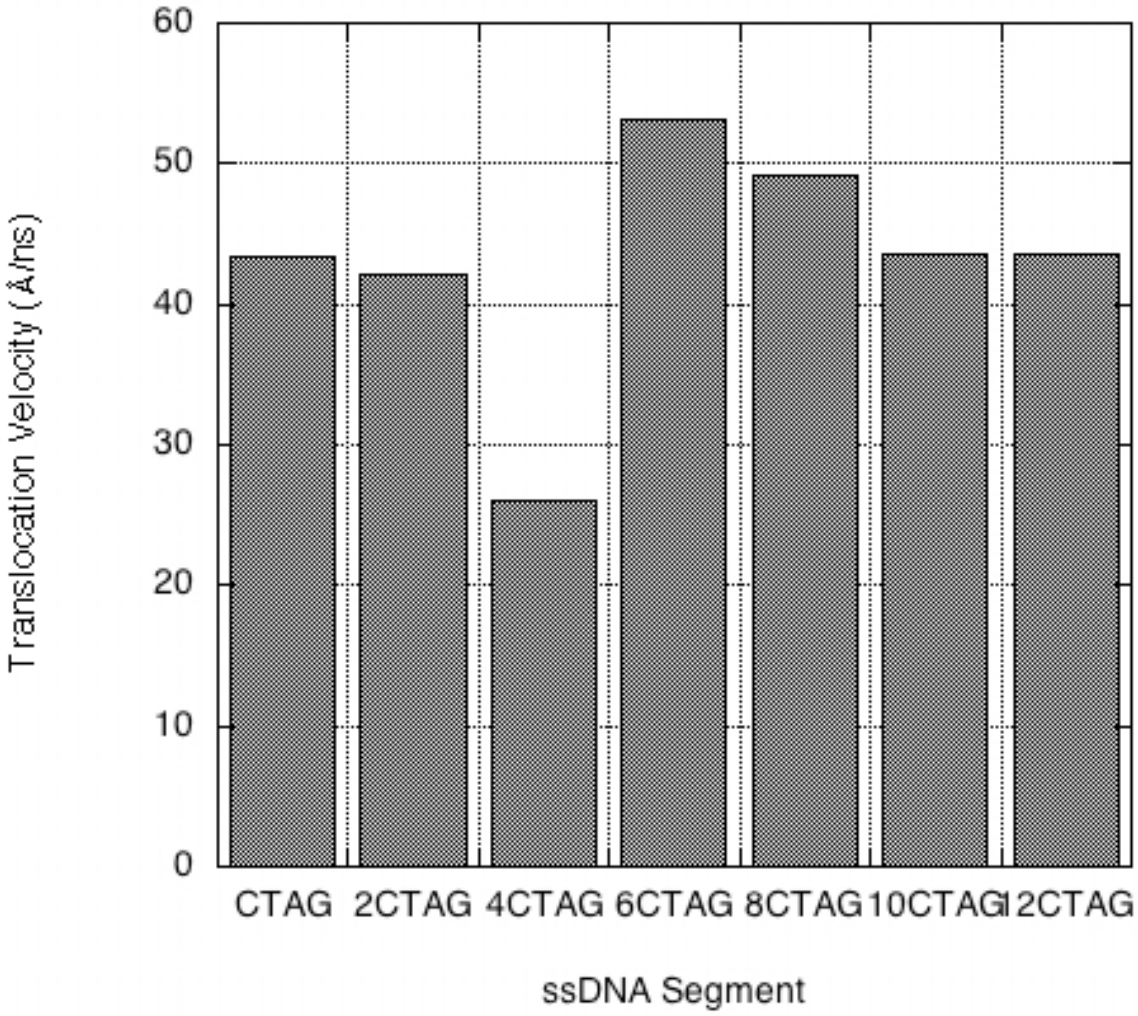

Figure 39: Summary of translocation velocities for different length ssDNA segments. The results shown consist of the simulations exhibiting translocation in Table 2 (CTAG, 2CTAG, 6CTAG, 12CTAG) and the results reported in Table 3 in which the molecules were placed 1 nm inside the nanogap. The average translocation velocity is 43±8 A/ns. If the outlying result (4CTAG) is removed, the average translocation velocity is 46±4 A/ns.

CHAPTER VII

CONCLUSIONS

VII.1 Synopsis

We have developed molecular dynamics simulations based on a conceptual device design for rapid sequencing of DNA. Preliminary simulations led to the search for more applicable metal/non-metal potentials to describe the interactions with the electrodes. We also performed electrophoretic simulations of DNA in bulk to compare simulation values for translocation velocity to experimental values through extrapolation. This ensured that the velocity values we obtained through simulation were within reasonable bounds.

Following initial investigatory simulations, we began full-scale simulations of the device concept using the electrode charge dynamics method to accurately describe metal/non-metal interactions with the intention of developing relationships between design variables and translocation behavior. Application of applied external electric fields illustrated that this method of control can be used to force ssDNA to translocate through a nanoscale gap; however, a clear relationship (i.e. linear or non-linear equation) was not obtained. There exist several factors including energetic barriers to nanopore translocation and molecular attraction to metal electrodes that have been prohibitive in developing this relationship. It was clear from this study, though, that electrode charge dynamics was the appropriate interaction potential for future simulations of this device.

Further design variable study led to the examination of the electrode gap width and it effect on allowing translocation of the ssDNA molecule. We found a heuristic

value for which the molecule will no longer translocate over the course of our nanosecond simulations. Widths larger than this value appear to have little effect on translocation speed. This value, 2.5 nm, happens to be slightly larger than previous studies of DNA translocation through synthetic nanopores. However, there are many differences in the simulations to consider including the ssDNA, the initial conditions, pore geometry and nature of the pore making direct comparisons difficult.

This final variable we considered was the length of the ssDNA sample. Realistic applications of this device will use DNA strands that are infinitely long on the molecular dynamics scale. We evaluated the translocation behavior of strands varying from 4 to 48 nucleotides, being limited by the electrostatic cutoff value and physical limitations of the simulated device as well as computational resources. We were unable to conclusively evaluate the effect of changing length strand (without pre-threading the sample) on translocation velocity due to the molecule's affinity for the electrodes. Pre-threading of the sample allowed for successful translocation in most cases and the resulting velocities suggest chain length has little influence on translocation velocity at nanoscale sample sizes. Attempting to overcome molecular deformation though the implementation of shaped electrodes, we were similarly unable to avoid the molecular attraction of the ssDNA to the metal electrodes. This affinity is well know in literature[65-69] and must be overcome through other methods in the future, such as using nanofluidic transport to the electrode so that the molecule arrives at the electrode in an extended conformation.

VII.2 Future Work

There exist several opportunities for continuation and extension of the work presented in this dissertation. A significant addition would include ensemble averaging of the individual simulations, though this would require significantly more computational resources than we currently have available. Ensemble averaging would possibly allow for the evaluation of a translocation velocity-length relationship in the case of the variable sample length simulations. Should a velocity-length relationship be developed, one could then compare the results to a mathematical model for polymer translocation through a long nanopore[73] which predicts two regimes of behavior based on polymer length and pore size.

The original concept called for the use of both platinum and gold electrodes for experimental implementation. Obtaining ECD parameters for gold atoms would make simulations line up even closer with the conceptual vision of the device. These parameters would also be of use for future simulations in different applications.

Extension of this project could easily be accomplished through evaluation of more device design variables. The solvent used in all simulations presented here was pure water. Evaluation of various viscosities (i.e. different solvents) and their effects on translocation could prove beneficial in determining ideal motive force. Presumably, the ideal applied electric field will also be dependent on solvent viscosity. Additional simulations investigating the shape of the electrodes may also be of value.

Finally, we believe it will be necessary to include some form of nanofluidic focusing device to properly align the strand at the entrance to the nanogap. Simulations investing the effects of the implementation of fluid flow (using the appropriate interaction

potentials) within the device would be of great value. It may even eliminate the need for an electrical driving force.

APPENDIX A

LAMMPS INPUT FILE

I have included here, for reference, a sample input file for use with the modified version of LAMMPS. This input file was used for the 4CTAG length simulation as described in Chapter 6. The input first sets about defining basic simulation input values such as boundary conditions and bond, angle, and dihedral types. Then after reading the data file, which contains some pair coefficient data, we define more specific interactions between atoms with the *pair_coeff* command. Then we use the *group* command to define groups of atoms that will be used in applying "fixes". The *chd* command is only valid in the modified LAMMPS version used for this work. It defines the electrode charge dynamics parameters |e| and γ and the atom type to which ECD is applied. We then apply our "fixes" which include NVT, SHAKE, and ECD. The run is performed in sections as presented here because of the extremely large size of the dump files. The ACCRE file system, and most LINUX machines, does not allow single files to be larger than 2GB in size without special compilation consideration. The equilibration occurs over 400,000 timesteps of varying sizes before the electric field is applied through a fix. The remaining dump files are the output of the production run of 1 ns.

```
units           real
neigh_modify    delay 5 every 1
boundary        p p f

atom_style      hybrid full chd
bond_style      harmonic
angle_style     charmm
dihedral_style  charmm
improper_style  harmonic
```

```
pair_style      hybrid lj/charmm/coul/long 8 10 morse/chd/long 10 chd/long 10
pair_modify     mix arithmetic
kspace_style    pppm 1e-4
kspace_modify   slab 3.0

read_data       4CTAG.data

special_bonds   charmm
pair_coeff      1 46 morse/chd/long 0.387 2.320 2.768
pair_coeff      31 46 morse/chd/long 0.1985 2.000 3.073
pair_coeff      39 46 lj/charmm/coul/long 0.06125 2.44173 0.06125 2.44173
pair_coeff      46 46 chd/long
pair_coeff      2*3 46 lj/charmm/coul/long 0.06066 1.42678 0.06066 1.42678
pair_coeff      4 46 lj/charmm/coul/long 0.06066 2.20676 0.06066 2.20676
pair_coeff      5 46 lj/charmm/coul/long 0.06066 1.42678 0.06066 1.42678
pair_coeff      6 46 lj/charmm/coul/long 0.04195 2.40276 0.04195 2.40276
pair_coeff      7 46 lj/charmm/coul/long 0.04733 2.42057 0.04733 2.42057
pair_coeff      8 46 lj/charmm/coul/long 0.04382 2.42057 0.04382 2.42057
pair_coeff      9*11 46 lj/charmm/coul/long 0.08944 2.91948 0.08944 2.91948
pair_coeff      12*16 46 lj/charmm/coul/long 0.08485 2.91948 0.08485 2.91948
pair_coeff      17*18 46 lj/charmm/coul/long 0.04000 3.25356 0.04000 3.25356
pair_coeff      19*20 46 lj/charmm/coul/long 0.06693 3.01748 0.06693 3.01748
pair_coeff      21 46 lj/charmm/coul/long 0.07899 3.04420 0.07899 3.04420
pair_coeff      22*30 46 lj/charmm/coul/long 0.12649 2.87493 0.12649 2.87493
pair_coeff      32*33 46 lj/charmm/coul/long 0.09798 2.74130 0.09798 2.74130
pair_coeff      34 46 lj/charmm/coul/long 0.11031 2.80366 0.11031 2.80366
pair_coeff      35 46 lj/charmm/coul/long 0.09798 2.74130 0.09798 2.74130
pair_coeff      36*37 46 lj/charmm/coul/long 0.11031 2.80366 0.11031 2.80366
pair_coeff      38 46 lj/charmm/coul/long 0.21633 3.14220 0.21633 3.14220
pair_coeff      40*41 46 lj/charmm/coul/long 0.00038 2.87778 0.00038 2.87778
pair_coeff      42 46 lj/charmm/coul/long 0.00033 3.36239 0.00033 3.36239
pair_coeff      43*44 46 lj/charmm/coul/long 0.11150 2.80954 0.11150 2.80954
pair_coeff      45 46 lj/charmm/coul/long 0.0 0.0 0.0 0.0
pair_coeff      46 47 lj/charmm/coul/long 0.08944 2.89378 0.08944 2.89378
pair_coeff      46 48 lj/charmm/coul/long 0.11150 2.80954 0.11150 2.80954

group           node1 id <> 523 2250
group           node2 id <> 2251 3978
group           mica type 40 41 42 43 44 45 47 48
group           water type 1 31
group           ions type 39
group           dna id <> 1 507
group           solution union water ions dna
group           platinum union node1 node2
group           surface union mica platinum
group           extfield union platinum solution

chd             46 1.0 0.751

fix             1 solution nvt 300.0 300.0 100.0
fix             2 all shake 1e-6 500 0 m 1.0 a 98
fix             3 platinum chd 0.0 5.0 100.0 2 node1 0.0 node2 0.0

temperature     mobile solution full
velocity        all create 0.0 12345678 dist uniform

thermo          1
thermo_style    one
thermo_modify   temp mobile
timestep        0.00005

dump            equil1 all atom 500 dump.atom.4ctag_equil.1

run             50000
```

```
undump          equil1
dump            equil2 all atom 500 dump.atom.4ctag_equil.2

timestep        0.005
run             50000

undump          equil2
dump            equil3 all atom 500 dump.atom.4ctag_equil.3

timestep        0.05

run             50000

undump          equil3
dump            equil4 all atom 500 dump.atom.4ctag_equil.4

timestep        0.5

run             50000

undump          equil4
dump            equil5 all atom 500 dump.atom.4ctag_equil.5


timestep        2.0
run             100000

undump          equil5
dump            equil6 all atom 500 dump.atom.4ctag_equil.6

run             100000
undump          equil6

fix             4 extfield efield -0.02 0.0 0.0

dump            d1 all atom 500 dump.atom.4ctag.1

run             100000


undump          d1
dump            d2 all atom 500 dump.atom.4ctag.2

run             100000


undump          d2
dump            d3 all atom 500 dump.atom.4ctag.3

run             100000

undump          d3
dump            d4 all atom 500 dump.atom.4ctag.4

run             100000

undump          d4
dump            d5 all atom 500 dump.atom.4ctag.5

run             100000
```

APPENDIX B

LAMMPS DATA FILE

I have included here, for reference, a sample data file for use with the modified version of LAMMPS. This data file was used for the 4CTAG length simulation as described in Chapter 6 and corresponds with the input file mentioned in Appendix A. Due to the size of the data file, only portions of it are shown here. The data file was created by the Charmm2Lammps utility included in the LAMMPS distribution under the *tools* directory from a PDB (protein data bank) file and PSF (protein structure file) file of the device. It follows the typical LAMMPS data file format listing number of atoms, boundaries, masses, pair coefficients, atom coordinates, bonds, angles, and dihedrals.

```
Created by charmm2lammps v1.6.3 on Tue Jul 24 16:47:25 CDT 2007

      138165  atoms
       59284  bonds
       27799  angles
        1689  dihedrals
          44  impropers

          48  atom types
          63  bond types
         121  angle types
         230  dihedral types
          10  improper types

      -0.698       207.86 xlo xhi
      -0.018      144.286 ylo yhi
     -50.403        0.846 zlo zhi


Masses

       1      1.008  # HT
       2      1.008  # HN1
       3      1.008  # HN2
       4      1.008  # HN3
       5      1.008  # HN5
       6      1.008  # HN7
```

```
 7      1.008  # HN8
 8      1.008  # HN9
 9     12.011  # CN1
10     12.011  # CN1T
11     12.011  # CN2
12     12.011  # CN3
13     12.011  # CN3T
14     12.011  # CN4
15     12.011  # CN5
16     12.011  # CN5G
17     12.011  # CN7
18     12.011  # CN7B
19     12.011  # CN8
20     12.011  # CN8B
21     12.011  # CN9
22     14.007  # NN1
23     14.007  # NN2
24     14.007  # NN2B
25     14.007  # NN2U
26     14.007  # NN2G
27     14.007  # NN3
28     14.007  # NN3A
29     14.007  # NN3G
30     14.007  # NN4
31    15.9994  # OT
32    15.9994  # ON1
33    15.9994  # ON1C
34    15.9994  # ON2
35    15.9994  # ON3
36    15.9994  # ON5
37    15.9994  # ON6
38     30.974  # P
39   22.98977  # SOD
40      28.09  # SI
41      26.98  # AT
42      26.98  # AO
43         16  # OB
44         16  # OH
45      1.008  # HO
46     195.08  # PT
47     39.102  # POTM
48         16  # OTT

Pair Coeffs

 1 lj/charmm/coul/long     0.046  0.4000135      0.046  0.4000135  # HT
 2 lj/charmm/coul/long     0.046  0.4000135      0.046  0.4000135  # HN1
 3 lj/charmm/coul/long     0.046  0.4000135      0.046  0.4000135  # HN2
 4 lj/charmm/coul/long     0.046   1.959977      0.046   1.959977  # HN3
 5 lj/charmm/coul/long     0.046  0.4000135      0.046  0.4000135  # HN5
 6 lj/charmm/coul/long     0.022   2.351973      0.022   2.351973  # HN7
 7 lj/charmm/coul/long     0.028   2.387609      0.028   2.387609  # HN8
 8 lj/charmm/coul/long     0.024   2.387609      0.024   2.387609  # HN9
 9 lj/charmm/coul/long       0.1   3.385415        0.1   3.385415  # CN1
10 lj/charmm/coul/long       0.1   3.385415        0.1   3.385415  # CN1T
11 lj/charmm/coul/long       0.1   3.385415        0.1   3.385415  # CN2
12 lj/charmm/coul/long      0.09   3.385415       0.09   3.385415  # CN3
13 lj/charmm/coul/long      0.09   3.385415       0.09   3.385415  # CN3T
14 lj/charmm/coul/long     0.075   3.385415      0.075   3.385415  # CN4
15 lj/charmm/coul/long     0.075   3.385415      0.075   3.385415  # CN5
16 lj/charmm/coul/long     0.075   3.385415      0.075   3.385415  # CN5G
17 lj/charmm/coul/long      0.02   4.053589       0.01   3.385415  # CN7
18 lj/charmm/coul/long      0.02   4.053589       0.01   3.385415  # CN7B
19 lj/charmm/coul/long     0.056   3.581413       0.01   3.385415  # CN8
20 lj/charmm/coul/long     0.056   3.581413       0.01   3.385415  # CN8B
```

```
       21 lj/charmm/coul/long     0.078   3.634867       0.01   3.385415  # CN9
       22 lj/charmm/coul/long       0.2   3.296325        0.2   3.296325  # NN1
       23 lj/charmm/coul/long       0.2   3.296325        0.2   3.296325  # NN2
       24 lj/charmm/coul/long       0.2   3.296325        0.2   3.296325  # NN2B
       25 lj/charmm/coul/long       0.2   3.296325        0.2   3.296325  # NN2U
       26 lj/charmm/coul/long       0.2   3.296325        0.2   3.296325  # NN2G
       27 lj/charmm/coul/long       0.2   3.296325        0.2   3.296325  # NN3
       28 lj/charmm/coul/long       0.2   3.296325        0.2   3.296325  # NN3A
       29 lj/charmm/coul/long       0.2   3.296325        0.2   3.296325  # NN3G
       30 lj/charmm/coul/long       0.2   3.296325        0.2   3.296325  # NN4
       31 lj/charmm/coul/long    0.1521   3.150574     0.1521   3.150574  # OT
       32 lj/charmm/coul/long      0.12   3.029056       0.12   3.029056  # ON1
       33 lj/charmm/coul/long      0.12   3.029056       0.12   3.029056  # ON1C
       34 lj/charmm/coul/long    0.1521   3.153781     0.1521   3.153781  # ON2
       35 lj/charmm/coul/long      0.12   3.029056       0.12   3.029056  # ON3
       36 lj/charmm/coul/long    0.1521   3.153781     0.1521   3.153781  # ON5
       37 lj/charmm/coul/long    0.1521   3.153781     0.1521   3.153781  # ON6
       38 lj/charmm/coul/long     0.585   3.830864      0.585   3.830864  # P
       39 lj/charmm/coul/long    0.0469   2.429926     0.0469   2.429926  # SOD
       40 lj/charmm/coul/long 1.8405e-06   3.302027 1.8405e-06   3.302027  # SI
       41 lj/charmm/coul/long 1.8405e-06   3.302027 1.8405e-06   3.302027  # AT
       42 lj/charmm/coul/long 1.3298e-06   4.271236 1.3298e-06   4.271236  # AO
       43 lj/charmm/coul/long    0.1554   3.165541     0.1554   3.165541  # OB
       44 lj/charmm/coul/long    0.1554   3.165541     0.1554   3.165541  # OH
       45 lj/charmm/coul/long         0          0          0          0  # HO
       46 chd/long                                                       # PT
       47 lj/charmm/coul/long       0.1    3.33401        0.1    3.33401  # POTM
       48 lj/charmm/coul/long    0.1554   3.165541     0.1554   3.165541  # OTT

Atoms

        1       1    17      0.16      94.225      72.436     -16.166  # CN7
        2       1     6      0.09      94.907      73.274     -16.024  # HN7
        3       1    37      -0.5      94.046       72.35     -17.612  # ON6
        4       1    18      0.16       92.68      72.119     -17.921  # CN7B
        5       1     6      0.09      92.303      72.936     -18.536  # HN7
        6       1    19     -0.18      91.924      71.948     -16.602  # CN8
        7       1     7      0.09      91.352      71.196     -16.059  # HN8
        8       1     7      0.09       91.24      72.644     -17.088  # HN8
        9       1     5      0.43      94.156      69.293     -15.097  # HN5
                                        .
                                        .
                                        .

Bond Coeffs

        1        302      1.403  # CN1  CN3T
        2        302       1.36  # CN1  CN5G
        3        380      1.367  # CN1  NN2
        4        340      1.396  # CN1  NN2G
        5        340      1.389  # CN1  NN2U
        6        350      1.335  # CN1  NN3
        7        660      1.234  # CN1  ON1
        8        620      1.245  # CN1  ON1C
        9        302      1.348  # CN1T NN2B
                                        .
                                        .
                                        .
```

```
Bonds

       1      44       1        3  # CN7  ON6
       2      38       1       26  # CN7  CN7
       3      41       1        2  # CN7  HN7
       4      49       3        4  # CN7B ON6
       5      47       4       14  # CN7B NN2
       6      45       4        6  # CN7B CN8
       7      46       4        5  # CN7B HN7
       8      50       6        7  # CN8  HN8
       9      39       6       26  # CN7  CN8
                                 .
                                 .
                                 .

Angle Coeffs

       1     120     116.7          0          0  # CN1  CN3T CN3
       2      38     118.7          0          0  # CN1  CN3T CN9
       3      70     119.6          0          0  # CN1  CN5G CN5
       4     125       129          0          0  # CN1  CN5G NN4
       5      50     124.1          0          0  # CN1  NN2  CN3
       6      45       120          0          0  # CN1  NN2  CN7B
       7      70     131.1          0          0  # CN1  NN2G CN2
       8      45     113.3          0          0  # CN1  NN2G HN2
       9      50     130.2          0          0  # CN1  NN2U CN1T
                                 .
                                 .
                                 .

Angles

       1      56       1       26       27  # CN7  CN7  HN7
       2      57       1       26       28  # CN7  CN7  ON2
       3      54       1       26        6  # CN7  CN7  CN8
       4      67       1        3        4  # CN7  ON6  CN7B
       5      62       1       11       13  # CN7  CN8B HN8
       6      62       1       11       12  # CN7  CN8B HN8
       7      92       3        4        5  # HN7  CN7B ON6
       8      75       3        4        6  # CN8  CN7B ON6
       9     107       3        4       14  # NN2  CN7B ON6
                                 .
                                 .
                                 .

Dihedral Coeffs

       1       1          2        180          1  # CN1  CN3T CN3  HN3
       2       3          2        180        0.5  # CN1  CN3T CN3  NN2B
       3    0.46          3          0          1  # CN1  CN3T CN9  HN9
       4       0          2        180          1  # CN1  CN5G CN5  NN2B
       5       2          2        180        0.5  # CN1  CN5G CN5  NN3G
       6       2          2        180          1  # CN1  CN5G NN4  CN4
       7     0.6          2        180        0.5  # CN1  NN2  CN3  CN3
       8     4.6          2        180          1  # CN1  NN2  CN3  HN3
       9       1          3          0          1  # CN1  NN2  CN7B CN8
                                 .
                                 .
```

.

Dihedrals

```
       1     101       1      26       6       4  # CN7  CN7  CN8  CN7B
       2     102       1      26       6       8  # CN7  CN7  CN8  HN8
       3     112       1      26      28      37  # CN7  CN7  ON2  P
       4     113       1      26      28      37  # CN7  CN7  ON2  P
       5     115       1      26      28      37  # CN7  CN7  ON2  P
       6     116       1      26      28      37  # CN7  CN7  ON2  P
       7     136       1       3       4      14  # CN7  ON6  CN7B NN2
       8     134       1       3       4       6  # CN7  ON6  CN7B CN8
       9     135       1       3       4       5  # CN7  ON6  CN7B HN7
```

.

.

.

Improper Coeffs

```
       1         80          0  # CN1  NN2  NN3  ON1C
       2         90          0  # CN1  NN2G CN5G ON1
       3         90          0  # CN1  NN2U CN3T ON1
       4        110          0  # CN1T NN2B NN2U ON1
       5         60          0  # CN2  NN3  CN3  NN1
       6         40          0  # CN2  NN3A CN5  NN1
       7         40          0  # CN2  NN3G NN2G NN1
       8         14          0  # CN3T CN1  CN3  CN9
       9          4          0  # HN1  CN2  HN1  NN1
      10          6          0  # HN1  HN1  CN2  NN1
```

Impropers

```
       1       1      19      14      21      20  # CN1  NN2  NN3  ON1C
       2       5      22      21      17      23  # CN2  NN3  CN3  NN1
       3      10      23      22      24      25  # HN1  HN1  CN2  NN1
       4       4      47      44      49      48  # CN1T NN2B NN2U ON1
       5       3      51      49      53      52  # CN1  NN2U CN3T ON1
       6       8      53      51      45      54  # CN3T CN1  CN3  CN9
       7       6      86      81      77      87  # CN2  NN3A CN5  NN1
       8      10      87      86      88      89  # HN1  HN1  CN2  NN1
       9       9     110     111     114     112  # HN1  CN2  HN1  NN1
```

APPENDIX C

NONLINEAR ELECTRIC FIELD EFFECTS

Here, we will present a brief description of the molecular basis for the nonlinear field effects such as those observed in the large magnitude applied electric field simulations presented in Chapter IV.

It is well known that thermodynamic systems' fluctuations in flux can be described by a linearly proportional relationship of the transport coefficient with the corresponding applied field[74]. This relationship holds true in the limiting case of a sufficiently small applied field. The standard chemical engineering example of this relationship is Newton's law of viscosity, where shear stress, $\tau_{\xi\psi}$, is linearly proportional to the strain rate, $du_x/dy = \dot{\gamma}$, through the relationship

$$\tau_{xy} = -\eta\dot{\gamma} \tag{20}$$

where η is the shear viscosity. In the linear (i.e., Newtonian) regime, η does not depend on $\dot{\gamma}$, and τ_{xy} is linear in $\dot{\gamma}$. However, as the strain rate increases, we know to expect the shear stress to exhibit nonlinear strain-rate dependence, resulting in a strain-rate-dependent viscosity. This is the non-linear regime, and in this regime the fluid is described as being non-Newtonian. Generally, the onset of non-linear shear response occurs then the strain rate exceeds τ^{-1}, where τ is the longest relaxation time in the system. Hence at the molecular scale it corresponds to shear rates so large that the molecules cannot relax into their equilibrium shapes when moving between different

locations in the strain field. These effects are most striking in polymers, where the relaxation times can be very long (and hence the strain rate needed to induce non-linear behavior is not very large) and where the conformational molecular changes in large strain fields (the polymer molecules stretch out to align with the strain field) give rise to large non-linear effects in the viscosity.

The same can be said for any equilibrium system under the influence of and applied external field, whether it be mechanical or thermal, including the relationship of drift velocity to electrophoretic mobility and applied electric field as described in Equation 6. As the applied field increases to the nonlinear regime, the proportionality constant, electrophoretic mobility in this case, becomes a function of the applied field and no longer results in linear flux behavior. This is behavior is apparent in the molecular conformation through alignment and elongation of the molecule with increasing external applied field. We should also see some alignment of the water molecules in response to the increasing external field[75], though we have not made a point of studying this molecular configuration. This behavior has been previously documented in many different systems[76-80] and is described in significant detail by Evans and Morriss[81].

REFERENCES

1. Venter, J. C.; Adams, M. D.; Myers, E. W.; al., e., The Sequence of the Human Genome. *Science* **2001,** 291, (5507), 1304-1351.

2. Allen, M. P.; Tildesley, D. J., *Computer Simulations of Liquids*. Clarendon Press: Oxford, 1987.

3. Zhang, L.; George, B.; Thundat, T.; Lee, J., Measurements of Electrical Transport Properties of Single-Stranded DNA Molecules. **Submitted for publication**.

4. Meller, A.; Nivon, L.; Branton, D., Voltage-Driven DNA Translocations Through a Nanopore. *Physical Review Letters* **2001,** 86, (15), 3435-3438.

5. Heng, J. B.; Ho, C.; Kim, T.; Timp, R.; Aksimentiev, A.; Grinkova, Y. V.; Sligar, S.; Schulten, K.; Timp, G., Sizing DNA Using a Nanometer-Diameter Pore. *Biophys. J.* **2004,** 87, (4), 2905-2911.

6. Storm, A.; Chen, J.; Zandbergen, H.; Dekker, C., Translocation of Double-Strand DNA Through a Silicon Oxide Nanopore. *Physical Review E* **2005,** 71, 051903.

7. Storm, A. J.; Storm, C.; Chen, J.; Zandbergen, H.; Joanny, J. F.; Dekker, C., Fast DNA Translocation through a Solid-State Nanopore. *Nano Lett.* **2005,** 5, (7), 1193-1197.

8. Fan, R.; Karnik, R.; Yue, M.; Li, D.; Majumdar, A.; Yang, P., DNA Translocation in Inorganic Nanotubes. *Nano Lett.* **2005,** 5, (9), 1633-1637.

9. Fologea, D.; Gershow, M.; Ledden, B.; McNabb, D. S.; Golovchenko, J. A.; Li, J., Detecting Single Stranded DNA with a Solid State Nanopore. *Nano Lett.* **2005,** 5, (10), 1905-1909.

10. Sung, W.; Park, P. J., Polymer Translocation through a Pore in a Membrane. *Physical Review Letters* **1996,** 77, (4), 783.

11. Lubensky, D. K.; Nelson, D. R., Driven Polymer Translocation Through a Narrow Pore. *Biophys. J.* **1999,** 77, (4), 1824-1838.

12. Kong, C. Y.; Muthukumar, M., Modeling of polynucleotide translocation through protein pores and nanotubes. *ELECTROPHORESIS* **2002,** 23, (16), 2697-2703.

13. Butler, T. Z.; Gundlach, J. H.; Troll, M. A., Determination of RNA Orientation during Translocation through a Biological Nanopore. *Biophys. J.* **2006,** 90, (1), 190-199.

14. Yeh, I.-C.; Hummer, G., Diffusion and Electrophoretic Mobility of Single-Stranded RNA from Molecular Dynamics Simulations. *Biophys. J.* **2004,** 86, (2), 681-689.

15. Lee, J. W.; Greenbaum, E., 1999. Programmable Nanometer-Scale Metal Bonding to Single Molecules by Electrolytic Deposition and Depletion. ORNL Invention Disclosure ID 0772;

16. Lee, J. W.; Greenbaum, E. 2002. Programmable Nanometer-Scale Electrolytic Metal Deposition and Depletion. Office, U. P. 6,447,663 B1.

17. Lagerqvist, J.; Zwolak, M.; DiVentra, M., Fast DNA Sequencing via Transverse Electronic Transport. *Nano Lett.* **2006,** 6, (4), 779-782.

18. Lagerqvist, J.; Zwolak, M.; Di Ventra, M., Influence of the Environment and Probes on Rapid DNA Sequencing via Transverse Electronic Transport. *Biophys. J.* **2007,** 93, (7), 2384-2390.

19. Zhang, X. G.; Krstic, P. S.; Zikic, R.; Wells, J. C.; Fuentes-Cabrera, M., First-Principles Transversal DNA Conductance Deconstructed. *Biophys. J.* **2006,** 91, (1), L04-6.

20. Lee, J.; Thundat, T.; Greenbaum, E., 2001. DNA and RNA Sequencing by Nanoscale Reading Through Programmable Electrophoresis and Nanoelectrode-Gated Tunneling and Dielectric Detection. ORNL Invention Disclosure ID 0943; US Patent Appl. Publ. (2003), 24 pp. CODEN: USXXCO US 2003141189 A1.

21. Leng, Y.; Cummings, P. T., Fluidity of Hydration Layers Nanoconfined between Mica Surfaces. *Physical Review Letters* **2005,** 94, (2), 026101-4.

22. Franklin, R.; Gosling, R., Molecular Configuration in Sodium Thymonucleate. *Nature* **1953,** 171, 740.

23. Swope, W. C.; Andersen, H. C.; Berens, P. H.; Wilson, K. R., A computer simulations method for the calculations of equilibrium constants for the formations of physical clusters of molecules: Application to small water clusters. *J. Chem. Phys.* **1982,** 76, 637-649.

24. Plimpton, S., Fast Parallel Algorithms for Short-Range Molecular Dynamics. *Journal of Computational Physics* **1995,** 117, (1), 1-19.

25. Plimpton, S.; LAMMPS. http://lammps.sandia.gov

26. Foloppe, N.; MacKerell, A. D., All-atom empirical force field for nucleic acids: I. Parameter optimization based on small molecule and condensed phase macromolecular target data. *Journal of Computational Chemistry* **2000,** 21, (2), 86-104.

27. MacKerell, A. D.; Banavali, N. K., All-atom empirical force field for nucleic acids: II. Application to molecular dynamics simulations of DNA and RNA in solution. *Journal of Computational Chemistry* **2000,** 21, (2), 105-120.

28. Beglov, D.; Roux, B., Finite representation of an infinite bulk system: Solvent boundary potential for computer simulations. *The Journal of Chemical Physics* **1994,** 100, (12), 9050-9063.

29. Jorgensen, W. L.; Chandrasekhar, J.; Madura, J. D.; Impey, R. W.; Klein, M. L., Comparison of simple potential functions for simulating liquid water. *The Journal of Chemical Physics* **1983,** 79, (2), 926-935.

30. Cygan, R. T.; Liang, J. J.; Kalinichev, A. G., Molecular Models of Hydroxide, Oxyhydroxide, and Clay Phases and the Development of a General Force Field. *J. Phys. Chem. B* **2004,** 108, (4), 1255-1266.

31. Rappé, A.; Casewit, C.; Colwell, K.; Goddard, W.; Skiff, W., UFF, a Full Periodic Table Force Field for Molecular Mechanics and Molecular Dynamics Simulations. *Journal of the American Chemical Society* **1992,** 114, 10024-10035.

32. Hockney, R. W.; Eastwood, J. W., *Computer Simulation Using Particles*. McGraw-Hill International Book co.: New York, 1989.

33. Yeh, I.-C.; Berkowitz, M. L., Ewald summation for systems with slab geometry. *The Journal of Chemical Physics* **1999,** 111, (7), 3155-3162.

34. Nosé, S., A molecular dynamics method for simulations in the canonical ensemble. *Molecular Physics* **1984,** 52, 255.

35. Nosé, S., A unified formulation of hte constant temperature molecular dynamics methods. *The Journal of Chemical Physics* **1984,** 81, (1), 511-519.

36. Hoover, W. G., Canonical dynamics: Equilibrium phase-space distributions. *Physical Review A* **1985,** 31, (3), 1695.

37. Payne, C. M.; Zhao, X.; Vlcek, L.; Cummings, P. T., Molecular Dynamics Simulation of DNA Translocation through a Copper Nanoelectrode Gap **submitted to Journal of Physical Chemistry C**.

38. Kasianowicz, J. J.; Brandin, E.; Branton, D.; Deamer, D. W., Characterization of individual polynucleotide molecules using a membrane†channel. *PNAS* **1996,** 93, (24), 13770-13773.

39. Stellwagen, E.; Stellwagen, N. C., Determining the electrophoretic mobility and translational diffusion coefficients of DNA molecules in free solution. *Electrophoresis* **2002,** 23, (16), 2794-2803.

40. Jackson, J. D., *Classical Electrodynamics*. Wiley: New York, 1962.

41. Spohr, E.; Heinzinger, K., Molecular dynamics simulation of a water/metal interface. *Chemical Physics Letters* **1986,** 123, (3), 218-221.

42. Guymon, C.; Rowley, R.; Harb, J.; Wheeler, D., Simulating an Electrochemical Interface Using Charge Dynamics. *Condensed Matter Physics* **2005,** 8, (2), 335-356.

43. Hoagland, D. A.; Arvanitidou, E.; Welch, C., Capillary Electrophoresis Measurements of the Free Solution Mobility for Several Model Polyelectrolyte Systems. *Macromolecules* **1999,** 32, 6180-6190.

44. Macke, T.; Case, D. A. In *Modeling unusual nucleic acid structures*, American Chemical Society, Washington, DC, 1998; Leontes, N. B.; J. SantaLucia, J., Eds. Washington, DC, 1998; pp 379-393.

45. Macke, T.; Svrcek-Seiler, W. A.; Brown, R. A.; Case, D. A.; The NAB Molecular Manipulation Language. http://www.scripps.edu/mb/case/

46. Berendsen, H. J. C.; Postma, J. P. M.; Gunsteren, W. F. v.; DiNola, A.; Haak, J. R., Molecular dynamics with coupling to an external bath. *The Journal of Chemical Physics* **1984,** 81, (8), 3684-3690.

47. Martyna, G. J.; Tobias, D. J.; Klein, M. L., Constant pressure molecular dynamics algorithms. *The Journal of Chemical Physics* **1994,** 101, (5), 4177-4189.

48. Ryckaert, J.-P.; Ciccotti, G.; Berendsen, H. J. C., Numerical integration of the cartesian equations of motion of a system with constraints: molecular dynamics of n-alkanes. *Journal of Computational Physics* **1977,** 23, (3), 327-341.

49. Dukhin, A. S.; Dukhin, S. S., Aperiodic capillary electrophoresis method using an alternating current electric field for separation of macromolecules. *Electrophoresis* **2005,** 26, (11), 2149-2153.

50. Raviv, U.; Klein, J., Fluidity of Bound Hydration Layers. *Science* **2002,** 297, (5586), 1540-1543.

51. Leng, Y.; Cummings, P. T., Fluidity of Hydration Layers Nanoconfined between Mica Surfaces. *Physical Review Letters* **2005,** 94, (2), 026101.

52. Leng, Y.; Cummings, P. T., Hydration structure of water confined between mica surfaces. *The Journal of Chemical Physics* **2006,** 124, (7), 074711.

53. Rappe, A. K.; Colwell, K. S.; Casewit, C. J., Application of a universal force field to metal complexes. *Inorg. Chem.* **1993,** 32, (16), 3438-3450.

54. Boyd, P. D. W.; Hodgson, M. C.; Rickard, C. E. F.; Oliver, A. G.; Chaker, L.; Brothers, P. J.; Bolskar, R. D.; Tham, F. S.; Reed, C. A., Selective Supramolecular Porphyrin/Fullerene Interactions. *J. Am. Chem. Soc.* **1999,** 121, (45), 10487-10495.

55. Fa, W.; Chen, J.; Liu, H.; Dong, J., Structural and electronic properties of the metal-metal intramoleular junctions of single-walled carbon nanotubes. *Physical Review B (Condensed Matter and Materials Physics)* **2004,** 69, (23), 235413.

56. Felix, V.; Matthews, S. E.; Beer, P. D.; Drew, M. G. B., Selectivity of calix[4]tubes towards metal ions: A molecular dynamics study. *Physical Chemistry Chemical Physics* **2002,** 4, (15), 3849-3858.

57. Horinek, D.; Michl, J., Surface-mounted altitudinal molecular rotors in alternating electric field: Single-molecule parametric oscillator molecular dynamics. *Proceedings of the National Academy of Sciences* **2005,** 102, (40), 14175-14180.

58. Evans, D. J.; Searles, D. J., Equilibrium microstates which generate second law violating steady states. *Physical Review E* **1994,** 50, (2), 1645.

59. Evans, D. J.; Searles, D. J., The Fluctuation Theorem. *Advances in Physics* **2002,** 51, (7), 1529-1585.

60. Payne, C. M.; Zhao, X.; Cummings, P. T., Molecular simulations of DNA transport in solution. *Molecular Simulation* **2007,** 33, (4), 399 - 403.

61. Wheeler, D.; Newman, J., Molecular Dynamics Simulations of Multicomponent Diffusion. 2. Nonequilibrium Method. *Journal of Physical Chemistry B* **2004,** 108, 18362-18367.

62. Meng, S.; Wang, E. G.; Gao, S., Water adsorption on metal surfaces: A general picture from density functional theory studies. *Physical Review B* **2004,** 69, 195404.

63. Heng, J. B.; Aksimentiev, A.; Ho, C.; Marks, P.; Grinkova, Y. V.; Sligar, S.; Schulten, K.; Timp, G., The Electromechanics of DNA in a Synthetic Nanopore. *Biophys. J.* **2006,** 90, (3), 1098-1106.

64. Henrickson, S. E.; Misakian, M.; Robertson, B.; Kasianowicz, J. J., Driven DNA Transport into an Asymmetric Nanometer-Scale Pore. *Physical Review Letters* **2000,** 85, (14), 3057.

65. Tsang, S. C.; Guo, Z.; Chen, Y. K.; Green, M. L. H.; Hill, H. A. O.; Hambley, T. W.; Sadler, P. J., Immobilization of Platinated and Iodinated Oligonucleotides on Carbon Nanotubes. *Angewandte Chemie International Edition in English* **1997,** 36, (20), 2198-2200.

66. Buzaneva, E.; Karlash, A.; Yakovkin, K.; Shtogun, Y.; Putselyk, S.; Zherebetskiy, D.; Gorchinskiy, A.; Popova, G.; Prilutska, S.; Matyshevska, O.; Prilutskyy, Y.; Lytvyn,

P.; Scharff, P.; Eklund, P., DNA nanotechnology of carbon nanotube cells: physico-chemical models of self-organization and properties. *Materials Science and Engineering: C* **2002,** 19, (1-2), 41-45.

67. Zheng, M.; Jagota, A.; Semke, E. D.; Diner, B. A.; McLean, R. S.; Lustig, S. R.; Richardson, R. E.; Tassi, N. G., DNA-assisted dispersion and separation of carbon nanotubes. *Nat Mater* **2003,** 2, (5), 338-342.

68. Gearheart, L. A.; Ploehn, H. J.; Murphy, C. J., Oligonucleotide Adsorption to Gold Nanoparticles: A Surface-Enhanced Raman Spectroscopy Study of Intrinsically Bent DNA. *J. Phys. Chem. B* **2001,** 105, (50), 12609-12615.

69. Mbindyo, J. K. N.; Reiss, B. D.; Martin, B. R.; Keating, C. D.; Natan, M. J.; Mallouk, T. E., DNA-Directed Assembly of Gold Nanowires on Complementary Surfaces. *Advanced Materials* **2001,** 13, (4), 249-254.

70. Fang, L.; Hu, H.; Larson, R. G., DNA configurations and concentration in shearing flow near a glass surface in a microchannel. *Journal of Rheology* **2005,** 49, (1), 127-138.

71. Dukkipati, V. r.; Kim, J. H.; Pang, S. W.; Larson, R. G., Protein-Assisted Stretching and Immobilization of DNA Molecules in a Microchannel. *Nano Lett.* **2006,** 6, (11), 2499-2504.

72. Watari, N.; Makino, M.; Kikuchi, N.; Larson, R.; Doi, M., Simulation of DNA motion in a microchannel using stochastic rotation dynamics. *Journal of Chemical Physics* **2007,** 126, 094902.

73. Slonkina, E.; Kolomeisky, A. B., Polymer Translocation Through a Long Nanopore. *Journal of Chemical Physics* **2003,** 118, (15), 7112-7118.

74. Kubo, R.; Yokota, M.; Nakajima, S., Statistical-mechanical theory of irreversible processes. II. Response to thermal disturbance. *Journal of the Physical Society of Japan* **1957,** 12, (11), 1203-1211.

75. Jung, D. H.; Yang, J. H.; Jhon, M. S., The effect of an external electric field on the structure of liquid water using molecular dynamics simulations. *Chemical Physics* **1999,** 244, 331-337.

76. Moore, J. D.; Cui, S. T.; Cochran, H. D.; Cummings, P. T., Rheology of lubricant basestocks: A molecular dynamics study of C_{30} isomers. *Journal of Chemical Physics* **2000,** 113, (19), 8833-8840.

77. Meyer, B.; Vanderbilt, D., Ab initio study of BaTiO_{3} and PbTiO_{3} surfaces in external electric fields. *Physical Review B* **2001,** 63, (20), 205426.

78. Kawasaki, K.; Gunton, J. D., Theory of Nonlinear Transport Processes: Nonlinear Shear Viscosity and Normal Stress Effects. *Physical Review A* **1973,** 8, (4), 2048.

79. Gravina, D.; Ciccotti, G.; Holian, B. L., Linear and nonlinear viscous flow in two-dimensional fluids. *Physical Review E* **1995,** 52, (6), 6123.

80. Maginn, E. J.; Bell, A. T.; Theodorou, D. N., Transport diffusivity of methane in silicalite from equilibrium and nonequilibrium simulations. *J. Phys. Chem.* **1993,** 97, (16), 4173-4181.

81. Evans, D. J.; Morriss, G. P., *Statistical Mechanics of Nonequilibrium Liquids*. Academic Press Inc.: San Diego, 1990.